UNIVERSITY OF CALIFORNIA,
IRVINE

Measuring and Understanding Pericellular Stiffness

DISSERTATION

submitted in partial satisfaction of the requirements
for the degree of

DOCTOR OF PHILOSOPHY

in Biomedical Engineering

by

Mark Keating

Dissertation Committee:
Professor Elliot L. Botvinick, Chair
Associate Professor Wendy Liu
Professor Michael Dennin

2018

DEDICATION

To

My family

You have been a continuous source of love and support throughout all challenges.

TABLE OF CONTENTS

LIST OF FIGURES

Page

LIST OF TABLES

ACKNOWLEDGEMENTS

I must first thank my advisor and committee chair, Professor Elliot Botvinick. Elliot has taught me how to approach and solve complex problems effectively. His enthusiasm for discovery cannot be understated – and, fortunately, is quite infectious. I most admire Elliot's dedication to his students. He has been there whenever we needed him, sometimes even working side-by-side with us in lab, but also being "hands off" enough to trust us to struggle and solve problems on our own. This has fostered independence as a researcher, but not isolation, for which I am greatly thankful.

During my time in the Botvinick Lab, I have been blessed with incredible lab mates who have no doubt elevated all work being done and made for amazing company during long studies throughout the years. The amazing culture for supporting and helping each other As an undergrad, I first worked under Dr. Martha Beatriz, who I cannot thank enough for her kindness and patience in helping me to learn the ropes within our lab. A special thanks especially to my first lab mates and friends: Drs. Abhishek Kurup, Shreyas Ravindrath, and Bhupinder Shergill for welcoming me into a lab culture that was friendly and engaging, but also for ensuring that we still challenged each other to always be better. I cannot thank Abhishek enough for his mentorship both during his time here in the lab and beyond. I deeply appreciate my conversations with Todd Thorson, Avid Najdahmadi, and Justin Luo who have always been encouraging and helpful. Fellow CARE fellow (among all her numerous fellowships) Rachel Gurlin deserves a specific 'thank you' for her dedication to the lab and helpful constructive criticism. My work would not be possible without the dedicated help from undergraduates Tim Tran and Micah Lim. In my short time working with Qingda Hu, who recently joined our lab as a PhD student, I have already grown to appreciate his insightful commentary and have no doubt the continuation of this work is in good hands. In our Biomedical Engineering Department, I have been blessed with amazing colleagues, all of whom may be too numerous to name. My research (and general sanity) has especially benefited from conversations with my colleagues and friends: Dr. Jessica Hsieh, Dr. Christian Crouzet, and Ben Lertsakdadet, who provided valuable perspectives and helpful advice. Thank you also to Linda McCarthy for going above and beyond to solve any problem and keeping our cell culture going. Additionally, thank you to Ann Fain for her care toward all students and especially for help fixing any and all administration issues.

I have been fortunate to have many collaborators during my research career. Thoughtful discussions with Professor Andrew Putnam and Professor Steven Weiss during our collaborations have been especially helpful with respect to developing my perspective both on my own research and the field at large. In no particular order, I would like to thank all my collaborators: Benjamin Juliar, Dr. Jessica Hsieh, Dr. Yen Kong, Dr. Janahan Arulmoli, Dr. Monica Romero-Lopez, Dr. Ashley Fong, Professor Christopher Hughes, Professor Ashley Brown, Professor Thomas Barker, Professor Wendy Liu, Professor Tranquillo, Professor Wendy Liu, Professor Anthony De Tomaso, Professor Lisa Flanagan, Professor Alex Levine. Additionally, thank you to all those who served on my committees both for my advancement to

candidacy and my defense committee: Professor Wendy Liu, Professor Michael Dennin, Professor Christopher Hughes, Professor Lisa Flanagan.

I cannot overstate how valuable the support of my friends and family has been throughout this process. Particularly the love and support of my mother, father, and brother who have helped me for (naturally) as long as I can remember. Without their help and dedication, I would never have gotten this far. Lastly, I must thank Andrea Navarro, who has reminded me to focus throughout my work, but also kept me sane by helping me to relax from time to time. She makes all the work worth it.

CURRICULUM VITAE

EDUCATION

University of California | Irvine, CA
Ph.D. Candidate, Biomedical Engineering – GPA: 3.97 Graduation: 2018
M.S. Biomedical Engineering 2016
B.S. Biomedical Engineering 2013

Awards: NSF Graduate Research Fellowship Program Honorable Mention 2015, Commendation from the City of Whittier 2015, Cardiovascular Applied Research and Entrepreneurship (CARE) Fellowship 2014-2016

Shibaura Institute of Technology | Tokyo, Japan
Robotics, Communications 2012

RESEARCH EXPERIENCE

Graduate Researcher – Ph.D. Candidate Aug 2013 – Aug 2018
Department of Biomedical Engineering | BEAMS Lab | UC Irvine

- Created and tested an automated active microrheology system to map pericellular rigidity between cells and their surrounding matrix through various cellular processes.
- Quantified the mechanics of magnetically aligned fibrin, showing the stiffness anisotropy that can be induced (collaboration with *Tranquillo Lab*).
- Investigated the micromechanical effects of interfering with fibrin polymerization via knob B mimics (collaboration with *Barker Lab*).
- Collaborations: *Barker Lab* (Georgia Tech), *Tranquillo Lab* (University of Minnesota), *Hughes Lab* (University of California, Irvine), *Putnam Lab* (University of Michigan), *Weiss Lab* (University of Michigan), *Flanagan Lab* (University of California, Irvine), *Liu Lab* (University of California, Irvine)

Undergraduate Researcher Mar 2012 – June 2013
Department of Biomedical Engineering | BEAMS Lab | UC Irvine

- Worked with Dr. Martha Alvarez-Elizondo to develop and automate control mechanisms and analysis software for new and existing instrumentation.

TEACHING EXPERIENCE

Teaching Assistant – Engineering Analysis and Design: Data Acquisition
BME60A | Department of Biomedical Engineering | University of California, Irvine Fall 2017

- Led a class of 138 students in designing, building, coding, and troubleshooting optical heart rate monitors and auto-focus systems.

Invited Guest Instructor – Integrative Approaches to Discovery in Molecular, Cell, and Developmental Biology
MCDB 192 | Department of Molecular, Cell, and Developmental Biology | UC Santa Barbara Summer 2017

- Instructed students on mechanobiology and methods of quantifying stiffness. Helped design experiments with students to test mechanically focused hypotheses utilizing a novel stiffening mechanism.

Workshop Leader – ALMA Science Academy Summer 2017
Madison Park Neighborhood Association | Santa Ana, CA

- Designed and taught a curriculum for elementary school students to build circuits and control them via an Arduino platform, culminating in them each building a heart rate monitor.

Lead Mentor – CardioStart Summer 2015
Edwards Lifesciences Center for Advanced Cardiovascular Technology (ELCACT) | University of California, Irvine

- Mentored high school students during a summer program in which they conducted an angiogenesis assay; supervised their quantification of budding vessels within petri-dishes and helped them present their findings.

Workshop Lead Instructor- Summer Science Camp Summer 2015

Team Science | Whittier, CA

- Devised and taught a curriculum for teaching robotics both programming and mechanical aspects to elementary and high school students; actively worked with students to troubleshoot any programming or electronic issues encountered

Teaching Assistant – Engineering Analysis and Design: Data Acquisition Fall 2014

BME60A | Department of Biomedical Engineering | University of California, Irvine

- Taught, lectured, and worked with a class of 131 students to provide hands on experience with data acquisition and automated systems.

Co-Lead Mentor – CardioStart Summer 2014

Edwards Lifesciences Center for Advanced Cardiovascular Technology (ELCACT) | UC Irvine

- Worked with high school students introducing them to Solidworks, 3D printing, 3D cell culture, and cell morphological analysis.

Workshop Assistant - Summer Science Camp Summer 2014

Team Science | Whittier, CA

- Aided in the instruction of fifth grade students actively learning about electricity and magnetism.

PUBLICATIONS

M.T. Keating, M. Lim, Q. Hu, E.L. Botvinick, Selective Stiffening of Fibrin Constructs with Micron Resolution Via Photo-Crosslinking. (2018). Under Revision. *Acta Biomatrerialia*.

M.T. Keating & B.A. Juliar, Y.P. Kong, E. L. Botvinick, and A. J. Putnam Sprouting angiogenesis induces significant mechanical heterogeneities and ECM stiffening across length scales in fibrin hydrogels. *Biomaterials* **162,** 99–108 (2018).

M. Keating, A. Kurup, M. Alvarez-Elizondo, A.J. Levine, E. Botvinick, Spatial distributions of pericellular stiffness in natural extracellular matrices are dependent on cell-mediated proteolysis and contractility, Acta Biomater. (2017). doi:10.1016/j.actbio.2017.05.008.

R.E. Gurlin, **M.T. Keating**, S. Li, J.R. Lakey, S. de Feraudy, B.S. Shergill, E.L. Botvinick, Vascularization and innervation of slits within polydimethylsiloxane sheets in the subcutaneous space of athymic nude mice, J. Tissue Eng. 8 (2017) 204173141769164. doi:10.1177/2041731417691645.

J. Arulmoli, H.J. Wright, D.T.T. Phan, U. Sheth, R.A. Que, G.A. Botten, **M. Keating**, E.L. Botvinick, M.M. Pathak, T.I. Zarembinski, D.S. Yanni, O. V. Razorenova, C.C.W. Hughes, L.A. Flanagan, Combination scaffolds of salmon fibrin, hyaluronic acid, and laminin for human neural stem cell and vascular tissue engineering, Acta Biomater. 43 (2016) 122–138. doi:10.1016/j.actbio.2016.07.043.

M. Romero-López, A.L. Trinh, A. Sobrino, M.M.S. Hatch, **M.T. Keating**, C. Fimbres, D.E. Lewis, P.D. Gershon, E.L. Botvinick, M. Digman, J.S. Lowengrub, C.C.W. Hughes, Recapitulating the human tumor microenvironment: Colon tumor-derived extracellular matrix promotes angiogenesis and tumor cell growth, Biomaterials. 116 (2016) 118–129. doi:10.1016/j.biomaterials.2016.11.034.

A.H. Fong, M. Romero-López, C.M. Heylman, **M. Keating**, D. Tran, A. Sobrino, A.Q. Tran, H.H. Pham, C. Fimbres, P.D. Gershon, E.L. Botvinick, S.C. George, C.C.W. Hughes, Three-Dimensional Adult Cardiac Extracellular Matrix Promotes Maturation of Human Induced Pluripotent Stem Cell-Derived Cardiomyocytes, Tissue Eng. Part A. 22 (2016) 1016–1025. doi:10.1089/ten.tea.2016.0027.

A. Kurup, S. Ravindranath, T. Tran, **M. Keating**, P. Gascard, L. Valdevit, T.D. Tlsty, E.L. Botvinick, Novel insights from 3D models: the pivotal role of physical symmetry in epithelial organization, Sci. Rep. 5 (2015) 15153. doi:10.1038/srep15153.

A.C. Brown, S.R. Baker, A.M. Douglas, **M. Keating**, M.B. Alvarez-Elizondo, E.L. Botvinick, M. Guthold, T.H. Barker, Molecular interference of fibrin's divalent polymerization mechanism enables modulation of multiscale material properties, Biomaterials. 49 (2015) 27–36. doi:10.1016/j.biomaterials.2015.01.010.

ORAL PRESENTATIONS

Keating, M., Kurup, A., Alvarez-Elizondo, M., Levine, A.J., Botvinick, E**.** "*Spatial distributions of pericellular stiffness in natural extracellular matrices are dependent on cell-mediated proteolysis and contractility*." University of California Systemwide Bioengineering Symposium. Los Angeles, CA. June 2017.

Keating, M. & Kurup, A., Alvarez, M., Botvinick, E. **"***Mapping Mechanical Properties of the Extra Cellular Matrix Surrounding Cells Cultured in 3D."* National Science Foundation: Workshop on the Quantitative Biology of Cytoskeletal Mechanics. Chicago, IL. 2015.

Keating, M., Kurup, A., Botvinick, E. "*Optical Characterization of Pericellular Mechanical Heterogeneity*" Frontiers in Optics 2015, the 99th Optical Society of America Annual Meeting. San Jose, CA. October, 2015.

Keating, M. & Kurup, A., Alvarez, M., Botvinick, E. "*Mapping Pericellular Stiffness of Naturally-derived Extra Cellular Matrix Around Cells Cultured in 3D*." Biomedical Engineering Society Annual Conference 2015. Tampa, FL. October, 2015.

Keating, M., Kurup, A., Alvarez, M., Botvinick, E. "*Mapping Mechanical Properties of the Extra Cellular Matrix Surrounding Cells Cultured in 3D."* Trends in Optical Micromanipulation III. Universitätszentrum Obergurgl. Obergurgl, Austria. January 2015.

Keating, M. & Kurup, A. , Alvarez, M., Botvinick, E. "*Quantifying Change in Stiffness Heterogeneity in 3D Around Cells Embedded in Natural ECMs Over Time*." International Society of Optics Photonics: Nanoscience + Engineering. San Diego, CA. August 2014.

Botvinick, E., Alvarez, M., Kurup, A., **Keating, M.** "*Mapping Mechanical Properties of the Extra Cellular Matrix Surrounding Cells Cultured in 3D.*" Biophysical Society 58th Annual Meeting. February 2014.

Alvarez, M., Kurup, A., **Keating, M.**, Botvinick, E. "*Automatic Optical Tweezers Based Active Microrheology*." Biomedical Engineering Society Annual Conference 2013. Seattle, WA. September 2013.

POSTER PRESENTATIONS

Keating, M. & Kurup, A., Alvarez-Elizondo, M., Botvinick, E. "*The Dependence of Pericellular Stiffness Spatial Distributions on Cell-Mediated Proteolysis and Contractility in a Naturally Derived Extracellular Matrix*." Biophysical Society 62nd Annual Meeting. San Francisco, CA. Feb 2018.

Keating, M., Riemenschneider, S., Botvinick, E., Tranquillo, R. "*Active Microrheology of Magnetically-aligned Fibrin Gel to Measure Stiffness Anisotropy*." Society for Biomaterials. Charlotte, NC. April 2015.

Keating, M. & Kurup, A., Alvarez, M., Botvinick, E. "*Quantifying Change in Stiffness Heterogeneity in 3D Around Cells Embedded in Natural ECMs*." UC Systemwide Bioengineering Symposium. Irvine, CA. June 2014.

AFFILIATIONS

Biomedical Engineering Society (BMES), International Society of Optics and Photonics (SPIE), Edwards Lifesciences Center for Advanced Cardiovascular Technology (ELCACT)

CERTIFICATION & TRAINING

Mammalian Cell Culture; HIPAA 101, Information Security; Bloodborne Pathogens; Fume Hood Safety; Fire Extinguisher Safety; Hazardous Waste; Formaldehyde Safety; Compressed Gas Safety; Shipping Hazardous Materials: Dry Ice; UC Ethical Values and Conduct; Laboratory Core Safety; Laser Safety; Radiation Safety

MISCELLANEOUS SKILLS

Software: MATLAB, LabVIEW, Mathematica, ImageJ, FIJI, SolidWorks, OriginPro, Minitab, GraphPad, Adobe Photoshop, Adobe Illustrator, Premiere Pro, Cinema4D, Javascript, Java, C++

Mechanical:	Optical Tweezers (both use and design/construction), Active/Passive Microrheology, General Machining (Milling, Lathing, Drill Pressing, Band Sawing etc.), 3D Printing (SL and AM, design, use, and maintenance)
Cell Culture:	Aseptic techniques, Mammalian cell culture, 2D/3D cell culture, Hydrogels (Collagen, Fibrin, Gelatin), PDMS, Bead Assay for Angiogenesis
Microscopy:	Fluorescence and Reflection Confocal, Multi-photon, Optical Systems

ABSTRACT OF THE DISSERTATION

Measuring and Understanding Pericellular Stiffness

By

Mark Thomas Keating

Doctor of Philosophy in Biomedical Engineering

University of California, Irvine, 2018

Professor Elliot L. Botvinick, Chair

While tissue stiffness is thought to play a role in regulation of cellular behavior, for the most part, stiffness is measured at the bulk level. The bulk measurement masks microscale dynamics within the fibrous extracellular matrix (ECM) and is insensitive to changes as cells remodel their local ECM. In order to investigate, cell-ECM dynamics I have developed an automated active microrheology (AMR) system and used it to probe the ECM near both single, isolated cells and multi-cell angiogenic sprouts, quantifying the pericellular distribution of stiffness. Additionally, I developed a new technique to modify stiffness within the ECM, at a scale relevant to the pericellular distribution of stiffness.

My work shows that both human fibroblasts and smooth muscle cells establish a complex heterogeneous pericellular stiffness landscape. As expected, cell contraction strain hardened the matrix, but surprisingly, cells must also be competent in ECM proteolysis, which is to say the matrix must be broken down for cell-mediated stiffening. My findings suggest pericellular stiffness distributions should be considered in the study of cell-ECM interactions.

In collaboration with Professor Andrew Putnam, I measured the evolution of stiffness change within a capillary morphogenesis model over time. We applied both bulk rheology and AMR to measure stiffness at different length scales. This data highlighted that bulk rheology was dominated by the activity of supportive stromal cells but blinded to the stiffness heterogeneity found proximal to vessels via AMR. These findings underscore that characterizing ECM mechanics across length scales can provide a deeper understanding of the microenvironment's role within these complex processes.

Lastly, I developed and evaluated a method to modify stiffness within fibrin matrices at the micron-scale. This method allows for a patterning of stiffness at a spatial scale and magnitude similar to that observed by cell-mediated stiffening. By using ruthenium-catalyzed photo-crosslinking coupled with our laser scanning confocal microscope, we can selectively illuminate and thereby selectively crosslink regions of interest within the volume of a hydrogel. This results in a stiffness increase of up to 25X, with a steep stiffness gradient in the surrounding area. Selective crosslinking could be of great utility in creating more complex patterns of stiffness, which could be invaluable for the investigation of mechanotransduction within a natural 3D ECM context.

Collectively, these works show that the mechanical topography surrounding cells within ECM is varied and must be considered in future study of mechanically driven hypotheses. Microrheology in combination with selective photo-crosslinking provides a new tool to better understand roles for tissue stiffness in cell regulation, and vice versa.

CHAPTER 1:CHAPTER 1: INTRODUCTION AND BACKGROUND

Cells found *in vivo* are often surrounded by a mesh of molecular networks forming a mechanical scaffold called the extracellular matrix (ECM). Interactions between cells and their surrounding ECM have been shown to play a crucial role in both cellular and tissue homeostasis. Cells sense the stiffness of their native ECM primarily via the integrin family of transmembrane proteins - the cellular mechanoreceptors that physically couple the host cells to the ECM. The integrins are critical in transducing extracellular mechanical stresses into chemical signaling in the cells[1]. In recent years these interactions are increasingly being alluded to in cancer pathology, for example, as mechanical interactions with the matrix are implicated in tumorigenesis[2] as well as mesenchymal stem cell (MSC) differentiation and proliferation[3,4]. Importantly, cells do not just react to the matrix they inhabit - they actively modify it through degradation via matrix metalloproteinase activity, cellular contractility, and deposition of *de novo* matrix components[5]. This poses a complex push-pull system in which it is difficult to describe cell-matrix interaction from a single snapshot in time.

While the ECM has other measurable properties such as density or porosity, the elusive ECM stiffness has also been implicated in many cellular processes such migration, proliferation, and differentiation[6–8]. However, in these studies, stiffness is typically not assessed at the spatial scale of a cell, presumably stripping much of the nuance out of the interaction between a cell and its surrounding environment and likely masking critical determinants of cell behavior. This work focuses on the quantification of distributions of stiffness at around cells and presents a new technique to modify those stiffness distributions at relevant scales.

1.1 THE EXTRACELLULAR MATRIX

Many cell types *in vivo* are surrounded by an extracellular matrix (ECM), the molecular and mechanical scaffolding of natural tissues. The ECM is composed of fibrous proteins, proteoglycans, and glycoproteins that are diverse in both structure and function[5,6]. The ECM actively regulates the behaviors of cells, influencing many essential cellular processes including proliferation, migration, and differentiation[6–8]. The complex chemical and physical properties of the matrix, sensed by resident cells, contribute to this modulation of cellular behavior. An overview of this is shown in **Figure 1.1**.

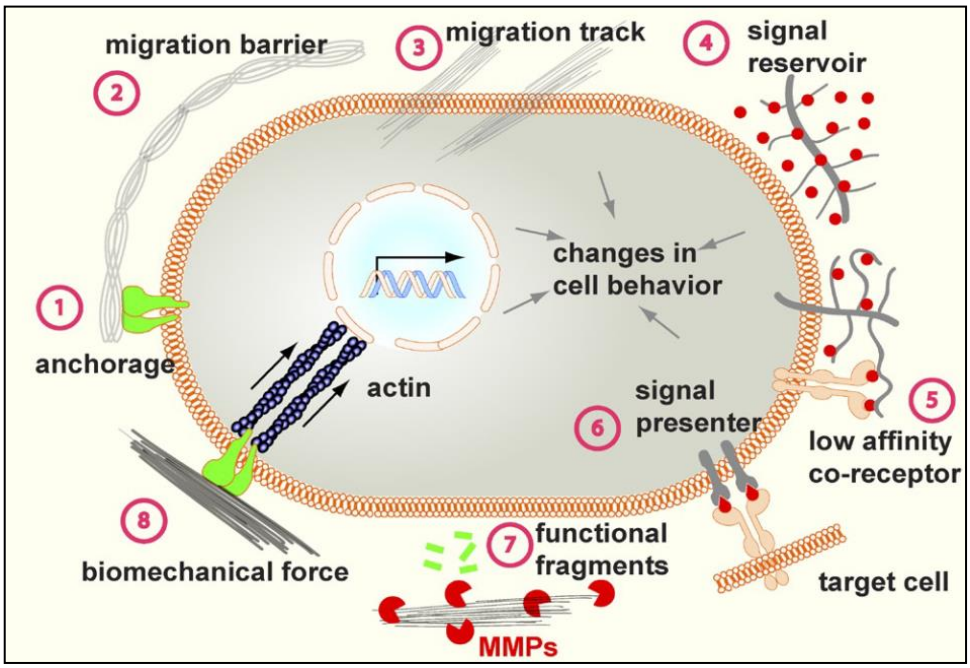

Figure 1.1*: Cells and their surrounding ECM can interact in a variety of ways that affect both the matrix and cell behavior*[89].

On the chemical side, the ECM can act as a reservoir for morphogens or as a mechanism for their presentation. ECMs have been shown to contain growth factors ranging from bone morphogenetic proteins (BMPs) to Wnts[5,9]. On the mechanical/structural side, the ECM provides a meshwork scaffold with adhesion sites for cell linkage and acts as conduit for force transmission[7]. Importantly, cells can remodel their local ECM environment through the use of contractility-mediated force, matrix breakdown via matrix metalloproteinases (MMPs), deposition of new ECM, or cross-linking of existing ECM[6,7,10]. Mechanical changes, such as changes in material stiffness, created during this interaction can then affect the cell, establishing a feedback loop, which is highlighted in **Figure 1.2**. Stiffness of the ECM has been implicated in several cellular processes *in vitro,* including proliferation and differentiation[10–13]. The ECM is viscoelastic, having both elastic and viscous material properties[14,15]. *In vitro,* ECMs have been used both as a 2D substrate and a 3D scaffold. Importantly, cells behave differently in two dimensions versus three dimensions, with three dimensional cell culture thought to better recapitulate the *in vivo* microenvironment[16–18].

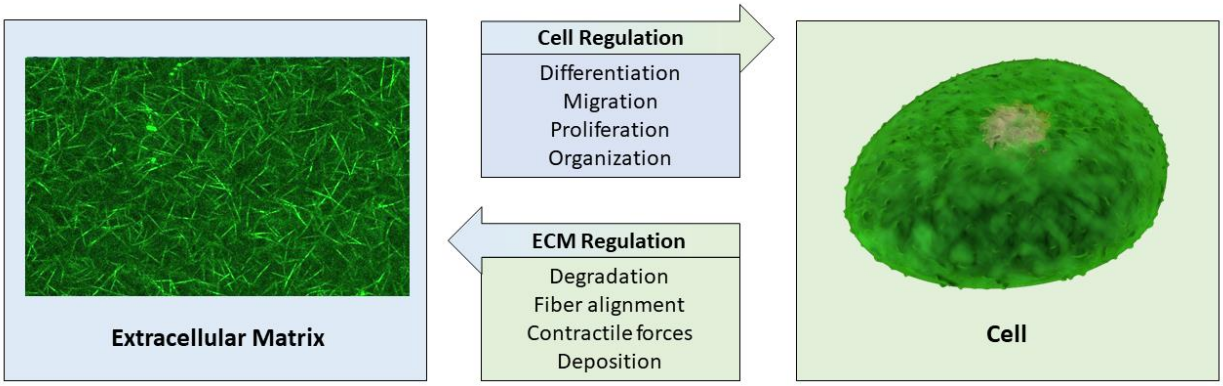

Figure 1.2*: Cells both react to and modify their surrounding ECM.*

1.1.1 Fibrin

One fibrous protein that can form an extracellular matrix is fibrin. Fibrin is an essential component of blood clots, making up a significant portion of the provisional matrix during wound

healing[19]. A fibrin matrix is formed when thrombin cleaves the fibrin precursor, fibrinogen, which is typically found in the blood at a concentration of 2.5 mg/mL[20,21]. Fibrinogen is a dimeric, 340kDa glycoprotein.

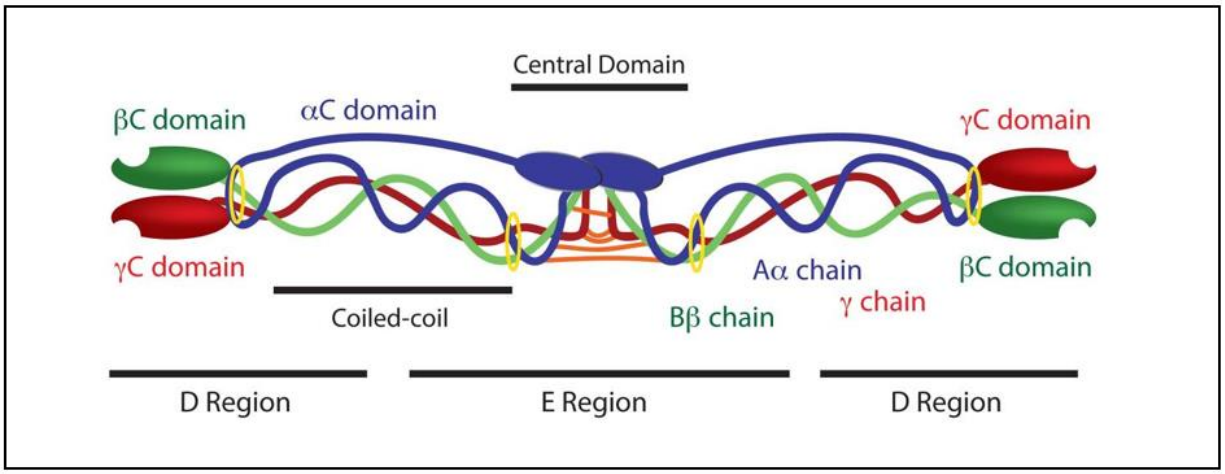

***Figure 1.3**: The structure of fibrinogen* [22].

The structure of fibrinogen is shown in **Figure 1.3**, where each dimer is composed of polypeptide chains called Aα, Bβ, and γ[22]. These dimers are connected to each other at the central domain by disulfide bridges[23]. On the distal ends of the molecule βC and γC domains, which are, respectively connected to the Bβ, and γ chains, , with αC domains connecting opposing βC and γC domains to the central domain[24]. Fibrinogen's structure can also be subdivided by the units created during plasminolysis, which are referred to as the two D and one E regions[22]. As previously mentioned, thrombin cleaves fibrinogen to make a fibrin. Thrombin does this via catalyzing the hydrolysis of fibrinopeptides A and B, which releases the αC domain from the central domain, exposing binding sites that can interact with the distal domains of βC and γC[25]. This creates fibrin monomers which can then assemble to create protofibrils, which can further associate laterally to make multi-stranded fibers and branching junctions, creating a reticular structure[23]. *In vitro* fibrin,

sometimes in combination with other ECM proteins, has been used as a method of studying angiogenesis[26], stem cells[27,28], macrophages[29], and cancer cell lines[30], to name a few. It has also been utilized as a delivery mechanism for therapies *in vivo*[31].

Fibrin is subject to cell-mediated degradation, and is replaced with granulation tissue in a wound healing environment[32]. Fibrin is susceptible to proteolytic cleavage via serine protease plasmin, which is activated from its precursor state plasminogen via enzymes such as tissue plasminogen activator (tPA) or urokinase plasminogen activator (uPA)[33]. While plasminogen production *in vivo* is thought to generally occur in the liver, cells active in the tissue repair process such as fibroblasts have also been shown to produce plasminogen[34,35]. Additionally, fibrin is also susceptible to proteolysis via some membrane tethered matrix metalloproteinases (MT-MMPs): MT1-MMP (MMP-14), MT5-MMP (MMP-24), MT6-MMP (MMP-25)[5].

1.1.2 Collagen

Another type of ECM is collagen. Collagen has a variety of types and is the most abundant protein within humans, with Collagen Type I being the most prolific, as one of the main structural proteins of ECM within the body[36]. In vertebrates, there are at least 28 different types of collagen which can vary both in structural assembly and where they are found in the body[37]. While some variation exists between collagen types, structurally collagen is composed of three polypeptide alpha chains wound into a superhelix, in a fashion similar to rope[6]. When produced intracellularly, this triple-helix structure initially has amino- and carboxyl-terminated on either end and is termed procollagen. Upon secretion into the extracellular space and metalloproteinase mediated cleavage of the amino and carboxyl ends, creating the collagen molecule[38]. This molecule can then self-assemble to create fibrils, stabilized by covalent crosslinks, as shown in **Figure 1.4A**[39]. These can aggregate into an interconnected fibrous network, as shown in **Figure 1.4B**.

In studying cells within collagen ECMs *in vitro*, collagen is often extracted from tissue via pepsin or an acid extraction process and then reconstituted via a pH and temperature mediated process, with cells either embedded within the network or added to the top of the gel following polymerization[40,41]. This is typically done with collagen I, as it is the most abundant and cost-effective[42]. Utilizing collagen in this way allows the study of cells in 3D culture, in a material that mimics the natural ECM and is inherently biocompatible and permissive to cellular modification[43]. Remodeling of ECM by cells requires degradation. Matrix metalloproteinases (MMPs) are primarily responsible for this degradation. For Collagen I, the primary MMPs acting to break down the matrix are MMP-1, MMP-8, partially MMP-9, MMP-13, and MMP-14 (also known as Membrane Tethered, MT1-MMP)[5]. The arrangement and organization of ECM components can greatly influence both the stiffness a cell feels and the most basic components of cell behaviors, but, importantly, these features of the ECM change as a result of cell activities - through MMPs and cellular contractile forces[5]. However, ECM architecture does not always correlate well with stiffness at the micro scale. Our lab has previously shown that architecture (assessed by pore size) is poorly correlated with changes in micro level stiffness[44]. Another group made similar

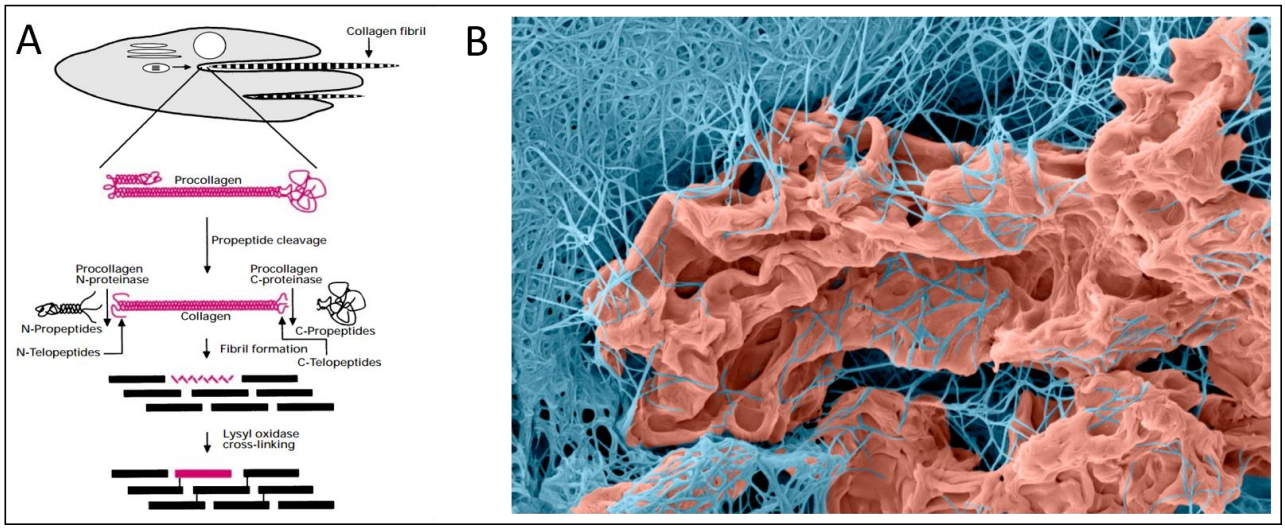

Figure 1.4*: (A) Collagen formation schematic* [39]*. (B) Psuedocolored SEM image of a fibrosarcoma (orange) in a type I collagen network* [40]*.*

observations in collagen, where micro level stiffness as assessed by atomic force microscopy did not fully correlate with collagen density[45]. Observations such as these have shown the need for a measurement of stiffness at this level, which is exactly the realm that microrheology can assess.

1.2 MECHANOBIOLOGY

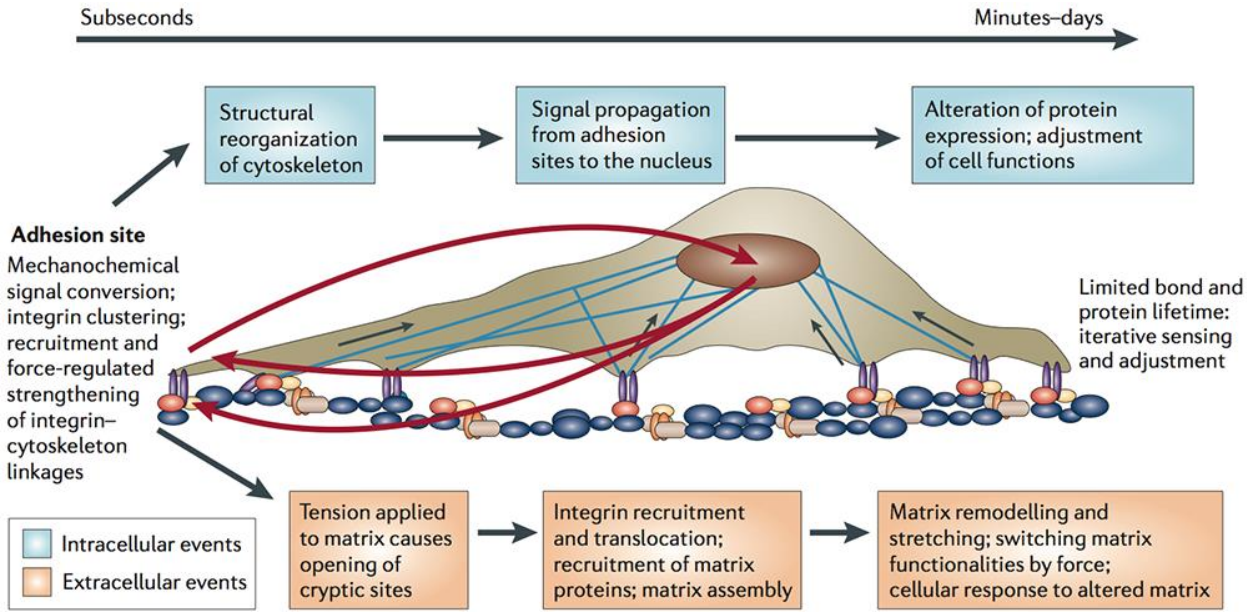

Figure 1.5*: Cell-mediated Interactions with the ECM and their relative time scales*[90].

As previously stated, cells both sense and react to the mechanics of their surrounding environment. Mechanobiology is the study of this process, which encompasses mechanical forces influencing cells, from fluid flow to cell-cell interactions. With respect to cells and their ECM, cells can sense the stiffness of their native ECM primarily via the integrin family of transmembrane proteins. Integrins are the most studied cellular mechanoreceptors, physically coupling the actin cytoskeleton of cells to the ECM[46]. Integrins are critical in transducing extracellular mechanical stresses into chemical signaling in the cells[1]. **Figure 1.5** shows these cell-mediated interactions, along with their relative time scales. However, it is important to note that there are other, non-integrin mechanoreceptors such as stretch activated ion channels, enzyme-linked receptors, lipid rafts and glycocalyx[47]. *In vitro*, mechanobiology can be studied in either 2D or 3D, with cells either

grown atop a substrate or within a material, typically a hydrogel. Importantly, cellular behavior is not the same between 2D and 3D culture, with 3D thought to better recapitulate the *in vivo* case[17,48].

Many cell types have been shown to be mechanoresponsive. Mesenchymal stem cells (MSCs), for example, were shown to upregulate different genetic fate markers when grown on substrates of varying stiffness[12], results which were expanded to 3D culture as well[49,50]. In fact, there are many studies that characterized the effect of ECM properties on the behavior of MSCs [51–57]. As previously stated however, these interactions are complex and not unidirectional. For instance, our lab previously studied these cells in collaboration with the Weiss Lab, showing that proteolytic degradation via MT1-MMP is necessary for cell fate decisions[58].

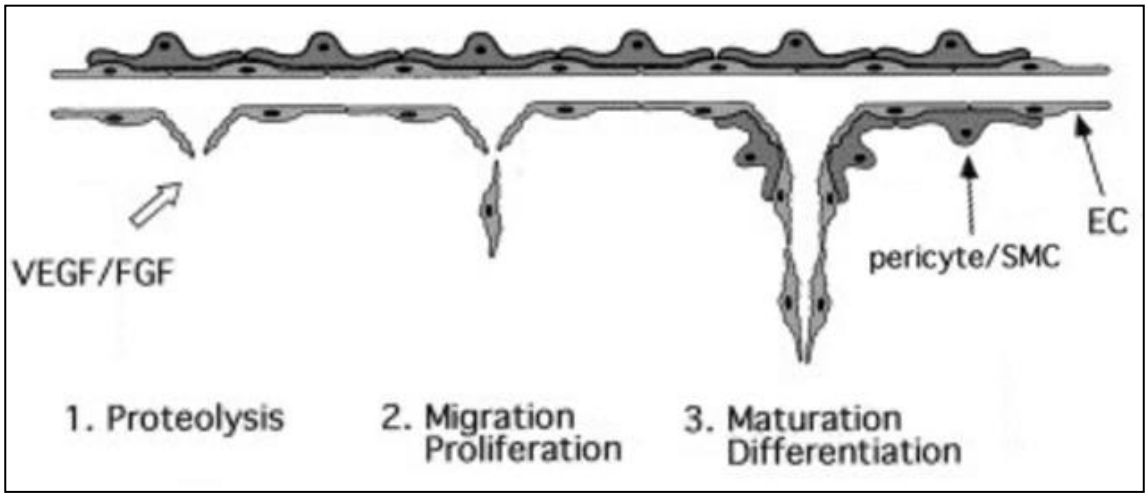

Figure 1.6: Diagram of Stages of Angiogenesis (Adapted from [91])

1.2.1 Mechanobiology of Angiogenesis

The creation of new blood vessel via sprouting from existing vasculature, angiogenesis, (also known as neovascularization), is an essential biological function. Control of such is critical to successful tissue engineering as well as treating many diseases. Angiogenesis is a complex, highly regulated biological process, particularly *in vivo*. Currently, there are two classes of angiogenesis: intussusceptive angiogenesis and sprouting angiogenesis. Intussusceptive

angiogenesis is the splitting of a larger vessel into smaller vessels and appears to be important during embryonic development, for creating specific vessel arrangements to assist organogenesis[59]. The process of sprouting angiogenesis has three primary stages which are illustrated in **Figure 1.6**: Activation of receptors in endothelial cells by angiogenic growth factors (such as VEGF[60]), proteolytic degradation of the existing vessel's basement membrane followed by endothelial cell migration and polarization to form an immature vessel with a hollow lumen[61]. Recruitment of supporting cells and ECM synthesis can then stabilize these nascent vessels[62]. Vessels anastomose with other vessels so as to complete a vascular circuit[63]. Endothelial cells, which make up the vessel walls are morphologically differentiated into tip cells or stalk cells by Notch-Dll4/Jag1 signaling axis which is in turn induced by VEGF signaling[64–66]. The formation of the sprout is led by the tip cell, which tends to migrate toward VEGF, or is replaced by another cell via a Notch-related feedback loop[67]. The stalk cells proliferate as they trail the tip cells and form the characteristic vessel lumen[68].

While significant work has gone into characterizing the role of chemical initiation and modification of angiogenesis, the role of ECM mechanics and microenvironment in angiogenic context in the context of angiogenesis is not well elucidated[69]. Matrix stiffness, as measured at the bulk level, has been shown affect angiogenesis - such as modulating vessel growth *in vitro*[70–74], or modifying the response of ECs to VEGF[75]. However, these mechanical theories are justified by experiments done using bulk characterization of ECM stiffness. Considering that we have previously demonstrated that ECM microenvironment around cells exhibits significant mechanical heterogeneity, bulk rheological measurements cannot be considered as a proxy for studying mechanical hypotheses of cells, especially around microvasculature during angiogenesis[44,76].

1.3 MICRORHEOLOGY

Studies relating the stiffness of ECM and cellular behavior or phenotypes have typically been done by only measuring initial bulk mechanical properties. Rheology is the study of material response in terms of elastic and viscous deformation to an applied stress and is typically studied using a mechanical rheometer (such as a parallel plate rheometer). In contrast, microrheology is a process in which the mechanical properties of a complex fluid are calculated based on the motion of embedded, typically spherical, probes, allowing for measurement of micron-scale material heterogeneities[15,77]. Within 3D biological systems, variations of this technique have been used previously to study the mechanical properties within biological systems such as a cell cytoplasm, fibrin, and collagen[44,78,79].

1.3.1 Passive and Active Microrheology

Microrheology techniques can be divided into passive microrheology (PMR) and active microrheology (AMR). PMR relies on the thermal motion of probe particles to extract material properties, while in AMR, the probe particles are driven by external forces[77]. Particle detection in both cases is typically done by either video microscopy or by a laser detection system[15]. While PMR is typically easier and less expensive to implement, it must be conducted with an assumption of thermodynamic equilibrium, it is more sensitive to noise, and it typically has a limited measurable maximum elastic modulus magnitude compared to AMR[15,80,81].

In AMR, probe particles can be driven using magnetic, optical, or micromechanical force. This document will focus on optical tweezer-based AMR, which can operate within the volume of the ECM. In brief, optical tweezers use a focused Gaussian laser beam (trapping beam) to capture and manipulate probe particles[82,83]. As rays of light pass through the spherical probe particle, the momentum change of the rays creates a force toward the focus of the laser, which reaches a stable

equilibrium when the trapped particle is in the trapping beam's focus[84,85]. A linear Hookean spring model can be used for to calculate displacements from the trap's center, as long as displacements are small[15,86]. Within an ECM, with spherical probe particles embedded, an individual particle can be oscillated sinusoidally, resulting in the surrounding matrix dissipating this energy through elastic and viscous means. This dissipation is reflected in an amplitude and phase modulation of the probe particle's motion relative to that of the trapping beam. The complex shear modulus G* for the local area can be calculated based on these phase amplitude modulations between the input trapping beam motion and the resulting motion of the particle, which will be detailed below[87].

1.3.2 Optical Tweezers System Description

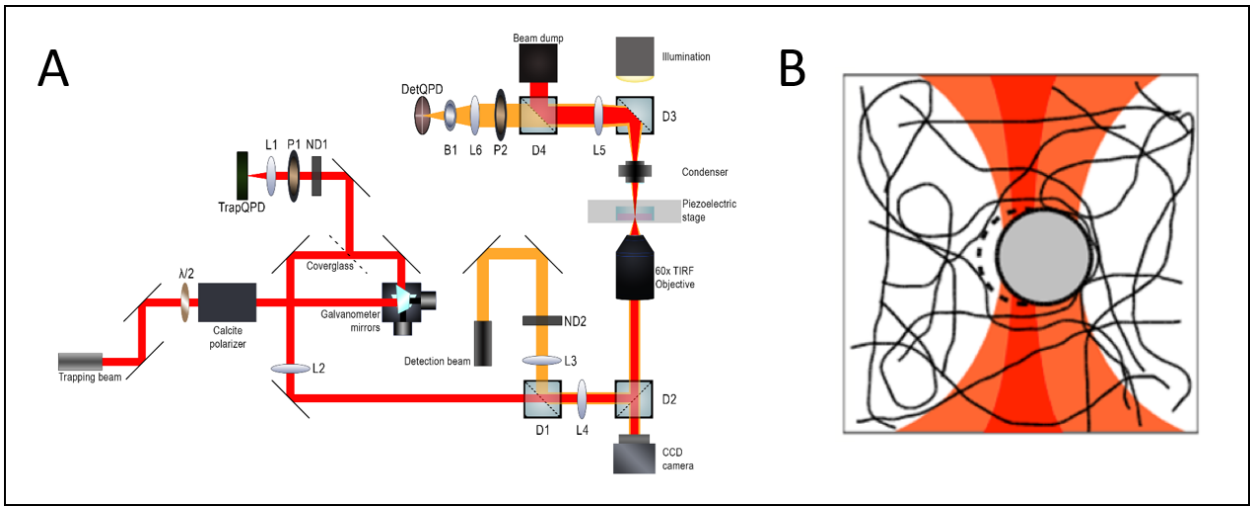

Figure 1.7: (A) Diagram of optical tweezers system. Optical components: λ/2 (half-wave plate), L (Lens), P (linear polarizer), D (dichroic mirror) and ND (neutral density filter). 1064nm trapping beam is depicted in red while the stationary, 785nm detection beam is depicted in orange. Beam expansion caused by lens pairs L2/L3 and L3/L4 is omitted from this diagram for simplicity. (B) Schematic diagram of a microbead probe being displaced by a trapping beam (orange) while motion is detected by the stationary detection beam (red) (Adapted from [44])

Active microrheology is conducted in the Botvinick Lab using a two-laser optical tweezers system. The diagram of the system is shown in **Figure 1.7A** and is a modification upon the previously described system[44]. A schematic diagram of the system displacing the probe bead within a fibrous ECM is shown in **Figure 1.7B.** The system is mounted on top of a SMART Table

(Newport) which dampens vibrations. In this system, a 1064nm is used as the trapping laser. Laser power is reduced via a polarization-based variable attenuator composed of a half wave plate and calcite polarizer. A pair of galvanometer mirrors steer the beam. A piece of cover glass reflects a small percent of the steered beam, which passes through a neutral density filter (ND1) and linear polarizer (P1). A lens (L1) then focuses the beam onto a quadrant photodiode (trapQPD). This allows for the sinusoidal motion of the trapping beam to be measured. A telescoping lens system (L2 and L4) then expands the beam and a second, stationary, 785nm laser is passed through a neutral density filter (ND2) and a telescoping lens system (L3 and L4). These two telescoping lens systems are to ensure the beam overfills the back aperture of the objective. The paths of the two lasers are combined at a dichroic (D1), where they are co-aligned. The co-aligned beams reflect off of another dichroic (D2) and both beams are focused into the sample plane via a 1.45NA 60X TIRF Oil Objective (Olympus).

For AMR, a probe particle within the sample plane will be centered in both the detection and trapping beams as the trapping beam is oscillated. Motion of the particle will cause subtle deflection of the detection beam. Both beams then pass through microscope condenser, where they reflect off of a dichroic (D3) and are collimated by a lens (L5). Another dichroic (D4) splits the trapping beam into a beam dump, while the detection beam is focused onto a second quadrant photodiode (detQPD) by lens L6, through a linear polarizer (P2) and through a bandpass filter (B1). Here the deflections caused by the response of the probe particle or microbead are detected.

1.3.3 Calibration and Calculation of the Complex Shear Modulus

Deflections of the detection beam are linear for small oscillations; however, this depends on particle size. For 2 μm microbeads, which are typically used in probing the ECM, this amplitude was empirically determined to be approximately 0.25 μm with our system. Before use of the

system each time, the system is calibrated with a water sample containing a dilute number of microbeads. Briefly, beams are co-aligned, (typically slight adjustment is necessary to ensure proper co-alignment) and the linear response of the detection beam deflection to the trapping beam's oscillation is optimized. Once this is done, optical trap stiffness (k_t) is determined via power spectrum method. In the power spectrum method, Brownian motion of the trapped microbead is measured by trapping a bead and sampling signals from detQPD at 100kHz for 30 seconds. A Lorentzian function is fit to the power spectrum of this signal, and the corner frequency (f_c) from that fit is used to calculate trap stiffness according to **Eq. (1)**, with the viscous drag coefficient γ calculated by **Eq. (2)** [88].

$$\boldsymbol{k_t = f_c 2\pi\gamma} \qquad (1)$$

$$\boldsymbol{\gamma = 6\pi\eta r} \qquad (2)$$

where η the viscosity of water and r the radius of the bead. For calibration measurements in water, the trap is driven slowly with a frequency of 0.1Hz in a triangle wave, at more than double the amplitude of a measurement oscillation (0.4 μm). Signals on both the trapQPD and detQPD during this oscillation are used to establish a volt to meter conversion for both signals. A standard AMR measurement is then conducted to ensure that the calculated viscosity matches with the theoretical viscosity of water at that temperature, within a reasonable margin of error. These calibrations are conducted in triplicate for every height that AMR will be conducted at within the sample.

Calculation of the complex shear modulus follows what has been previously done both within the field and our lab [17,44,81,87]. Briefly here, the calibrated signals from trapQPD and detQPD, correspond to trapping beam position and bead position. A function representing each, respectively, $x_t(t)$ and $x_b(t)$ is shown in **Equations (3)** and **(4)**,

calculated via a Fourier transform of the signal:

$$\boldsymbol{x_t(t) = A_t\, sin(\,\omega t)} \tag{3}$$

$$\boldsymbol{x_b(t) = A_b\, sin[\,\omega t - \theta_b(\omega)} \tag{4}$$

Here the $\boldsymbol{A_t}$ is the amplitude of the Fourier transform at frequency of the driving motion, $\boldsymbol{\omega}$. $\boldsymbol{A_b}$ is the amplitude of the Fourier transform of the bead motion at the driving frequency and $\boldsymbol{\theta_b(\omega)}$ is the phase lag[44]. The phase lag and attenuated amplitude in $x_b(t)$ is caused by the local material resistance. The force function ($\boldsymbol{x_f(t)}$) can be calculated from **Eq.(5)**, taking the difference of the two position functions and multiplying by the trap stiffness κ_t.

$$\boldsymbol{x_f(t) = k_t\,(x_t(t) - \,x_b(t)\,) = \,A_f\, sin[\omega t - \theta_f(\omega)]} \tag{5}$$

Here $\boldsymbol{A_f}$ is the amplitude of the force function and $\theta_f(\omega)$ is the phase lag between the force function and the trap position function[44]. The apparent complex response function $A(\omega)$ is calculated by **Eq. (6)** [81]:

$$\boldsymbol{A(\omega)\ = \frac{x_b(\omega)}{x_f(\omega)}} \tag{6}$$

Respectively, $\boldsymbol{x_b(\omega)}$ and $\boldsymbol{x_f(\omega)}$ are the Fourier transforms of $x_b(t)$ and $\boldsymbol{x_f}(t)$. Contributions of the trap to the apparent complex response can be corrected for in **Eq.(7)**, resulting in the corrected response function $\alpha(\omega)$.

$$\boldsymbol{\alpha(\omega) = \frac{A(\omega)}{1 - k_t A(\omega)}} \tag{7}$$

The contribution of the detection beam to this equation is negligible because it is an order of magnitude lower in terms of trap stiffness, so for this portion we only use k_t as oppose to $k_t + k_d$, where k_d is the trap stiffness of the detection beam[81]. The generalized Stokes equation can then be used to compute the complex shear modulus shown in **Equation (8)** [81]. As shown in **Equation (9)**, $G(\omega)$ is complex and can be broken down into the real and imaginary components $G'(\omega)$ and $G''(\omega)$, which, respectively, are the elastic and loss modulus. Important to note, however, this conversion from $\alpha(\omega)$ to $G(\omega)$ relies on an assumption of a continuum between the particle and

$$\boldsymbol{G(\omega) = \frac{1}{6\pi r \alpha(\omega)}} \qquad (8)$$

$$\boldsymbol{G(\omega) = G'(\omega) + iG''(\omega)} \qquad (9)$$

the surrounding material[77], this does not hold within a fibrous matrix. However, given the ubiquity

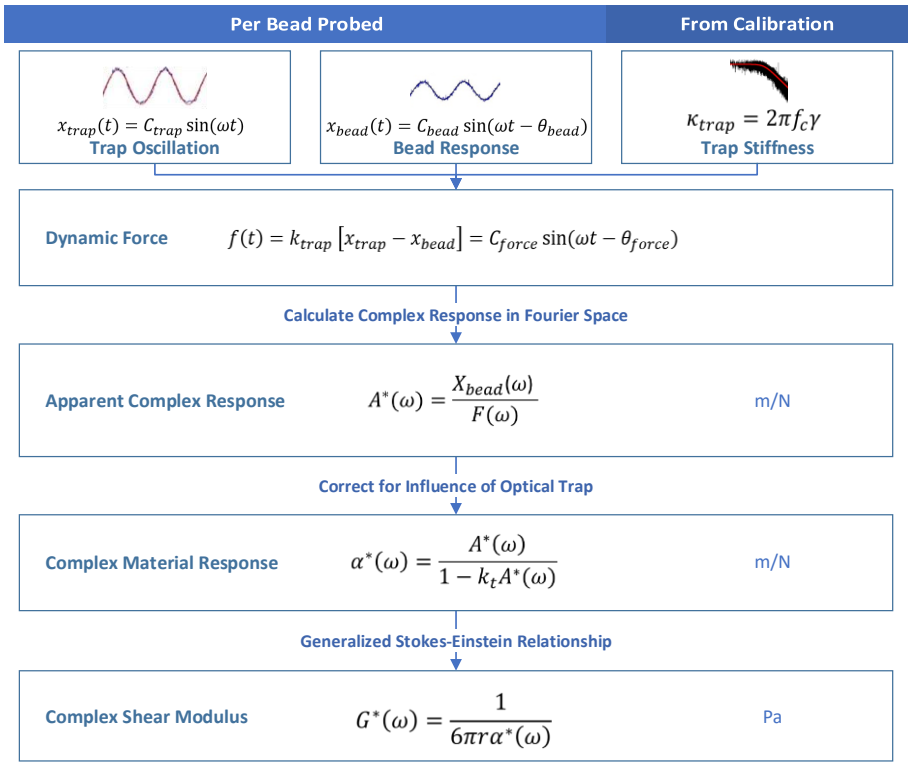

***Figure 1.8**: Process diagram for computing material properties from AMR measurements. Equations from* [81,87] .

of $G(\omega)$ within tissue mechanics and the reversibility of the operation, our lab has opted to report $G(\omega)$ for these measurements for comparison purposes, acknowledging the erroneous assumption being made. These values can also be reported as $1/\alpha'$ values with units of nN/μm, which precludes the need for a continuum assumption. The process for computing material properties from AMR data is summed up in **Figure 1.8**.

1.4 REFERENCES

1. Katsumi, A., Orr, A. W., Tzima, E. & Schwartz, M. A. Integrins in Mechanotransduction. *J. Biol. Chem.* **279,** 12001–12004 (2004).
2. Paszek, M. J. *et al.* Tensional homeostasis and the malignant phenotype. *Cancer Cell* **8,** 241–254 (2005).
3. Trappmann, B. *et al.* Extracellular-matrix tethering regulates stem-cell fate. *Nat. Mater.* **11,** 742–742 (2012).
4. Kshitiz *et al.* Control of stem cell fate and function by engineering physical microenvironments. *Integr. Biol. (Camb).* **4,** 1008–18 (2012).
5. Lu, P., Takai, K., Weaver, V. M. & Werb, Z. Extracellular matrix degradation and remodeling in development and disease. *Cold Spring Harb Perspect Biol* **3,** 1–24 (2011).
6. Alberts, B. *et al. Molecular Biology of the Cell*. (Garland Science, 2014).
7. Humphrey, J. D., Dufresne, E. R. & Schwartz, M. A. Mechanotransduction and extracellular matrix homeostasis. *Nat. Rev. Mol. Cell Biol.* **15,** 802–812 (2014).
8. Hynes, R. O. The Extracellular Matrix: Not Just Pretty Fibrils. *Science (80-.).* **326,** 1216–1219 (2009).
9. Rozario, T. & DeSimone, D. W. The extracellular matrix in development and morphogenesis: A dynamic view. *Dev. Biol.* **341,** 126–140 (2010).
10. Mason, B. N., Califano, J. P. & Reinhart-King, C. A. Matrix Stiffness: A Regulator of Cellular Behavior and Tissue Formation. in *Engineering Biomaterials for Regenerative Medicine* 19–37 (Springer New York, 2012). doi:10.1007/978-1-4614-1080-5_2
11. Provenzano, P. P. & Keely, P. J. Mechanical signaling through the cytoskeleton regulates cell proliferation by coordinated focal adhesion and Rho GTPase signaling. *J. Cell Sci.* **124,** 1195–1205 (2011).
12. Engler, A. J., Sen, S., Sweeney, H. L. & Discher, D. E. Matrix Elasticity Directs Stem Cell Lineage Specification. *Cell* **126,** 677–689 (2006).
13. Wei, S. C. *et al.* Matrix stiffness drives epithelial-mesenchymal transition and tumour metastasis through a TWIST1-G3BP2 mechanotransduction pathway. *Nat. Cell Biol.* **17,** 678–88 (2015).
14. Xu, X. & Safran, S. A. Nonlinearities of biopolymer gels increase the range of force transmission. *Phys. Rev. E* **92,** 032728 (2015).
15. Gardel, M. L., Valentine, M. T. & Weitz, D. A. Microrheology. *Microscale Diagnostic Tech.* 1–49 (2005). doi:10.1007/3-540-26449-3_1
16. Benton, G., George, J., Kleinman, H. K. & Arnaoutova, I. P. Advancing science and technology via 3D culture on basement membrane matrix. *J. Cell. Physiol.* **221,** 18–25 (2009).
17. Kurup, A. *et al.* Novel insights from 3D models: the pivotal role of physical symmetry in epithelial organization. *Sci. Rep.* **5,** 15153 (2015).
18. Tang, Y. *et al.* MT1-MMP-Dependent Control of Skeletal Stem Cell Commitment via a β1-Integrin/YAP/TAZ Signaling Axis. *Dev. Cell* **25,** 402–416 (2013).
19. Clark, R. A. F. Fibrin and wound healing. *Ann. N. Y. Acad. Sci.* **936,** 355–367 (2001).
20. Clark, R. A. F. *The Molecular and Cellular Biology of Wound Repair*. (Springer US, 1996). doi:10.1007/978-1-4899-0185-9
21. Di Cera, E. Thrombin. *Mol. Aspects Med.* **29,** 203–254 (2008).
22. Brown, A. C. & Barker, T. H. Fibrin-based biomaterials: Modulation of macroscopic properties through rational design at the molecular level. *Acta Biomater.* **10,** 1502–1514 (2014).
23. Mosesson, M. W. Fibrinogen and fibrin structure and functions. *J. Thromb. Haemost.* **3,** 1894–1904 (2005).

24. Undas, A. & Ariëns, R. A. S. Fibrin clot structure and function: A role in the pathophysiology of arterial and venous thromboembolic diseases. *Arterioscler. Thromb. Vasc. Biol.* **31,** (2011).
25. Ryan, E. a., Mockros, L. F., Weisel, J. W. & Lorand, L. Structural Origins of Fibrin Clot Rheology. *Biophys. J.* **77,** 2813–2826 (1999).
26. Nakatsu, M. N., Davis, J. & Hughes, C. C. W. Optimized fibrin gel bead assay for the study of angiogenesis. *J. Vis. Exp.* 186 (2007). doi:10.3791/186
27. Kolehmainen, K. & Willerth, S. M. Preparation of 3D fibrin scaffolds for stem cell culture applications. *J. Vis. Exp.* e3641 (2012). doi:10.3791/3641
28. Arulmoli, J. *et al.* Static stretch affects neural stem cell differentiation in an extracellular matrix-dependent manner. *Sci. Rep.* **5,** 8499 (2015).
29. Colvin, R. B. & Dvorak, H. F. Fibrinogen/fibrin on the surface of macrophages: detection, distribution, binding requirements, and possible role in macrophage adherence phenomena. *J. Exp. Med.* **142,** 1377–1390 (1975).
30. Liu, J. *et al.* Soft fibrin gels promote selection and growth of tumorigenic cells. *Nat. Mater.* **11,** 734–41 (2012).
31. Moloney, T. C., Ní Fhlathartaigh, M., Kulkarni, M., Pandit, A. & Dowd, E. Fibrin As a Scaffold for Delivery of GDNF Overexpressing Stem Cells to the Adult Rat Brain. *ACS Biomater. Sci. Eng.* **1,** 559–566 (2015).
32. Singer, A. & Clark, R. Cutaneous wound healing. *N. Engl. J. Med.* **341,** 738–746 (1999).
33. Collen, D. & Lijnen, H. R. Basic and clinical aspects of fibrinolysis and thrombolysis. *Blood* **78,** 3114–3124 (1991).
34. Raum, D. *et al.* Synthesis of human plasminogen by the liver. *Science* **208,** 1036–1037 (1980).
35. Vande Berg, J. S. *et al.* Cultured pressure ulcer fibroblasts show replicative senescence with elevated production of plasmin, plasminogen activator inhibitor-1, and transforming growth factor-??1. *Wound Repair Regen.* **13,** 76–83 (2005).
36. Di Lullo, G. A., Sweeney, S. M., Körkkö, J., Ala-Kokko, L. & San Antonio, J. D. Mapping the ligand-binding sites and disease-associated mutations on the most abundant protein in the human, type I collagen. *J. Biol. Chem.* **277,** 4223–4231 (2002).
37. Brinckmann, J. Collagens at a glance. *Top. Curr. Chem.* **247,** 1–6 (2005).
38. Mouw, J. K., Ou, G. & Weaver, V. M. Extracellular matrix assembly: a multiscale deconstruction. *Nat. Rev. Mol. Cell Biol.* **15,** 771–785 (2014).
39. Kadler, K. E., Holmes, D. F., Trotter, J. A. & Chapman, J. A. Collagen fibril formation. *J. Biochem.* **316,** 1–11 (1996).
40. Sabeh, F., Shimizu-Hirota, R. & Weiss, S. J. Protease-dependent versus-independent cancer cell invasion programs: Three-dimensional amoeboid movement revisited. *J. Cell Biol.* **185,** 11–19 (2009).
41. Aragona, M. *et al.* A mechanical checkpoint controls multicellular growth through YAP/TAZ regulation by actin-processing factors. *Cell* **154,** 1047–1059 (2013).
42. Higuchi, A., Ling, Q.-D., Hsu, S.-T. & Umezawa, A. Biomimetic Cell Culture Proteins as Extracellular Matrices for Stem Cell Differentiation. *Chem. Rev.* **112,** 4507–4540 (2012).
43. Tibbitt, M. W. & Anseth, K. S. Hydrogels as extracellular matrix mimics for 3D cell culture. *Biotechnol. Bioeng.* **103,** 655–663 (2009).
44. Kotlarchyk, M. A. *et al.* Concentration independent modulation of local micromechanics in a fibrin gel. *PLoS One* **6,** (2011).
45. Gjorevski, N. & Nelson, C. M. Mapping of mechanical strains and stresses around quiescent engineered three-dimensional epithelial tissues. *Biophys. J.* **103,** 152–162 (2012).
46. Wang, N., Butler, J. P., Ingber, D. E. & Donald, E. Mechanotransduction across the cell surface and through the cytoskeleton. *Sci. Reports* **260,** 1124–1127 (1993).
47. Gasparski, A. N. & Beningo, K. A. Mechanoreception at the cell membrane: More than the integrins. *Arch. Biochem. Biophys.* **586,** 20–26 (2015).
48. Jansen, K. A. *et al.* A guide to mechanobiology: Where biology and physics meet. *Biochim. Biophys. Acta - Mol. Cell Res.* **1853,** 3043–3052 (2015).
49. Pek, Y. S., Wan, A. C. A. & Ying, J. Y. The effect of matrix stiffness on mesenchymal stem cell differentiation in a 3D thixotropic gel. *Biomaterials* **31,** 385–391 (2010).
50. Khetan, S. & Burdick, J. A. Patterning network structure to spatially control cellular remodeling and stem cell fate within 3-dimensional hydrogels. *Biomaterials* **31,** 8228–8234 (2010).

51. Steward, A. J. & Kelly, D. J. Mechanical regulation of mesenchymal stem cell differentiation. *J. Anat.* **227,** 717–731 (2015).
52. Tsou, Y.-H., Khoneisser, J., Huang, P.-C. & Xu, X. Hydrogel as a bioactive material to regulate stem cell fate. *Bioact. Mater.* (2016). doi:http://dx.doi.org/10.1016/j.bioactmat.2016.05.001
53. Watt, F. M. & Huck, W. T. S. Role of the extracellular matrix in regulating stem cell fate. *Nat. Rev. Mol. Cell Biol.* **14,** 467–73 (2013).
54. Wen, J. H. *et al.* Interplay of matrix stiffness and protein tethering in stem cell differentiation. *Nat. Mater.* **advance on,** 1–21 (2014).
55. Yang, C., Tibbitt, M. W., Basta, L. & Anseth, K. S. Mechanical memory and dosing influence stem cell fate. *Nat. Mater.* **13,** 645–652 (2014).
56. Hsieh, W. T. *et al.* Matrix dimensionality and stiffness cooperatively regulate osteogenesis of mesenchymal stromal cells. *Acta Biomater.* **32,** 210–222 (2016).
57. Chaudhuri, O. *et al.* Hydrogels with tunable stress relaxation regulate stem cell fate and activity. *Nat. Mater.* **15,** 326–333 (2015).
58. Tang, Y. *et al.* MT1-MMP-Dependent Control of Skeletal Stem Cell Commitment via a β1-Integrin/YAP/TAZ Signaling Axis. *Dev. Cell* **25,** 402–416 (2013).
59. Makanya, A. N., Hlushchuk, R. & Djonov, V. G. Intussusceptive angiogenesis and its role in vascular morphogenesis, patterning, and remodeling. *Angiogenesis* **12,** 113–123 (2009).
60. Ferrara, N., Gerber, H. P. & LeCouter, J. The biology of VEGF and its receptors. *Nat Med* **9,** 669–676 (2003).
61. Hillen, F. & Griffioen, A. W. Tumour vascularization: Sprouting angiogenesis and beyond. *Cancer Metastasis Rev.* **26,** 489–502 (2007).
62. Ribatti, D., Nico, B. & Crivellato, E. The role of pericytes in angiogenesis. *Int. J. Dev. Biol.* **55,** 261–268 (2011).
63. Cheng, G. *et al.* Engineered blood vessel networks connect to host vasculature via wrapping-and-tapping anastomosis. *Blood* **118,** 4740–4749 (2011).
64. Hellström, M. *et al.* Dll4 signalling through Notch1 regulates formation of tip cells during angiogenesis. *Nature* **445,** 776–780 (2007).
65. Gerhardt, H. *et al.* VEGF guides angiogenic sprouting utilizing endothelial tip cell filopodia. *J. Cell Biol.* **161,** 1163–1177 (2003).
66. Benedito, R. *et al.* The Notch Ligands Dll4 and Jagged1 Have Opposing Effects on Angiogenesis. *Cell* **137,** 1124–1135 (2009).
67. Jakobsson, L. *et al.* Endothelial cells dynamically compete for the tip cell position during angiogenic sprouting. *Nat. Cell Biol.* **12,** 943–953 (2010).
68. Gerhardt, H. VEGF and endothelial guidance in angiogenic sprouting. *Organogenesis* **4,** 241–246 (2008).
69. Reinhart-King, C. *Mechanical and Chemical Signaling in Angiogenesis*. **12,** (Springer Berlin Heidelberg, 2013).
70. Sieminski, A. L., Hebbel, R. P. & Gooch, K. J. The relative magnitudes of endothelial force generation and matrix stiffness modulate capillary morphogenesis in vitro. *Exp. Cell Res.* **297,** 574–584 (2004).
71. Shen, Y. *et al.* Hyaluronic acid hydrogel stiffness and oxygen tension affect cancer cell fate and endothelial sprouting. *Biomater. Sci.* **2,** 655–665 (2014).
72. Mason, B. N., Starchenko, A., Williams, R. M., Bonassar, L. J. & Reinhart-King, C. A. Tuning three-dimensional collagen matrix stiffness independently of collagen concentration modulates endothelial cell behavior. *Acta Biomater.* **9,** 4635–4644 (2013).
73. Ingber, D. E. & Folkman, J. How does extracellular matrix control capillary morphogenesis? *Cell* **58,** 803–805 (1989).
74. Ingber, D. E. Mechanical signaling and the cellular response to extracellular matrix in angiogenesis and cardiovascular physiology. *Circ. Res.* **91,** 877–887 (2002).
75. Shamloo, A. & Heilshorn, S. C. Matrix density mediates polarization and lumen formation of endothelial sprouts in VEGF gradients. *Lab Chip* **10,** 3061–3068 (2010).
76. Kniazeva, E. *et al.* Quantification of local matrix deformations and mechanical properties during capillary morphogenesis in 3D. *Integr. Biol.* **4,** 431–439 (2012).
77. Squires, T. M. & Mason, T. G. Fluid Mechanics of Microrheology. *Annu. Rev. Fluid Mech.* **42,** 413–438 (2010).
78. Wirtz, D. Particle-tracking microrheology of living cells: principles and applications. *Annu. Rev. Biophys.*

38, 301–26 (2009).
79. Velegol, D. & Lanni, F. Cell traction forces on soft biomaterials. I. Microrheology of type I collagen gels. *Biophys. J.* **81,** 1786 (2001).
80. Schultz, K. M., Kyburz, K. a & Anseth, K. S. Measuring dynamic cell-material interactions and remodeling during 3D human mesenchymal stem cell migration in hydrogels. *Proc. Natl. Acad. Sci. U. S. A.* **112,** E3757-3764 (2015).
81. Mizuno, D., Head, D. a., MacKintosh, F. C. & Schmidt, C. F. Active and Passive Microrheology in Equilibrium and Nonequilibrium Systems. *Macromolecules* **41,** 7194–7202 (2008).
82. Ashkin, A. Optical Trapping and Manipulation of Neutral Particles Using Lasers. *Opt. Photonics News* **10,** 41 (1999).
83. Neuman, K. C. & Block, S. M. Optical trapping. *Rev. Sci. Instrum.* **75,** 2787–2809 (2004).
84. Nieminen, T. A., Knöner, G., Heckenberg, N. R. & Rubinsztein-Dunlop, H. Physics of Optical Tweezers. in *Methods in Cell Biology* **82,** 207–236 (2007).
85. Ashkin, A. Forces of a single-beam gradient laser trap on a dielectric sphere in the ray optics regime. *Biophys. J.* **61,** 569–82 (1992).
86. Shaevitz, J. W. A Practical Guide to Optical Trapping. *Web* 1–19 (2006).
87. Brau, R. R. *et al.* Passive and active microrheology with optical tweezers. *J. Opt. A Pure Appl. Opt.* **9,** S103–S112 (2007).
88. Gittes, F. & Schmidt, C. F. Chapter 8 Signals and Noise in Micromechanical Measurements. *Methods Cell Biol.* **55,** 129–156 (1997).
89. Lu, P., Weaver, V. M. & Werb, Z. The extracellular matrix: A dynamic niche in cancer progression. *J. Cell Biol.* **196,** 395–406 (2012).
90. Vogel, V. & Sheetz, M. Local force and geometry sensing regulate cell functions. *Nat. Rev. Mol. Cell Biol.* **7,** 265–275 (2006).
91. Gerwins, P., Sköldenberg, E. & Claesson-Welsh, L. Function of fibroblast growth factors and vascular endothelial growth factors and their receptors in angiogenesis. *Crit. Rev. Oncol. Hematol.* **34,** 185–194 (2000).

CHAPTER 2: SPATIAL DISTRIBUTIONS OF PERICELLULAR STIFFNESS IN NATURAL EXTRACELLULAR MATRICES ARE DEPENDENT ON CELL-MEDIATED PROTEOLYSIS AND CONTRACTILITY

Mark Keating[a, 1], Abhishek Kurup[a, 1], Martha Alvarez-Elizondo[b], A.J. Levine[c], Elliot Botvinick[a, 2]

[a] University of California, Irvine, Department of Biomedical Engineering, Irvine, 92697-2730, USA
[b] Technion, Israel Institute of Technology, Department of Biomedical Engineering, Technion City, 32000, Israel
[c] Departments of Physics & Astronomy, Chemistry & Biochemistry, and Biomathematics, University of California, Los Angeles CA 90095 USA.
[1] These authors contributed equally to this work
[2] To whom correspondence may addressed. Email: elliot.botvinick@uci.edu

Keywords: Microrheology; Cellular Remodeling; Pericellular Stiffness; Tissue Mechanics; Extracellular Matrix; Hydrogel

2.1 ABSTRACT

Bulk tissue stiffness has been correlated with regulation of cellular processes and conversely cells have been shown to remodel their pericellular tissue according to a complex feedback mechanism critical to development, homeostasis, and disease. However, bulk rheological methods mask the dynamics within a heterogeneous fibrous extracellular matrix (ECM) in the region proximal to a cell (pericellular region). Here, we use optical tweezers active microrheology (AMR) to probe the distribution of the complex material response function ($\alpha = \alpha' + \alpha''$, in units of μm/nN) within a type I collagen ECM, a biomaterial commonly used in tissue engineering. We discovered cells both elastically and plastically deformed the pericellular material. α' is wildly heterogeneous, with $1/\alpha$' values spanning three orders of magnitude around a single cell. This was observed in gels having a cell-free 1/α' of approximately 0.5 nN/μm. We also found that inhibition of cell contractility instantaneously softens the pericellular space and reduces stiffness heterogeneity, suggesting the system was strain hardened and not only plastically remodeled. The remaining regions of high stiffness strongly suggest cellular remodeling of their surrounding matrix. To test this hypothesis, cells were incubated within the type I collagen gel for 24 hours in a media containing a broad-spectrum matrix metalloproteinase (MMP) inhibitor. While the pericellular material maintained stiffness asymmetry, stiffness magnitudes were reduced. Dual inhibition demonstrates that the combination of MMP activity and contractility is necessary to establish the pericellular stiffness landscape. This heterogeneity in stiffness suggests the distribution of pericellular stiffness, and not bulk stiffness alone, must be considered in the study of cell-ECM interactions and design of complex biomaterial scaffolds.

2.2 INTRODUCTION

Interactions between cells and their extracellular matrix (ECM) are bi-directional. On one hand, the mechanical properties of the ECM have been shown to regulate key processes in cells; for example, increasing bulk ECM stiffness has been correlated to invasion of mammary epithelial cells[1], differentiation of mesenchymal stem cells[2,3], and maturation of cardiomyocytes[4]. On the other hand, cells actively alter their ECM through context-dependent degradation, remodeling, and deposition of new ECM[5]. Thus, quantifying the mechanical interactions between the cell and its ECM both spatially and temporally, at a scale relevant to the interaction, is imperative to study how cells are regulated in physiological and pathological processes.

One interesting aspect of cell-ECM physical interactions is the distribution of traction forces that cells exert onto their local ECM. 3D traction force microscopy (TFM) has been developed for cells fully embedded within a linear, homogenous, nano-porous, synthetic PEG hydrogel containing tracer microbeads[6,7], which can be modified to contain sites for cell adhesion and cell mediated degradation[8]. The strain field can be calculated by tracking bead displacement. Then, an estimation of traction forces can be computed under the assumption of hydrogel linear elasticity, homogeneity, and without consideration of cell-mediated degradation and deposition of new ECM. While these methods are elegant and provide important insight, results may not be generalizable to physiologically relevant tissues because these gels do not share the native architecture, pore size, or nonlinear properties of natural matrices[9]. Such differences have the potential to cause cells to remodel these ECMs differently, if at all, than they would in natural materials. Heterogeneities in local ECM architecture and stiffness have hindered efforts to extend TFM to natural matrices particularly in the pericellular space. For example, it has been reported that stresses within the ECM cannot be determined from bead

displacements alone under the assumption of homogenous mechanical properties[7] and without accounting for local degradation[10]. Furthermore, stiffness of natural, type I collagen fibrous matrices increases non-linearly with deformation, and cannot be determined from collagen concentration alone[7,11]. Instantaneous stiffness should be determinable from strain if the nonlinear relationship between strain and stiffness is known a priori. However, such a calculation requires knowledge of the current stress free state of the material, which may not be available once cells plastically remodel the local matrix. Thus, the study of how pericellular stiffness changes over time requires the use of a technique that can directly measure stiffness locally.

Here we use optical tweezers active microrheology (AMR) to directly measure the complex material response function at multiple sites around cells grown in 3D type 1 collagen gels and observe the dependence of material property heterogeneity on both cell contractility and matrix metalloproteinase (MMP) activity. One potential way a cell can modulate its pericellular mechanical topography is through cytoskeletal contractile forces that locally deform the ECM and stiffen it through strain-hardening[12], a process that's also essential for cell mechanoresponsiveness[13]. Another way in which a cell may modulate its local mechanical topography is through degradation of its local ECM, mediated by cell synthesized MMPs[14]. MMP mediated matrix degradation has been shown to be critical in processes including angiogenesis[15,16], cancer metastasis [17], or skeletal formation[18]. Thus, both cytoskeletal contractility and MMP activity are logical targets to explore the role of a cell in establishing or maintaining its pericellular stiffness, which we have shown can be significantly stiffer than values reported by bulk rheology [19–21] and are consistent in order-of-magnitude to stiffness reported by other groups using AMR in type I collagen[22], Matrigel, hyaluronic acid, and zebrafish *in vivo*[23]. In earlier studies, we used AMR to discover that during capillary

morphogenesis, the pericellular space surrounding the tip of a sprouting capillary had increased stiffness as compared to distal regions[24]. We also showed that mouse skeletal stem cells required MMP14 (MT1-MMP) activity to stiffen the pericellular space within 3D collagen gels, a result that was associated with osteogenic fate commitment *in vivo*[25]. Here we use AMR to measure the distribution of pericellular stiffness surrounding isolated dermal fibroblasts as well as smooth muscle cells embedded within collagen gels and observe important new insights into how cells modulate their mechanical microenvironment in a contractility and MMP-dependent manner.

2.3 METHODS

2.3.1 Cell Culture

Dermal fibroblasts (DFs) were acquired from Lonza (CC-2511) and were cultured in DMEM (Fisher) with 10% FBS (Gibco) and 1% penicillin streptomycin (Gibco). Human Aortic smooth muscle cells (HAoSMCs) were acquired from ATCC (PCS-100-012) and the media plus bullet kit (CC-3182) from Lonza. All cells in this study were used prior to passage 7.

2.3.2 Collagen Hydrogel Formation

Type 1 collagen was chosen for these studies given both its abundance as the one of the main structural protein of ECM within the body[26] and it's relative prevalence within the natural context of each type cell used [27,28]. Collagen hydrogels were made at a final concentration of 1.0 mg/mL or 2.0 mg/mL using acid extracted rat tail type 1 collagen from vendors Advanced Biomatrix or Corning, respectively. Collagen of this type has been previously reported to vary significantly from lot to lot as has been previously noted by others[29]. Importantly, collagen lots and concentrations were kept consistent for each set of cells: 1mg/mL for DF experiments and 2 mg/mL for HAoSMC experiments. Structure (as assessed by reflection confocal) and mechanical

properties (as probed by AMR) were roughly matched between the two cell-free conditions. For DF experiments, 3 cells in 3 separate gels were measured per condition. For HAoSMC experiments, 3 cells were measured within a single gel per condition.

Collagen gels were prepared with 10x PBS (Life Technologies), 1N NaOH (Fisher), sterile-filtered DI H_2O, 2 μm carboxylated silica microbeads (0.8 mg/ml, Bangs Laboratories), and cells (100 k/ml) in 35 mm glass bottom dishes (MatTek). The samples were placed in a standard tissue culture incubator at 37 °C for 40 minutes during the polymerization process, after which media was added to each dish.

Cells in control conditions were fed with normal media at the time of gelation. In the BB94 conditions, cells were fed with normal media supplemented with 10 μM BB94 (Sigma) after gelation. All dishes were incubated for 24 hours in a standard tissue culture incubator. Prior to AMR measurements, the culture media was supplemented with HEPES (20 mM) and the dish placed within stage. A custom-built incubation system plus an objective heater maintained temperature in the dish at 34°C. Gels were allowed to equilibrate to temperature for at least 1 hour to prevent focus drift[30]. Y27632 conditions were supplemented with 20 μM Y27632 (Sigma) during this 1 hour, on stage incubation period.

2.3.3 AMR system

The AMR system is illustrated in **Supp. Figure 2.1a**. Optical tweezers are generated by a continuous-wave fiber laser with emission at 1064 nm (IPG Photonics), hereafter referred to as the trapping beam. A pair of galvanometer mirrors (ThorLabs) placed conjugate to the back focal plane of the objective lens steers the trapping beam focus in the transverse plane of the microscope objective. The cover glass reflects a small fraction of the beam power and directs it

onto a quadrant photo diode (QPD, Newport) labeled as trapQPD in **Supp. Figure 2.1a**. The trapQPD outputs analog signals proportional to the deflection of the trapping beam. A low power laser diode with emission at 785 nm (World Star Technologies), hereafter referred to as the detection beam, detects the probe bead response motion. A long pass dichroic beam splitting mirror (D1, Semrock) combines the two laser beams and introduces them into the white light path of an IX81 inverted microscope (Olympus).

The microscope is equipped with the Zero Drift Compensation package (Olympus) comprising an external laser/detector unit and a filter cube placed just below the microscope objective lens (D2 in **Supp**. **Figure 2.1a**). We removed the laser/detector unit and replaced the stock dichroic beam splitting mirror with a short pass dichroic beam splitting mirror (Chroma) designed to reflect our laser beams into the microscope objective lens while passing visible light for confocal and brightfield microscopy. A high numerical aperture microscope objective lens (60x-oil PlanApo TIRFM 1.45 NA, Olympus) focuses both beams into the sample. The microscope condenser lens (0.55 NA, Olympus) collects the forward scattered laser light which is then reflected by a 50/50 beam splitter (Thorlabs), labeled D3 in **Supp. Figure 2.1a**, towards the detection beam quadrant photo diode (detQPD, Newport).

A short pass dichroic beam splitting mirror D4 (Chroma Technologies) is placed before the detQPD to reflect the trapping beam away from the detQPD. A band pass filter centered at 785 nm is placed directly in front of the detQPD to remove noise from non-detection laser sources. A laser trapped microbead oscillating in the hydrogel will deflect the detection beam across the surface of the detQPD, which outputs analog signals proportional to the position of that microbead.

The microscope is also equipped with a FluoView 1200 laser confocal scan head (Olympus) used here for reflection confocal microscopy (488 nm laser line). Samples are placed onto a piezoelectric XY stage (P-733.2CL, Physik Instrumente) which is housed within a motorized XY stepper motor stage (MS-2000, Applied Scientific Instruments), allowing for sub-nanometer resolution movements over an area of (100 x 100) μm^2.

Our microscope and optical tweezer components comprise a robotic system controlled by custom software developed in our laboratory (**Supplementary Note 2**). Net time to probe each bead is approximately 8 seconds. Each bead is probed at 50Hz. In support of probing at 50 Hz alone, previous microrheological studies have reported that *probed stiffness* is frequency independent in type I collagen gels at frequencies <100 Hz[31] and we further determined no difference in *1/* α' measured by frequency sweep or at 50 Hz alone (**Supp. Figure 2.2a**). Accurate measurement of *1/* α' requires precise centering of each bead in the laser trap. We found errors in measured *1/* α' due to automated stage motion were 5.5% (**Supplementary Note 2**).

2.3.4 System Validation

To validate our automated system, we first conduct AMR in water at room temperature with a frequency sweep at [10 20 50 75 100] Hz. Viscosity, η, in water is empirically known to be 0.001 Pa s and can be determined by AMR using the relationship $\eta = G''/2\pi f$, where f is the frequency of oscillation[32]. Before each experiment, we validated the AMR system by measuring η of water and comparing it to the theoretical value. A typical measured value is 0.001 ± 5.76 x 10^{-5} Pa s, which agrees with the empirical value ($n_{beads} = 5$; $p = 0.975$).

We next probed beads in a hydrogel (type I collagen) to investigate potential sources of error originating from hardware automation. We randomly selected beads (n = 5) separated from

each other by at least 75 μm. At this distance, the robotic system must move both the long-range stepper motor stage as well as the piezoelectric stage to center a bead within the optical trap with 0.10 μm repeatability. The AMR system (**Supplementary Note 2**) cycled between all beads five times (**Supp. Figure 2.2b**), each time measuring *1/ α'*. On average, the percent error (standard deviation/ mean x 100%) of *1/α'* for the same bead across all five measurements was 5.5%, demonstrating the small error introduced by automation. To assess the effect of rigid objects contained within a type I collagen gel on stiffness as probed by AMR, carboxylated 20 μm polystyrene beads (Polysciences) were embedded into a 1mg/mL type 1 collagen gel and AMR measurements were conducted proximal to the bead (**Supp. Figure 2.4**). No significant difference was found between measurements proximal to the bead (N=3) and comparable measurements within a similar set of cell free gels (N=3, p=0.26).

2.3.5 Statistical Analyses

All statistical analyses were conducted in OriginPro using the Mann-Whitney test, unless otherwise stated, because typically data was not normally distributed (Shapiro-Wilk test, $p < 0.05$). The (statistical) alpha value used to determine statistical significance was adjusted in the cases of multiple comparisons according to the Bonferroni correction. For the case of viscosity measurement in water, comparison was made by the Student's T-test. Data in the manuscript is presented as mean ± standard deviation.

2.4 RESULTS

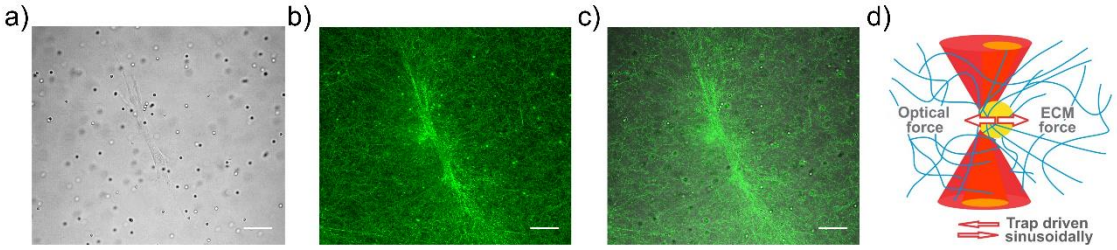

Figure 2.1*: Probing pericellular stiffness with AMR. (**a**) Brightfield image of an isolated DF cultured in a type I collagen gel embedded with 2 µm diameter silica microbeads. (**b**) Reflection confocal microscopy image of the region in (**a**) showing both the cell and the fibrous collagen matrix. (**c**) Merged brightfield and confocal images. Scale bars are 20 µm. (**d**) Diagram of optical tweezers active microrheology (AMR). The optical tweezers microbeam (dark red) is spatially oscillated to exert oscillatory forces on a microbead (yellow) and forces are resisted by the complex material response of the local extracellular matrix (blue). Detection beam deflections (light red) are analyzed to compute the complex valued material response α.*

2.4.1 Active microrheology to measure pericellular stiffness

We use AMR to measure the complex valued material properties within natural ECMs[19,22]. In our method, cells are embedded within an ECM that also contains a dispersion of 2 µm diameter silica microbeads. The cells and ECM can be imaged by transillumination (brightfield) microscopy (**Figure 2.1a**) and reflection confocal microscopy, which provides label-free images of cell and ECM architecture (**Figure 2.1b-c**). Examination of co-aligned transmission and reflection confocal microscope images confirms that most beads are confined within a pore (**Supp. Figure 2.5**). Qualitatively, we do not observe free diffusion of beads throughout the gel, even proximal to cells (**Supp. Videos 1-4**). In AMR, optical tweezers forces oscillate a microbead confined within the gel and a detection laser detects the change in bead position (**Figure 2.1d**).

The real (*α'*) and imaginary (*α''*) components of the complex valued material response function α are computed from experimental data **(see Supplementary Note 1)** with no simplifying assumptions regarding thermodynamic equilibrium and, $X(\omega) = \alpha(\omega)F(\omega)$,where $X(\omega)$ and

$F(\omega)$ are the amplitudes of the bead's displacement and the applied optical force respectively at ω, the frequency of the sinusoidal force applied by the optical tweezers. Here α' measures to the local material's elastic response, whereas α'' reports on the dissipative forces acting on the microbead. An alternative method to AMR is particle tracking microrheology, a passive method in which the thermally driven motion of beads is recorded at video rate, or less commonly at kilohertz by a detection beam [33], and used to compute ECM material properties.

If the system were in thermal equilibrium one could rely on the fluctuation-dissipation theorem[34] to relate the observed fluctuation spectrum to the frequency-dependent imaginary part of the response function α(ω). From these data, one can also recover the real part of the response function using Kramer-Kronig relations and generally applicable assumptions regarding the unobserved, high frequency part of the dissipative response function. This method, however, is inapplicable to nonequilibrium systems since the fluctuation-dissipation theorem fails. In some cases this failure is dramatic[35]. Therefore, passive microrheology for characterizing the pericellular space has been limited to either detection of the formation of a hydrogel, dissolution of a hydrogel[36], or ECMs that are orders of magnitude softer than *in vivo* ECMs[37,38].

Typically in nonequilibrium systems, one must resort to active microrheology, although in some cases the combination of active and passive techniques has been used to quantify the nonequilibrium nature of various biological systems[39]. We note also that non-driven displacement fluctuations in the system are significantly smaller than the observed response to the driven displacement of our reference particles, on which we base our active microrheological studies. In this work, we report solely on active microrheological measurements, which are sufficient to extract mechanical or rheological data on an ECM network containing live cells that is clearly out of equilibrium.

2.4.2 AMR Around Living Cells Reveals Stiffness Heterogeneity

Human Aortic Smooth Muscle Cells (HAoSMCs) were cultured in type I collagen gels (2 mg/ml) containing 2 μm diameter microbeads at a concentration of 0.8 mg/ml. On average, each bead was located approximately 13 μm from its neighbors. Probe microbeads were found approximately 30 μm above the glass coverslip in a 350 x 280 μm^2 region, and were probed before and after contractility inhibition via 20 μM ROCK inhibitor Y27632. This has previously shown to result in a significant loss in contractility (within 15-30 minutes) for human uterine smooth muscle cells[40]. **Figure 2.2a** shows a significant decrease in the mean value of $1/\alpha'$ from 3.1 ± 3.0 nN/μm to 1.2 ± 1.0 nN/μm before and after treatment respectively ($p < 0.001$). Mapping stiffness spatially before treatment shows the material surrounding two cells was significantly stiffened (*red box*; $n_{beads} = 42$) as compared to cell-free regions (*blue box*; $n_{beads} = 30$) within the image montage ($p < 0.001$). Inhibiting contractility (**Figure 2.2b**) results in a notable loss in spatial heterogeneity in $1/\alpha'$ (**Figure 2.2c**). Note the handful of beads between cells 2 and 3 that reported stiff ECM before treatment (**Figure 2.2d**), but did not soften as much compared to their neighbors after Y27632 treatment (**Figure 2.2e**). We used reflection confocal microscopy to image this region and observed fiber alignment and increased ECM density pre-treatment (**Figure 2.2f**). Confocal imaging after treatment (**Figure 2.2g**) shows that the decrease in average ECM stiffness correlated with relaxation, but not abatement, of fiber alignment (**Figure 2.2g**). In fact, the ECM density between the two cells remained high after treatment. This suggests roles for cell-mediated local remodeling and provides evidence that collagen

concentration alone may not determine stiffness.

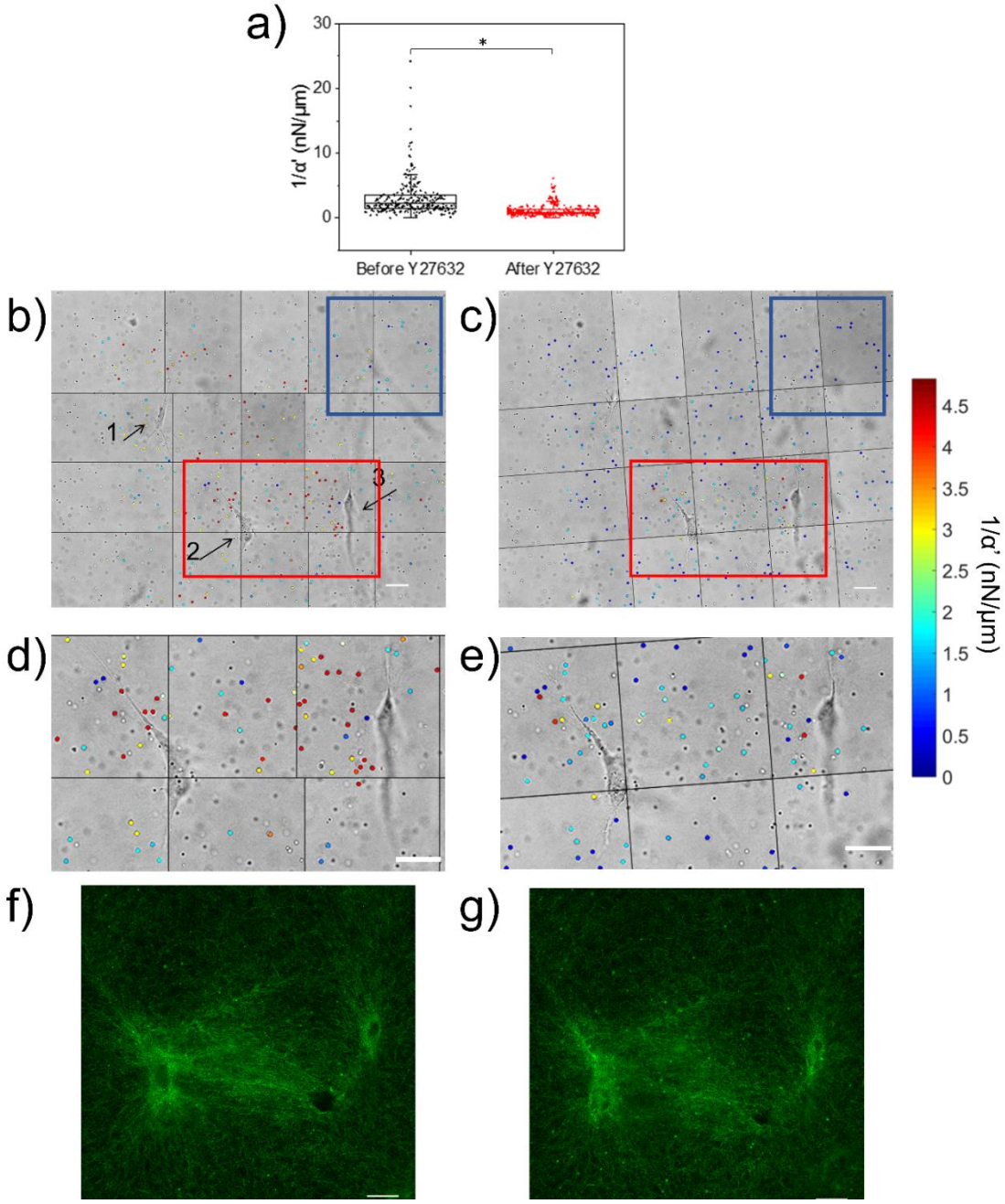

***Figure 2.2**: Mapping pericellular stiffness with AMR. (**a**) Scatterplot of AMR measurements of 1/α' in 2 mg/ml type I collagen gel around multiple HAoSMCs in a ~ 350 x 280 μm^2 region taken before (n_{beads} = 288) and after (n_{beads} = 279) 1 hour incubation with 20 μM Y27632. 1/α' values significantly decreased after treatment ($p << 0.001$). Montage containing HAoSMCs (labeled 1, 2, and 3) and microbeads (represented in (**a**)) probed before (**b**) and after (**c**) treatment. Probed microbeads are overlaid with a colored circle corresponding to the measured 1/α' (note color bar saturates at 5 nN/μm, but full range is shown in (**a**). (**d, e**) Zoomed in view of regions in (**b**) and (**c**) bound by red rectangle. (**f, g**) Reflection confocal images of region between cells 2 and 3 before and after treatment with Y27632. Scale bars are 20 μm.*

2.4.3 Average pericellular stiffness depends on cytoskeletal contractility and MMP activity

We next studied the effects of both cytoskeletal contractility and local remodeling on pericellular material stiffness around isolated HAoSMCs as well as human dermal fibroblasts (DFs). AMR was conducted around isolated cells in control conditions as well as those treated with Y27632 and BB94 (Batimastat), a wide-spectrum inhibitor of matrix metalloproteinases (MMPs). The pericellular stiffness surrounding isolated cells was measured in four conditions: (*1)* control, (*2)* Y27632, (*3)* BB94 or (*4)* both BB94 and Y27632. For conditions *3* and *4*, 10 μM BB94 was added just after gelation and followed by 24h incubation. For conditions *2* and *4*, 20μM Y27632 was added after overnight incubation at one hour prior to measurements. As compared to control, average $1/\alpha'$ in the probed region decreased in all three experimental conditions for both cell types (DF: $p < 0.001$, **Figure 2.3a;** HAoSMC: $p < 0.001$, **Supp. Figure 2.6**). Additionally, average $1/\alpha'$ for condition *4* was lower than that for conditions *2* and *3* (DF: $p < 0.001$, HAoSMC: $p < 0.001$), showing that dual-inhibition was most effective at softening the pericellular ECM relative to control. To determine any effects of the drugs on the hydrogel, AMR was conducted in cell-free gels (1mg/mL type 1 collagen). No significant changes in $1/\alpha'$ were detected between gels treated with 20 μM Y27632 for one hour, gels treated with 10 μM

BB94 for 24-hours, gels treated with Y27632 after a 24-hour treatment with BB94, and control gels (**Fig. 3b,** Kruskal–Wallis test, p=0.16).

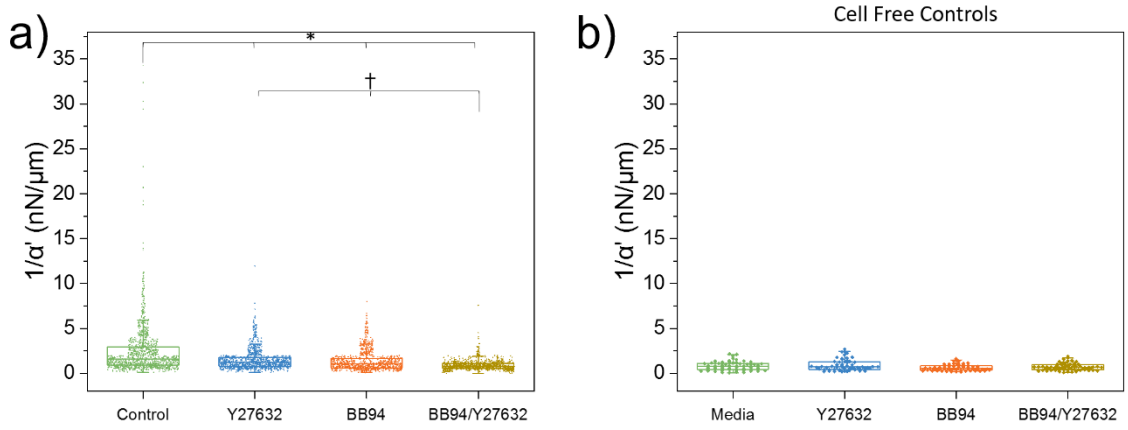

Figure 2.3*: Pericellular stiffness distribution modulated by inhibition of contractility and MMP activity.* ***(a)*** *AMR measurements of 1/α' in cell-free 1 mg/ml type I collagen gels under control conditions (n_{beads} = 59), as well as treatment conditions: 20 μM Y27632 (n_{beads} = 58), 10 μM BB94 (n_{beads} =58), and BB94+Y27632 (n_{beads} = 71). No significant differences were detected (Kruskal–Wallis test, p=0.16).* ***(b)*** *AMR measurements of 1/α' in a ~280 x 280 x 30 μm³ volume surrounding isolated DFs in control conditions (n_{cells} = 3; n_{beads} = 1060) as well as treatment with Y27632 (n_{cells} = 3; n_{beads} = 994), BB94 (n_{cells} = 3; n_{beads} = 873) and BB94+Y27632 (n_{cells} = 3; n_{beads} = 804). Each experimental condition was significantly different as compared to control (*, p << 0.001). Additionally, BB94+Y27632 was different as compared to Y27632 and BB94 (†, p << 0.001).*

2.4.4 Spatial distribution of pericellular stiffness depends on MMP activity and cytoskeletal contractility

In order to aggregate pericellular stiffness distributions across multiple cells we first transformed the Cartesian coordinates of each bead into a polar coordinate system (r, θ), with origin at the cell centroid. As shown in **Figure 2.4a-d**, all points were rotated such that the major axis of each cell (determined by a bounding ellipse) aligns with $\theta = 0$ allowing superposition of all points across all cells, per condition. The decrease in stiffness and loss in spatial heterogeneity following drug treatment as compared to control (**Figure 2.4a-d**) is better visualized by interpolated surface maps (**Figure 2.4e-h**). Here interpolation is for visualization purposes only and likely not reliable between measured coordinates. We next computed S_d, the shortest

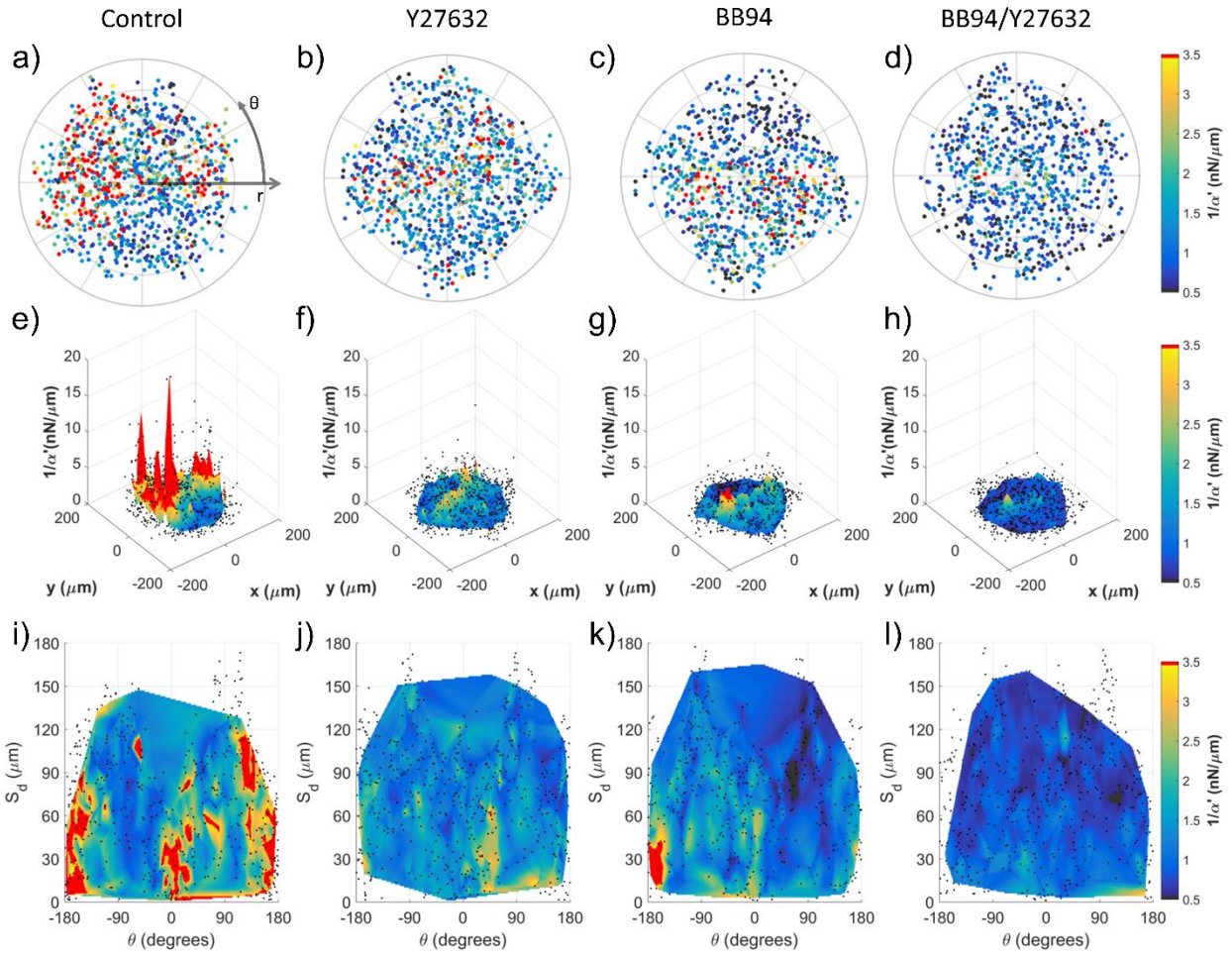

Figure 2.4*: Characterization of pericellular stiffness for multiple isolated DFs. Polar plots of 1/α' surrounding isolated cells for (**a**) control (n_{cells} = 3), (**b**) 20 μM Y27632 (n_{cells} = 3), (**c**) 10 μM BB94 (n_{cells} = 3) and (**d**) BB94+Y27632 (n_{cells} = 3) conditions. Concentric lines are drawn in 50 μm increments of r. (**e-h**) 3D surface plots of the aggregate data in (**a-d**), respectively. (**i-l**) Data in (**a-d**) mapped to a Cartesian plot of θ vs. distance from cell boundary, S_d. For (**e-l**), probed beads are denoted by black dots. Data interpolation is restricted to regions containing data from all cells, per condition. Color maps in (**a-d** and **i-l**) range approximately from the average 1/α' value of BB94+Y27632 to the average 1/α' value plus one standard deviation of the control condition. Note that the color map saturates at 3.5 nN/μm.*

distance between each probed microbead and the boundary of its corresponding cell. **Figure 2.4i-l** show *1/α'* plotted on a (S_d,*θ*) coordinate system to visualize relationships between ECM stiffening, cell orientation, and distances from cells across experimental conditions.

In the case of DFs, which have an elongated morphology (**Supp. Figure 2.7**), punctate regions of stiffening are observed near to the leading (-45° < *θ* < *+45*°) and trailing (135° < *θ* < *180*° and -180° < *θ* < *-135*°) edges for S_d < 50 μm (**Figure 2.4**). Discrete punctate regions of

elevated *1/α'* values were also found for $S_d > 50$ μm, supporting previous assertions that long range stiffening may not be a spatially continuous process, but dependent on the fibrous network[41] and/or the asymmetry[42] by which cells contract against their matrix. In support of this hypothesis, inhibition of cell contractility by Y27632 (**Figure 2.4b,f,j**) resulted in a significant decrease in pericellular stiffness and stiffness asymmetry as compared to control (**Figure 2.4a,e,i**). This observation implicates the important role of cytoskeletal contractility-mediated strain hardening in determining the mechanical landscape in the pericellular space.

We also found that inhibition of MMP activity by BB94 (**Figure 2.4c,g,k)** lowers *1/α'* values relative to control but preserves asymmetry (**Figure 2.4k**), as observed in control conditions, but without long range stiffening. Further incubation with Y27632 (**Figure 2.4d,h,l**) nearly completely abrogates stiffening in the pericellular space. Similar results were observed for HAoSMCs in 2 mg/mL type 1 collagen gels, which show a less elongated morphology (**Supp. Figure 2.8 and Supp. Figure 2.9**). For both cell types, either cellular contractility (**Figure 2.4b,f,j; Fig. S9b,f,j**) or MMP activity (**Figure 2.4c,g,k; Fig. S9c,g,k**) alone were insufficient to create or maintain the asymmetry, stiffness, and long range stiffening observed in controls (**Figure 2.4a,e,i**; **Fig. S9a,e,i)**. Rather, it may be the cooperation between both MMP activity and cellular contractility that are required for creating a normal pericellular mechanical topography in the complex material of our type 1 collagen system.

2.5 DISCUSSION

As we have previously demonstrated in cell-free systems, the distribution of local ECM stiffness values within a single gel are not observable via bulk rheological methods [19]. Consequently, studies relying on bulk measurements alone may miss important ways in which ECM heterogeneity can guide cell behavior with respect to stiffness. As a metric for heterogeneity, we

examined the differences in $1/\alpha'$ as probed by neighboring beads (e.g. **Figure 2.4**). This provides us with an estimate of errors when interpolating stiffness in regions not directly probed by a bead. For each bead, we determined *d*, the center-to-center distance to its closest neighbor (eliminating redundant pairs), and $\Delta(1/\alpha')$, the difference in $1/\alpha'$ reported by those beads (**Figure 2.5a)**. The lower limit of *d* is 2 μm, which occurs only if two beads are in contact. Histograms of $\Delta(1/\alpha')$ (**Figure 2.5b-f**) show the effects of cell contractility and MMP-mediated ECM degradation on $\Delta(1/\alpha')$ in the pericellular space. For control cells (**Figure 2.5c**), $\Delta(1/\alpha')$ values ranged up to 30 nN/μm and 75% of values were less than 2 nN/μm. In contrast, 75% of $\Delta(1/\alpha')$ values in a cell-free gel (**Figure 2.5b**) were less than 0.5 nN/μm. Additionally, 75% of $\Delta(1/\alpha')$ values were less than 1, 1 and 0.5 nN/μm, following inhibition of contractility (**Figure 2.5d**), MMPs (**Figure 2.5e**) or both (**Figure 2.5**) respectively. This finding demonstrates that in control conditions, $\Delta(1/\alpha')$ can vary wildly between adjacent probe beads around a single cell. We next parsed beads into two groups, those found within and those beyond 50 μm of the cell boundary. Two important findings were observed relating to the limits of interpolation. First, for control cells, there is no clear trend between $\Delta(1/\alpha')$ and the distance between beads in both groups (**Figure 2.5g)**. This observation suggests that minimizing bead-to-bead distance does not improve accuracy of interpolation. Second, regions of long-range stiffening for control cells (**Figure 2.4i)** also exhibit large $\Delta(1/\alpha')$ (**Figure 2.5g,** black markers) particularly as compared to inhibited cells (**Figure 2.5h-j**). Similar analysis was performed on HAoSMC, shown in **Figure S10**.

Taken together, these observations suggest that estimation of a continuous *stiffness* function derived from interpolation between beads in natural matrices like collagen can produce errors in local stiffness estimates as large as tens of nN/µm, or under the assumption of a continuum, hundreds of pascals.

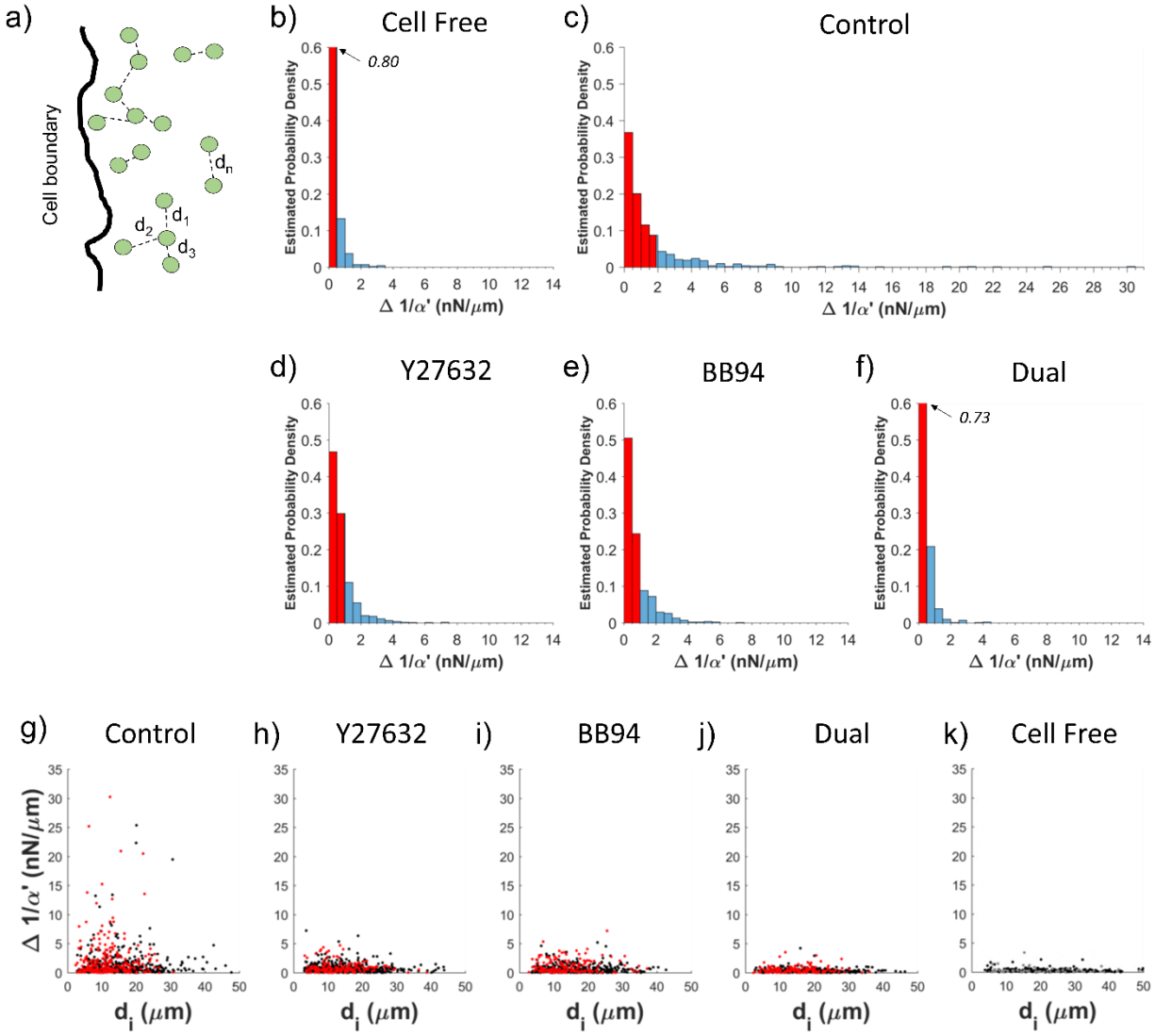

Figure 2.5*: Variability in stiffness between adjacent beads. (**a**) For each bead, d_i is defined as the distance to its closest neighbor. Estimated probability density of Δ1/α' in (**b**) cell free collagen as well as collagen gels containing DFs under (**c**) control conditions or treatment with (**d**) Y27632, (**e**) BB94 or (**f**) both. Red shaded region represents 75% of the data. (**g-h**) Scatter plots of d_i and Δ1/α' for DFs under (**g**) control conditions or treatment with (**h**) Y27632, (**i**) BB94 or (**j**) both. Red dots indicate beads within S_d < 50 µm and black dots indicate beads within S_d > 50 µm. (**k**) Scatter plots of d_i and Δ1/α' for a cell-free collagen gel.*

It is difficult to assess the consequences of such a wildly varying stiffness field on computing forces. In order to ascertain an order of magnitude understanding of errors in estimating force, we conducted a quantitative but rough estimate of such forces under assumptions of no strain hardening, viscoelastic creep, and stress relaxation. Specifically, we computed the force magnitude, *F*, required to displace a bead by distance *x*, where $F = |x/\alpha'|$. We estimated values of *F* under a simplifying assumption that α *does* not change for the 1 and 5 μm displacements used in this analysis. Although we have data to contradict this assumption (not shown), our analysis will still provide insight into the significance of observed $\Delta(1/\alpha')$ values in an order of magnitude sense. As shown in **Table 2.1**, we estimated force magnitudes acting on a bead for values of $1/\alpha' \in$ [0.1, 0.5, 1, 5, 10, 30] nN/μm, a range observed surrounding control

$\mathbf{1/\alpha'}$ **[nN/**$\boldsymbol{\mu m}$**]**	$\boldsymbol{F}$ $[\boldsymbol{nN}]$	
	$\boldsymbol{\Delta x = 1\ \mu m}$	$\boldsymbol{\Delta x = 5\ \mu m}$
0.1	0.1	0.5
0.5	0.5	2.5
1	1	5
5	5	25
10	10	50
30	30	150

Table 2.1: Estimates of force magnitude required to displace a bead by 1 or 5 μm in a gel with given 1/ α'.

cells (**Figure 2.3a**). *F* was estimated for *x* = 1 μm and 5 μm, which are values consistent with previously reported bead displacements surrounding single HT-1080 fibrosarcoma cells in a type I collagen gel[10]. By our estimate, *F* could range from 0.5 to 150 nN for a 5 μm displacement

around an untreated cell (**Table 2.1**). Thus, if α is not directly measured, but estimated from other methods including parallel plate rheology, the error in *F* could be as large as two orders of magnitude. This estimated range of *F* spans the traction forces measured for a single cell using two-dimensional (2D) micropillar traction force microscopy[43,44]. Jin et al. computed cell contractile forces in 3D ECMs by monitoring the contraction of a type I collagen gel seeded with human aortic adventitial fibroblasts. They estimated the average cell contractile force was approximately 1.5 nN, which is

well within our range of estimated forces[45]. Bloom et al. tracked displacements of 3.6 μm diameter beads around HT-1080 cells in a type I collagen gel. They estimated that a 4 nN force is required to displace a bead by 5 μm[10]. Both of these studies assumed homogenous material properties measured by bulk methods. But, as seen in our experiments, because *1/α'* can range across three orders of magnitude around each bead, force calculations are very sensitive to this uncertainly in *1/α'*. Given this new insight, we caution the use of bead-based TFM in fibrous gels unless stiffness is determined continuously throughout the pericellular space.

Quantification of the effects of cell contractility, remodeling, and fiber mesh architecture on the pericellular stiffness within a natural 3D ECM at physiological concentration has only been modeled[46] within the volume of a fibrous hydrogel, but not directly measured within the volume as is possible with AMR. Even within synthetic ECM constructs, specifically those with sites susceptible to cell-mediated degradation, pericellular mechanical properties are unknown unless measured directly, as has been recently noted[47]. Our method is generalizable to many tissue engineering systems because it is independent of ECM composition and cell type[19–21,24,48–50]. AMR is ultimately limited by the minimum detectable bead displacement as well as maximum bead density, which is not only restricted by pore structure and bead size, but can also

influence ECM properties with excessive loading. There is a growing body of correlations between bulk ECM stiffness and cell phenotype in tissue models including progenitor cell differentiation[51], regulation of cell colony size[52], and signaling pathways that regulate tumor growth[53]. Cells in these experiments are seeded within a set of ECMs, each with unique but homogenous bulk stiffness, with shear moduli spanning 30 to ~1000 Pa. If we estimate shear moduli values from our observed α (under assumption of a material continuum and using the Generalized Stokes-Einstein Relation[32]), which inherently introduces error), then remarkably this same range was observed by AMR around single cells in our study. This begs the question: which stiffness value is important? We speculate that no single value of stiffness guides cells, rather it is the evolution and distribution of stiffness that is important.

2.6 ACKNOWLEDGMENTS

We thank Tim Tran and Linda McCarthy for their assistance in cell culture. We thank the funding sources that made this research possible (NSF Physical and Engineering Sciences in Oncology Grant CMMI-1233697, National Institute of Health (NIH)/National Institute of Child Health and Human Development (NICHD) T32 Pre-doctoral Training Grant HD060555-05, NIH/National Heart, Lung, and Blood Institute (NHLBI) T32 pre-doctoral Training Grant HL116270, and the Laser Microbeam and Medical Program, a National Biomedical Technology Resource (NIH P41-EB015890), (NHLBI-R01HL085339). The content is solely the responsibility of the authors and does not necessarily represent the official views of the NCI, NIH, NSF, NICHD or NHLBI.

2.7 SUPPLEMENTAL MATERIAL

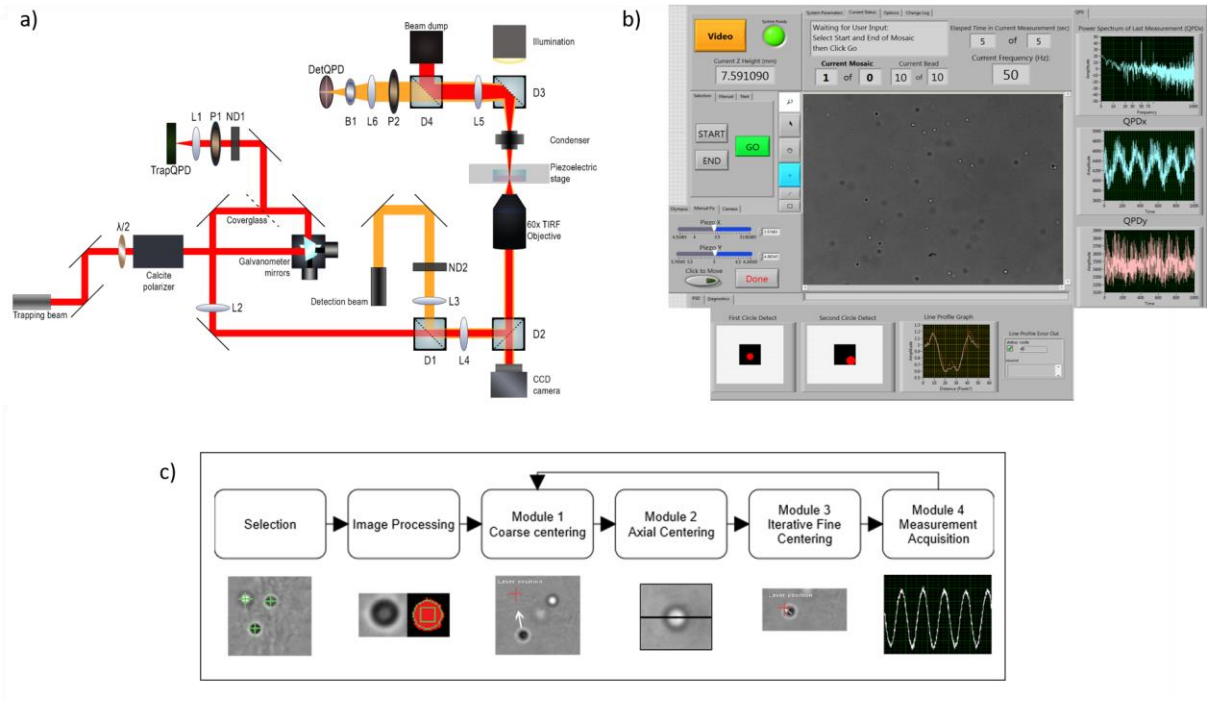

Supp. Figure 2.1: Depiction of AMR apparatus and algorithm. ***(a)*** *Optical tweezers system layout. The optical components are: λ/2 (half-wave plate), L (Lens), P (linear polarizer), D (dichroic mirror) and ND (neutral density filter). A detailed description can be found in the* ***Methods****. Details concerning calculation of the complex material response can be found in* ***Supplementary Note 1****.* ***(b)*** *The AMR User Interface provides user control over parameters and the display of signals in real time.* ***(c)*** *Flow-chart of AMR; details in* ***Supplementary Note 2****.*

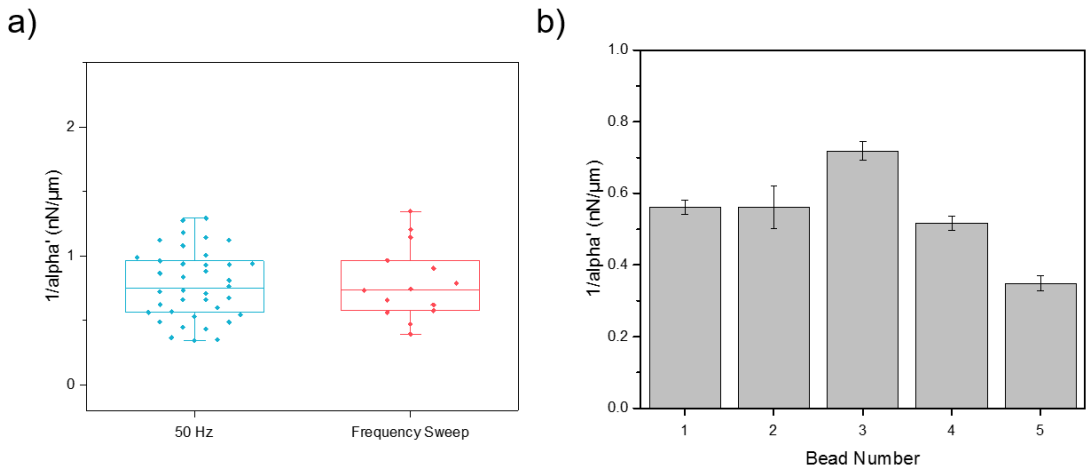

Supp. Figure 2.2: ***(a)*** *1/α' measured in a collagen gel as determined by either (i) oscillating the optical tweezers at single oscillation frequency (50 Hz, n = 38) or (ii) as the average 1/α' across a frequency sweep of 10, 20, 50, 75, and 100 Hz (n = 14). No significant differences were detected between the two measurements (p > 0.8).* ***(b)*** *1/α' values for five beads chosen at random in 2.0 mg/ml collagen gel and separated by at least the range of the piezoelectric x-y stage (~100um). The automation system cycled between the five beads five times.*

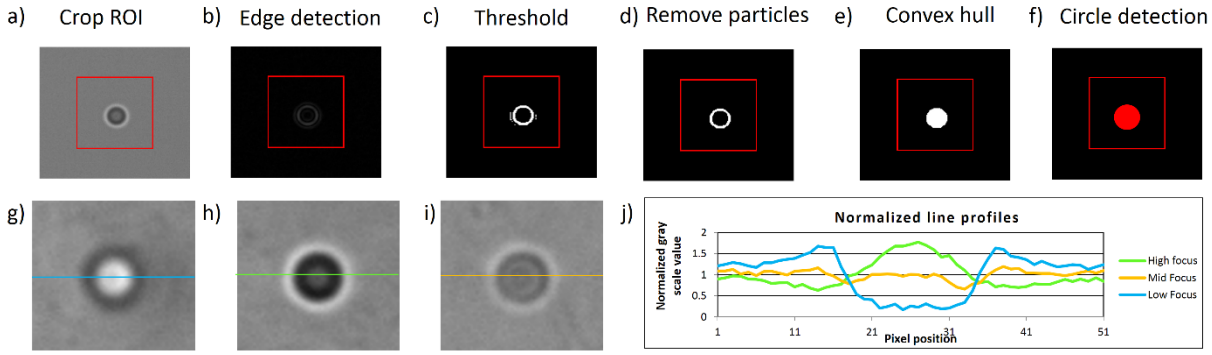

Supp. Figure 2.3: Centering a microbead in the optical trap. ***(a)*** *First a region of interest is automatically created around each bead (graphically displayed by red box). Then the National Instruments (NI) Vision toolkit implements* ***(b)*** *edge detection,* ***(c)*** *binary thresholding,* ***(d)*** *removal of small particles,* ***(e)*** *a convex hull operation and* ***(f)*** *circle detection to determine the bead center coordinates. Axial centering of a bead within the focal plan is accomplished using a custom line-profile algorithm. A line profile through a bead is compared to a reference stack of profiles to determine the focal position of that bead. Representative images of beads below* ***(g),*** *above* ***(h),*** *and at focus* ***(i)*** *are shown along with their normalized line profiles* ***(j)****. Details on 3D centering can be found in* ***Supplementary Note 2****.*

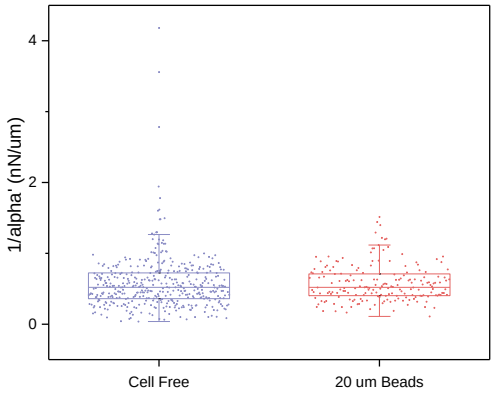

Supp. Figure 2.4: Stiffness proximal to cell-size rigid spheres (polystyrene, E~1 GPa) shows similar heterogeneity to a cell-free gel. 1/α' measured by AMR within 1 mg/mL type 1 collagen cell-free gels (N=3, n_{beads}= 422) and gels also containing 20 µm diameter polystyrene beads (N=3, n_{beads}= 190). There was no significant difference between the two conditions (p=0.26).

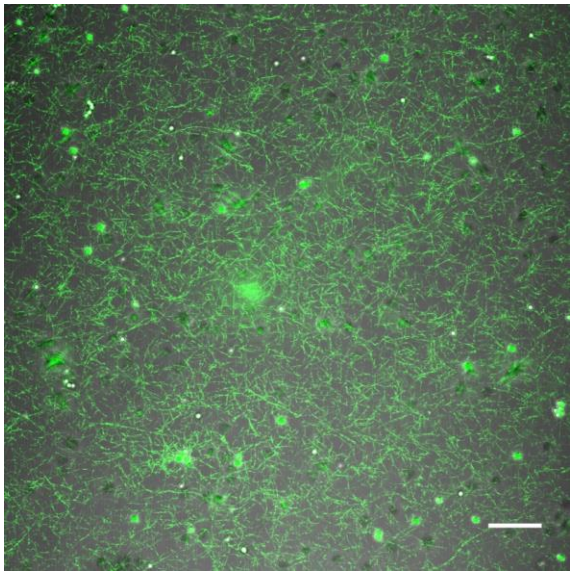

Supp. Figure 2.5: Composite of transmitted light and reflection confocal images. Images are max intensity projections of a 4 µm stack with 1 µm step size. The field of view contains microbeads (2 µm in diameter) within a 1 mg/mL collagen gel. Microbeads that are within the 4 µm stack (i.e. white arrows) appear to be surrounded by fibrous ECM. Beads that appear bright white are above the in-focus planes. Scale bar = 20 µm.

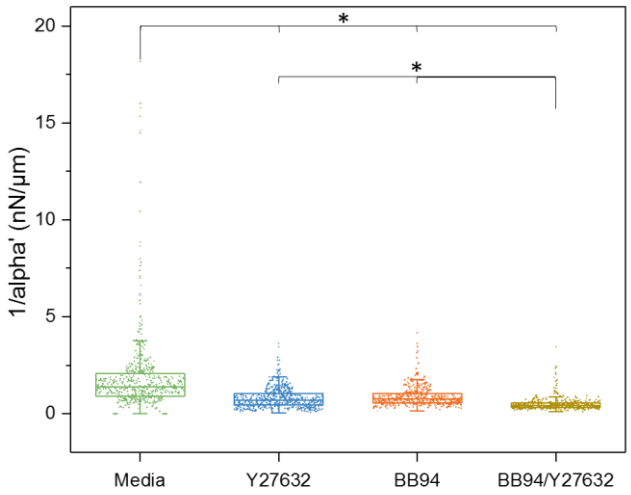

*Supp. Figure 2.6: Effects of drug treatment on pericellular stiffness distribution around isolated HAoSMCs. (**a**) AMR measurements of 1/α' in a ~280 x 280 μm² region surrounding isolated HAoSMCs embedded in 2 mg/ml type 1 collagen gels under control conditions (n_{cells} = 3; n_{beads} = 506) as well as treatments with 20 μM Y27632 (n_{cells} = 4; n_{beads} = 583), 10 μM BB94 (n_{cells} = 3; n_{beads} = 428) and BB94+ Y27632 (n_{cells} = 3; n_{beads} = 417). Each experimental condition was significantly different as compared to control. Additionally, BB94+Y27632 was different as compared to Y27632 and BB94 (*, p << 0.001).*

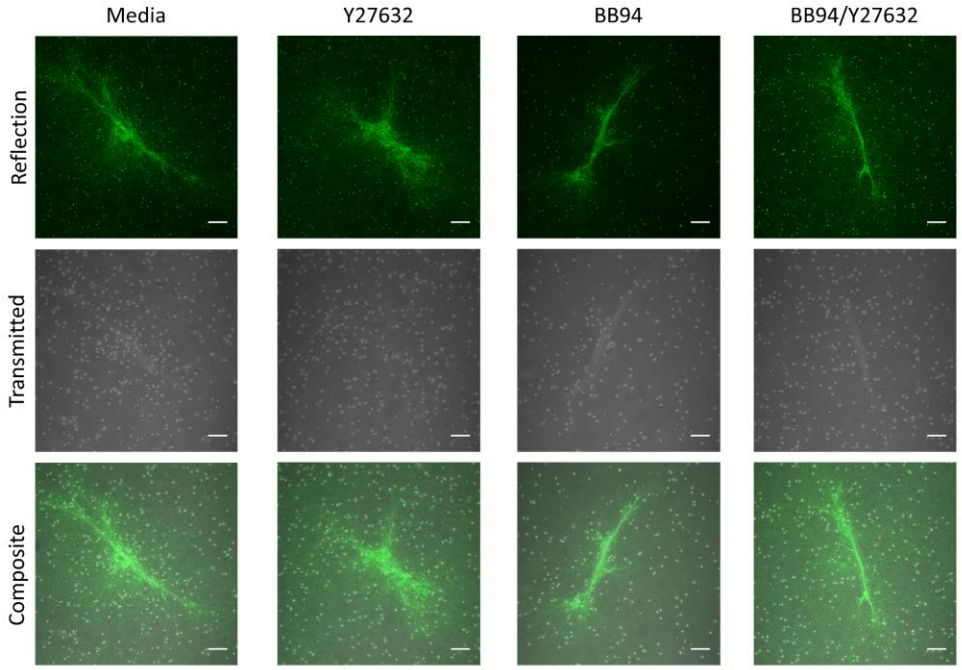

Supp. Figure 2.7: Maximum intensity projections of 30 μm thick image z-stacks (1 μm step) of reflection confocal and transmitted light. Images contain DFs within a 1mg/mL type 1 collagen gel, per condition. Scale bar = 20 μm.

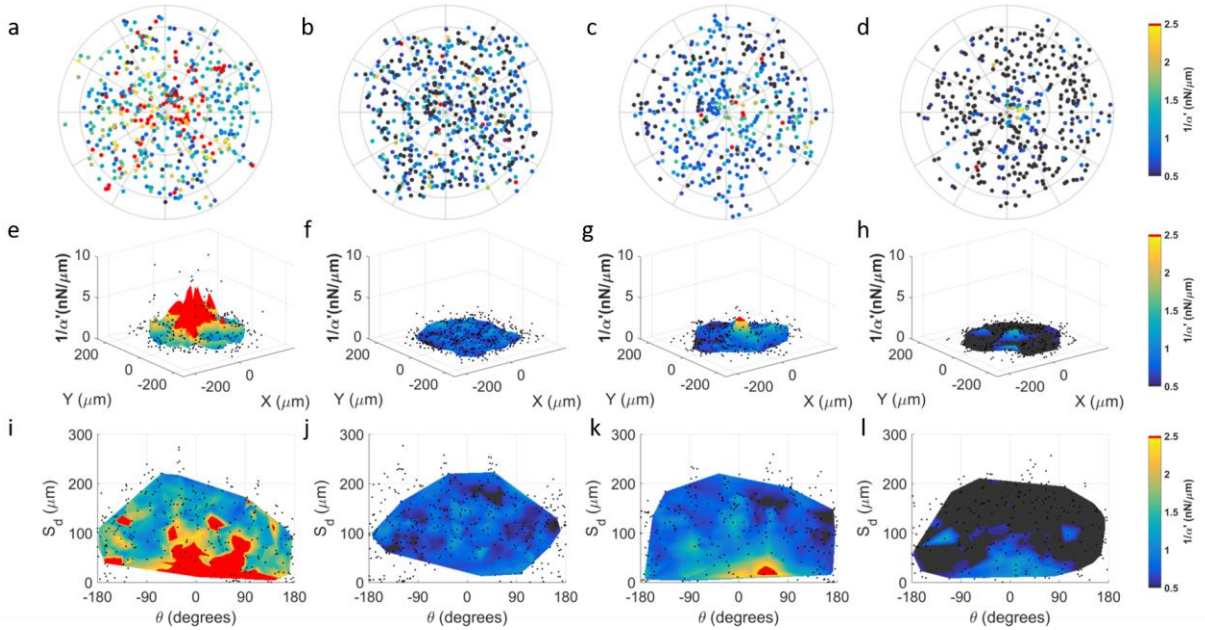

*Supp. Figure 2.8: Characterization of pericellular stiffness for multiple isolated HAoSMCs. Polar plots of 1/α' surrounding isolated cells for (**a**) control (n_{cells} = 3), (**b**) 20 μM Y27632 (n_{cells} = 4), (**c**) 10 μM BB94 (n_{cells} = 3) and (**d**) BB94+Y27632 (n_{cells} = 3) conditions. Concentric lines are drawn in 50 μm increments of r. (**e-h**) 3D surface plots of the aggregate data in (**a-d**), respectively. (**i-l**) Data in (**a-d**) mapped to a Cartesian plot of θ vs. distance from cell boundary, S_d. For (**e-l**), probed beads are denoted by black dots. Data interpolation is restricted to regions containing data from all cells, per condition. Color maps in (**a-d** and **i-l**) range approximately from the average 1/α' value of BB94+Y27632 to the average 1/α' value plus one standard deviation of the control condition. Note that the color map saturates at 2.5 nN/μm.*

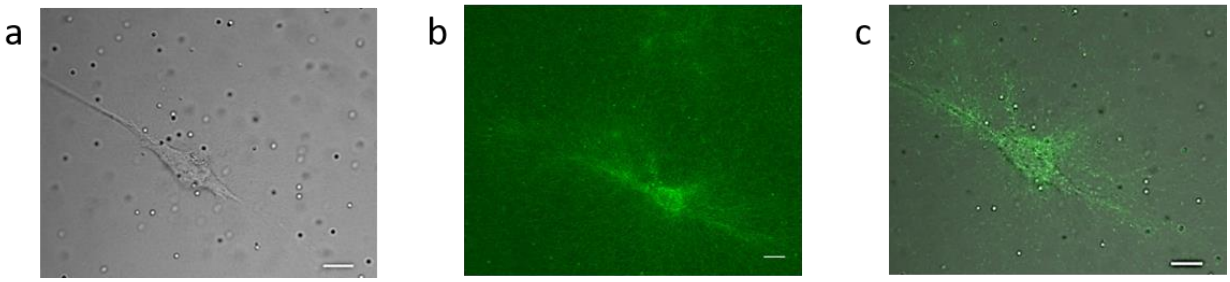

Supp. Figure 2.9: HAoSMC in 2.0 mg/mL type 1 collagen. (a) Brightfield image of an isolated HAoSMC embedded within type 1 collagen gel with 2 μm diameter silica microbeads. (b) Reflection confocal microscopy image of the region in (a) showing both the cell and the fibrous collagen matrix. (c) Merged brightfield and confocal images. Scale bars are 20 μm.

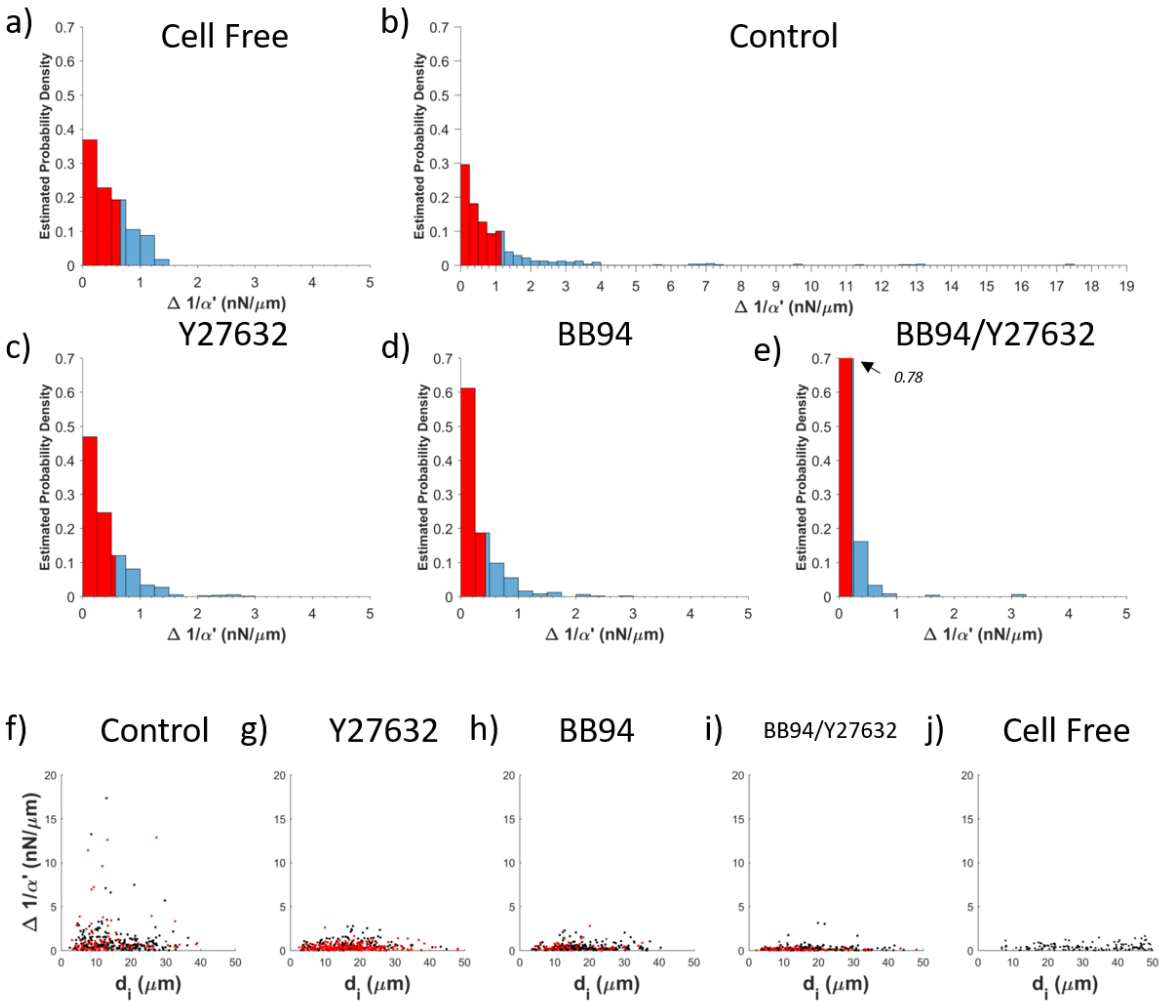

*Supp. Figure 2.10: Variability in stiffness between adjacent beads. For each bead, d_i is the distance to its closest neighbor. Estimated probability density of Δ1/α' in (**a**) 2.0 mg/mL cell free collagen as well as collagen gels containing DFs under (**b**) control conditions or treatment with (**c**) Y27632, (**d**) BB94 or (**e**) both. Red shaded region represents 75% of the data. (**f-i**) Scatter plots of d_i and Δ1/α' for HAoSMCs under (**f**) control conditions or treatment with (**g**) Y27632, (**h**) BB94 or (**i**) both. Red dots indicate beads within $S_d < 50$ μm and black dots indicate beads within $S_d > 50$ μm. (**j**) Scatter plots of d_i and Δ1/α' for a cell-free collagen gel.*

2.7.1 Supplementary Note 1

2.7.1.1 System alignment and calibration

Before each experiment, the optical tweezers and particle detection laser beams are co-aligned and optical trap stiffness κ_t is determined. First, the detection beam optically traps a microbead alone in water so that the bead exhibits Brownian motion in the trap. The stiffness of the detection beam optical trap is at least one order of magnitude weaker than the primary optical trap and has negligible influence on our measurements of $1/\alpha'$ (empirically observed). Next, the position of detQPD is adjusted so the mean position of the detection beam in the trap corresponds to 0V on the detector. Specifically, the position of the detQPD is adjusted in the transverse plane by a micrometer-driven stage until $\langle Vdet, x\rangle = \langle Vdet, y\rangle = 0$ V, where $\langle Vdet, x\rangle$ and $\langle Vdet, y\rangle$ are the mean x and y analog outputs of the detQPD. Next, in order to co-align both beams, the trapping beam traps the same microbead. The galvanometer mirrors are steered in order to position the trapping beam until once again until $\langle Vdet, x\rangle = \langle Vdet, y\rangle = 0$ V. Laser co-alignment is further optimized by adjusting the galvanometer mirrors until a linear response is observed in the detQPD signal as the trapping beam is oscillated in either the x or y axis in a triangle wave around the center of the detection beam. The mean position of the oscillation is adjusted until the detQPD is devoid of nonlinear aberrations such as flattened peaks and valleys or amplitude inversions at the peaks and valleys.

Next, κ_t is calculated from the Brownian motion of a trapped microbead using the power spectrum method[54]. Briefly, a microbead is trapped and positioned in the center of the detection beam focus. Then, detQPD signals are sampled for 30 seconds at 100 kHz. The power spectra of those signals are then fit to a Lorentzian function and κ_t is determined from the corner frequency f_c by the following relationships:

$$\kappa_t = f_c 2\pi\gamma \quad (1)$$

$$\gamma = 6\pi\eta r \quad (2)$$

where γ is the viscous drag coefficient, η the viscosity of water and r the radius of the bead.

2.7.1.2 Optical tweezers active microrheology

In optical tweezers AMR, the transverse position of the optical trap focus is oscillated as a sinusoid by galvanometer mirrors. The extracellular matrix surrounding the bead resists bead motion through both elastic storage and viscous dissipation. This modulates the amplitude and phase of the bead oscillation relative to the optical trap. The pointing position of the trapping beam is detected by the trapQPD (**Supp. Figure 2.1**). The local complex material response α, which is representative of the local matrix surrounding the bead[55], is then computed from trapQPD and detQPD signals. More details can be found in our previous publication[55] and seminal papers by others in the field[32,39]. Briefly, two waveforms are extracted from detQPD and trapQPD signals, which correspond to the bead position $x_B(t)$ and trapping beam position $x_T(t)$, respectively. The force waveform $f(t)$ is then computed as:

$$f(t) = \kappa_t (x_T(t) - x_B(t)) \quad (3)$$

Taking the Fourier transforms of $x_B(t)$ and $f(t)$ we can compute the complex valued material response function $A(\omega)$:

$$X(\omega) = A(\omega)F(\omega) \quad (4)$$

To account for the influence of the optical trap, a corrected material response function α is determined[39]:

$$\alpha(\omega) = A(\omega) \Big/ 1 - \kappa_t A(\omega) \quad (5)$$

If a continuum with the surrounding material is assumed, the complex shear modulus *G* can be computed using the Generalized Stokes-Einstein Relation[39], which relates the drag force on a spherical object to complex material properties so that

$$G(\omega) = {}^{1}/_{6\pi r\alpha(\omega)} \tag{6}$$

$$G(\omega) = G'(\omega) + iG''(\omega) \tag{7}$$

where *G'* and *G''* are the elastic and loss modulus, respectively.

2.7.2 Supplementary Note 2

2.7.2.1 Automation Algorithm

All software modules of the AMR system were developed in LabVIEW 2012 with the NI Vision package. A screenshot of the automation software interface is shown in **Supp. Figure 2.1b** and a flow chart of the automation sequence is depicted in **Supp. Figure 2.1c**. The automation software is broken down into modules explained below.

Module 1: Coarse centering of beads in the optical trap

At the start of experiments the user uses a mouse to manually click on all the beads to be probed. To convert the clicked positions into the precise (x,y) coordinate of each bead, a 60 pixel x 60 pixel region of interest (ROI) is programmatically cropped around each mouse click (**Supp. Figure 2.3a**). The size of the ROI was chosen to be large enough to ensure the entire 2μm bead (diameter ~ 20 pixels) is within the ROI. An edge-enhanced image is computed using the Sobel edge detection algorithm (**Supp. Figure 2.3b**) from which a binary image mask is computed using a background correction based thresholding algorithm with a 32x32 window (**Supp. Figure 2.3c**). The binary image can contain small pixel noise which is removed by a small

particle filter (**Supp. Figure 2.3d**). Next, the mask is filled in using a convex hull algorithm (**Supp. Figure 2.3e**). Lastly, the centroid of the circle corresponding to the bead center in the (x,y) plane (**Supp. Figure 2.3f**). If multiple beads are in the ROI, we only consider the detected circle closest to the center of the ROI. The algorithm quickly analyzes all ROIs and generates a matrix of bead centers relative to the top left corner of the field of view. The piezoelectric stage is moved to bring each bead center near to the optical trap. Moving the stepper motor stage allows for stitching of measurements in multiple fields of view together. In the next modules, the bead is finely centered in the optical trap, along all three coordinate axes.

Module 2: Axial Centering: Line Profiling

The bead is brought into focus using a custom line-profile algorithm adapted from a previously described method[10]. Microbead diffraction patterns in brightfield illumination change with axial position relative to the microscope objective plane. Example reference planes and their corresponding intensity line profiles are shown in **Supp. Figure 2.3g-j**. For each grayscale bead image, we compute the mean square error between a line profile through the center of the bead and each of the 111 line profiles extracted from a reference image stack. The reference image stack is a z-series through a reference bead in a hydrogel taken with a 0.05μm step size. The axial position of the reference line scan that minimizes the mean square error is the axial distance between the bead current focal position and true focus. The objective lens is moved by this distance. To compensate for error in the microscope focus motor, this process is repeated iteratively until the axial distance between the bead and true focus is less than 0.05 μm. Typically 3 to 4 iterations are necessary. If the criteria cannot be achieved within 10 iterations, the bead is removed from data analysis.

Module 3: Iterative Fine Centering

Once a bead is placed into focus by Module 2, its (x,y) position relative to the laser focus can then be optimized by deliberately shifting the focus by exactly 2 μm (empirically determined) and repeating Module 1. The 2 μm shift generates a high contrast bead diffraction pattern, and thus a high contrast line scan. To compensate for errors in stage motion Module 1 is iterated until the bead center is at the same pixel location as the laser focus. If the criteria cannot be achieved within 10 iterations, the bead is removed from data analysis.

Module 4: Measurement Acquisition

After centering the bead, AMR and data analysis is performed as described previously and in **Supplementary Note 1**.

2.8 REFERENCES

1. Paszek, M. J. *et al.* Tensional homeostasis and the malignant phenotype. *Cancer Cell* **8,** 241–254 (2005).
2. Park, J. S. *et al.* The effect of matrix stiffness on the differentiation of mesenchymal stem cells in response to TGF-β. *Biomaterials* **32,** 3921–3930 (2011).
3. Chaudhuri, O. & Mooney, D. J. Stem-cell differentiation: Anchoring cell-fate cues. *Nat. Mater.* **11,** 568–569 (2012).
4. Young, J. L., Kretchmer, K., Ondeck, M. G., Zambon, A. C. & Engler, A. J. Mechanosensitive kinases regulate stiffness-induced cardiomyocyte maturation. *Sci. Rep.* **4,** 6425 (2014).
5. Kumar, S. & Weaver, V. M. Mechanics, malignancy, and metastasis: The force journey of a tumor cell. *Cancer Metastasis Rev.* **28,** 113–127 (2009).
6. Legant, W. R. *et al.* Measurement of mechanical tractions exerted by cells in three-dimensional matrices. *Nat. Methods* **7,** 969–71 (2010).
7. Gjorevski, N. & Nelson, C. M. Mapping of mechanical strains and stresses around quiescent engineered three-dimensional epithelial tissues. *Biophys. J.* **103,** 152–162 (2012).
8. Mann, B. K., Gobin, A. S., Tsai, A. T., Schmedlen, R. H. & West, J. L. Smooth muscle cell growth in photopolymerized hydrogels with cell adhesive and proteolytically degradable domains: Synthetic ECM analogs for tissue engineering. *Biomaterials* **22,** 3045–3051 (2001).
9. Daley, W. P., Peters, S. B. & Larsen, M. Extracellular matrix dynamics in development and regenerative medicine. *J. Cell Sci.* **121,** 255–64 (2008).
10. Bloom, R. J., George, J. P., Celedon, A., Sun, S. X. & Wirtz, D. Mapping local matrix remodeling induced by a migrating tumor cell using three-dimensional multiple-particle tracking. *Biophys. J.* **95,** 4077–88 (2008).
11. Licup, A. J. *et al.* Stress controls the mechanics of collagen networks. *Proc. Natl. Acad. Sci.* **112,** 201504258 (2015).
12. Vader, D., Kabla, A., Weitz, D. & Mahadevan, L. Strain-induced alignment in collagen gels. *PLoS One* **4,** (2009).
13. Wozniak, M. a & Chen, C. S. Mechanotransduction in development: a growing role for contractility. *Nat. Rev. Mol. Cell Biol.* **10,** 34–43 (2009).

14. Lu, P., Takai, K., Weaver, V. M. & Werb, Z. Extracellular matrix degradation and remodeling in development and disease. *Cold Spring Harb Perspect Biol* **3,** 1–24 (2011).
15. Oblander, S. A. *et al.* Distinctive functions of membrane type 1 matrix-metalloprotease (MT1-MMP or MMP-14) in lung and submandibular gland development are independent of its role in pro-MMP-2 activation. *Dev. Biol.* **277,** 255–269 (2005).
16. Ghajar, C. M. *et al.* Mesenchymal cells stimulate capillary morphogenesis via distinct proteolytic mechanisms. *Exp. Cell Res.* **316,** 813–825 (2010).
17. Sabeh, F. *et al.* Tumor cell traffic through the extracellular matrix is controlled by the membrane-anchored collagenase MT1-MMP. *J. Cell Biol.* **167,** 769–781 (2004).
18. Holmbeck, K. *et al.* MT1-MMP-deficient mice develop dwarfism, osteopenia, arthritis, and connective tissue disease due to inadequate collagen turnover. *Cell* **99,** 81–92 (1999).
19. Kotlarchyk, M. A. *et al.* Concentration independent modulation of local micromechanics in a fibrin gel. *PLoS One* **6,** (2011).
20. Tang, Y. *et al.* MT1-MMP-Dependent Control of Skeletal Stem Cell Commitment via a β1-Integrin/YAP/TAZ Signaling Axis. *Dev. Cell* **25,** 402–416 (2013).
21. Kurup, A. *et al.* Novel insights from 3D models: the pivotal role of physical symmetry in epithelial organization. *Sci. Rep.* **5,** 15153 (2015).
22. Velegol, D. & Lanni, F. Cell traction forces on soft biomaterials. I. Microrheology of type I collagen gels. *Biophys. J.* **81,** 1786 (2001).
23. Blehm, B. H., Devine, A., Staunton, J. R. & Tanner, K. In vivo tissue has non-linear rheological behavior distinct from 3D biomimetic hydrogels, as determined by AMOTIV microscopy. *Biomaterials* **83,** 66–78 (2016).
24. Kniazeva, E. *et al.* Quantification of local matrix deformations and mechanical properties during capillary morphogenesis in 3D. *Integr. Biol. (Camb).* **4,** 431–9 (2012).
25. Tang, Y. *et al.* MT1-MMP-Dependent Control of Skeletal Stem Cell Commitment via a β1-Integrin/YAP/TAZ Signaling Axis. *Dev. Cell* **25,** 402–416 (2013).
26. Di Lullo, G. A., Sweeney, S. M., Körkkö, J., Ala-Kokko, L. & San Antonio, J. D. Mapping the ligand-binding sites and disease-associated mutations on the most abundant protein in the human, type I collagen. *J. Biol. Chem.* **277,** 4223–4231 (2002).
27. Rensen, S. S. M., Doevendans, P. A. F. M. & van Eys, G. J. J. M. Regulation and characteristics of vascular smooth muscle cell phenotypic diversity. *Neth. Heart J.* **15,** 100–8 (2007).
28. Tracy, L. E., Minasian, R. a. & Caterson, E. J. Extracellular Matrix and Dermal Fibroblast Function in the Healing Wound. *Adv. Wound Care* **5,** 119–136 (2016).
29. Doyle, A. D., Carvajal, N., Jin, A., Matsumoto, K. & Yamada, K. M. Local 3D matrix microenvironment regulates cell migration through spatiotemporal dynamics of contractility-dependent adhesions. *Nat. Commun.* **6,** 8720 (2015).
30. Frigault, M. M., Lacoste, J., Swift, J. L. & Brown, C. M. Live-cell microscopy - tips and tools. *J. Cell Sci.* **122,** 753–767 (2009).
31. Shayegan, M. & Forde, N. R. Microrheological Characterization of Collagen Systems: From Molecular Solutions to Fibrillar Gels. *PLoS One* **8,** 23–28 (2013).
32. Brau, R. R. *et al.* Passive and active microrheology with optical tweezers. *J. Opt. A Pure Appl. Opt.* **9,** S103–S112 (2007).
33. Gardel, M. L., Valentine, M. T. & Weitz, D. A. Microrheology. *Microscale Diagnostic Tech.* 1–49 (2005). doi:10.1007/3-540-26449-3_1
34. Chaikin, P. M. & Lubensky, T. C. *Principles of condensed matter physics*. (Cambridge university press, 2000).
35. Mizuno, D., Tardin, C., Schmidt, C. F. & Mackintosh, F. C. Nonequilibrium mechanics of active cytoskeletal networks. *Science* **315,** 370–3 (2007).
36. Schultz, K. M., Kyburz, K. a & Anseth, K. S. Measuring dynamic cell-material interactions and remodeling during 3D human mesenchymal stem cell migration in hydrogels. *Proc. Natl. Acad. Sci. U. S. A.* **112,** E3757-3764 (2015).
37. Nijenhuis, N., Mizuno, D., Spaan, J. a. E. & Schmidt, C. F. High-resolution microrheology in the pericellular matrix of prostate cancer cells. *J. R. Soc. Interface* **9,** 1733–1744 (2012).
38. Schultz, K. M. *et al.* Electrospinning covalently cross-linking biocompatible hydrogelators. *Polymer (Guildf).* **54,** 363–371 (2013).

39. Mizuno, D., Head, D. a., MacKintosh, F. C. & Schmidt, C. F. Active and Passive Microrheology in Equilibrium and Nonequilibrium Systems. *Macromolecules* **41,** 7194–7202 (2008).
40. Fitzgibbon, J., Morrison, J. J., Smith, T. J. & O'Brien, M. Modulation of human uterine smooth muscle cell collagen contractility by thrombin, Y-27632, TNF alpha and indomethacin. *Reprod. Biol. Endocrinol.* **7,** 2 (2009).
41. Ma, X. *et al.* Fibers in the extracellular matrix enable long-range stress transmission between cells. *Biophys. J.* **104,** 1410–1418 (2013).
42. Winer, J. P., Oake, S. & Janmey, P. A. Non-linear elasticity of extracellular matrices enables contractile cells to communicate local position and orientation. *PLoS One* **4,** (2009).
43. Tan, J. L. *et al.* Cells lying on a bed of microneedles: an approach to isolate mechanical force. *Proc. Natl. Acad. Sci. U. S. A.* **100,** 1484–9 (2003).
44. Saez, A., Ghibaudo, M., Buguin, A., Silberzan, P. & Ladoux, B. Rigidity-driven growth and migration of epithelial cells on microstructured anisotropic substrates. *Proc. Natl. Acad. Sci. U. S. A.* **104,** 8281–6 (2007).
45. Jin, T., Li, L., Siow, R. C. M. & Liu, K.-K. A novel collagen gel-based measurement technique for quantitation of cell contraction force. *J. R. Soc. Interface* **12,** 20141365 (2015).
46. Abhilash, A. S., Baker, B. M., Trappmann, B., Chen, C. S. & Shenoy, V. B. Remodeling of fibrous extracellular matrices by contractile cells: Predictions from discrete fiber network simulations. *Biophys. J.* **107,** 1829–1840 (2014).
47. Caliari, S. R., Vega, S. L., Kwon, M., Soulas, E. M. & Burdick, J. A. Dimensionality and spreading influence MSC YAP/TAZ signaling in hydrogel environments. *Biomaterials* **103,** 314–323 (2016).
48. Brown, A. C. *et al.* Molecular interference of fibrin's divalent polymerization mechanism enables modulation of multiscale material properties. *Biomaterials* **49,** 27–36 (2015).
49. Fong, A. H. *et al.* Three-Dimensional Adult Cardiac Extracellular Matrix Promotes Maturation of Human Induced Pluripotent Stem Cell-Derived Cardiomyocytes. *Tissue Eng. Part A* **22,** 1016–1025 (2016).
50. Romero-López, M. *et al.* Recapitulating the human tumor microenvironment: Colon tumor-derived extracellular matrix promotes angiogenesis and tumor cell growth. *Biomaterials* **116,** 118–129 (2017).
51. Kraehenbuehl, T. P. *et al.* Three-dimensional extracellular matrix-directed cardioprogenitor differentiation: Systematic modulation of a synthetic cell-responsive PEG-hydrogel. *Biomaterials* **29,** 2757–2766 (2008).
52. Liu, J. *et al.* Soft fibrin gels promote selection and growth of tumorigenic cells. *Nat. Mater.* **11,** 734–41 (2012).
53. Chaudhuri, O. *et al.* Extracellular matrix stiffness and composition jointly regulate the induction of malignant phenotypes in mammary epithelium. *Nat. Mater.* **13,** 1–35 (2014).
54. Gittes, F. & Schmidt, C. F. Chapter 8 Signals and Noise in Micromechanical Measurements. *Methods Cell Biol.* **55,** 129–156 (1997).
55. Kotlarchyk, M. A., Botvinick, E. L. & Putnam, A. J. Characterization of hydrogel microstructure using laser tweezers particle tracking and confocal reflection imaging. *J. Phys. Condens. Matter* **22,** 194121 (2010).

CHAPTER 3: SPROUTING ANGIOGENESIS INDUCES SIGNIFICANT MECHANICAL HETEROGENEITIES AND ECM STIFFENING ACROSS LENGTH SCALES IN FIBRIN HYDROGELS

Benjamin A. Juliar[1,*], **Mark T. Keating**[2,*], Yen P. Kong[1], Elliot L. Botvinick[2,+], and Andrew J. Putnam[1,+]

[1]Department of Biomedical Engineering, University of Michigan; Ann Arbor, Michigan
[2]Department of Biomedical Engineering, University of California, Irvine; Irvine, California

[*]BAJ and MTK are co-first authors
[+]ELB and AJP are co-corresponding authors

[+] **Corresponding authors:**
Elliot L. Botvinick, Ph.D.
Email: elliot.botvinick@uci.edu

Andrew J. Putnam, Ph.D.
E-mail: putnam@umich.edu

Keywords: Endothelial cells; Fibrin; Fibroblasts; Microrheology; Microvasculature; Optical tweezer

3.1 ABSTRACT

Matrix stiffness is a well-established instructive cue in two-dimensional cell cultures. Its roles in morphogenesis in 3-dimensional (3D) cultures, and the converse effects of cells on the mechanics of their surrounding microenvironment, have been more elusive given the absence of suitable methods to quantify stiffness on a length-scale relevant for individual cell-extracellular matrix (ECM) interactions. In this study, we applied traditional bulk rheology and laser tweezers-based active microrheology to probe mechanics across length scales during the complex multicellular process of capillary morphogenesis in 3D, and further characterized the relative contributions of neovessels and supportive stromal cells to dynamic changes in stiffness over time. Our data show local ECM stiffness was highly heterogeneous around sprouting capillaries, and the variation progressively increased with time. Both endothelial cells and stromal support cells progressively stiffened the ECM, with the changes in bulk properties dominated by the latter. Interestingly, regions with high micro-stiffness did not necessarily correlate with remodeled regions of high ECM density as shown by confocal reflectance microscopy. Collectively, these findings, especially the large spatiotemporal variations in local stiffness around cells during morphogenesis in soft 3D fibrin gels, underscore that characterizing ECM mechanics across length scales. provides an opportunity to attain a deeper mechanobiological understanding of the microenvironment's roles in cell fate and tissue patterning.

3.2 INTRODUCTION

Numerous cell types demonstrate differential phenotypic responses and differentiation potential depending on the elasticity of the environment in which they reside[1]. Tuning substrate rigidity in 2D, ostensibly without altering porosity, diffusive transport, or ligand density, alters cell spreading[2,3], proliferation[4,5], migration[3,6], and differentiation[7,8]. Despite the interdependence of elasticity with other properties in real tissues, ECM mechanical properties also appear to control cell fate in 3D[9,10]. Nevertheless, despite considerable interest in the effects of matrix rigidity on cell phenotypes, how cells change the mechanical properties of the surrounding ECM, particularly on a microscale, remains poorly understood. Moreover, the instructive cue of matrix stiffness has largely been treated as unidirectional and static, with measurements of bulk stiffness at a singular initial time point correlated with cell fate. In reality, complex morphogenetic processes in 3D involve dynamic and reciprocal mechanical cross-talk between cells and the surrounding ECM.

ECM stiffness has also been postulated to be an important instructive cue governing capillary morphogenesis[11], affecting the magnitudes of contractile forces endothelial cells (ECs) exert on their surroundings to control their invasive abilities[12]. We have previously shown that EC contractile forces are essential for capillary morphogenesis[13], and the rate at which ECs deform ECM fibers depends on the initial matrix concentration and correlates with the rate at which they form vessel-like structures in 3D[14]. However, different material platforms and cross-linking schemes have led to discrepancies in the literature, with some studies suggesting softer matrices are more supportive of vascular morphogenesis and others reporting higher stiffness yields more invasion. Regardless, across all material platforms, the spatiotemporal evolution of ECM micromechanics during angiogenic sprouting remains unclear.

In this study, we exploited a well characterized model of angiogenic sprouting in which ECs coated on microcarrier beads invade a 3D fibrin matrix when co-cultured with stromal fibroblasts[15,16]. Fibrin is the major component of the provisional matrix in a blood clot[17], and thus is a suitable model for investigating the mechanical evolution of ECM during wound healing. Fibroblasts secrete pro-angiogenic cytokines and other factors that are essential for EC tubulogenesis when co-embedded with ECs in the fibrin matrix, where they can act in a pericyte-like manner and directly associate with the nascent capillaries[18], or overlaid on top of the gels as a monolayer[19,20]. In addition to supporting angiogenesis, fibroblasts play important roles in wound closure and healing by increasing contractility and depositing ECM[21], both of which effect the elasticity of the matrix[20,22].

Through a combination of shear rheology to track bulk elastic properties and laser-based optical tweezers active microrheology (AMR) to quantify elasticity on a length scale relevant for individual cells, we explicitly quantified changes in ECM mechanics across length scales, over time, and with unprecedented resolution during the complex morphogenetic process of angiogenic sprouting *in vitro*. Our findings reveal significant mechanical heterogeneities encountered by cells on the microscale, and demonstrate the extent to which the ECs themselves alter the mechanical properties of the surrounding ECM. We further assessed whether pericytic association affects the rate and degree to which local ECM stiffening occurs, and determined the effect fibroblasts have on the ECM when distant from sprouting microvasculature. Collectively, this study highlights the importance of characterizing ECM mechanical properties on an appropriate length scale and over time, as initial bulk characterization misses the dynamic and highly varied environment individual cells experience.

3.3 MATERIALS AND METHODS

Cell culture: Normal human dermal fibroblasts (DFs, Lonza, Walkersville, MD) were cultured in Dulbecco's modified eagle medium (DMEM, Life Technologies, Grand Island, NY) supplemented with 10% fetal bovine serum (FBS, Life Technologies) and 1% penicillin streptomycin (Life Technologies) and were used up to passage 7. Human umbilical vein endothelial cells (ECs) were either harvested from fresh umbilical cords as previously described[15] or purchased from a commercial source (Lonza). Two different sources of ECs were used to ensure robustness of the observed biological responses. The ability of these two different sources of HUVECs to sprout in our fibrin-based assays was quantitatively equivalent (data not shown). HUVECs for all experiments were cultured in fully supplemented EGM2 (Lonza) and used between passages 2-4. Media for both cell types were exchanged 3 times a week and cells were harvested below 80% confluence using 0.05% trypsin-EDTA (Life Technologies).

Fibrin-based capillary morphogenesis assay: A three-dimensional cell culture model of capillary morphogenesis was assembled following adapted protocols as previously described[15,16,23]. Briefly, EC-coated microbeads were embedded in fibrin gels with DFs either embedded or overlaid on the gel as a monolayer. A stock solution of sterilized Cytodex microcarrier beads (Sigma-Aldrich, St Louis, MO) was prepared ahead of time by autoclaving in PBS. The day before construct assembly, microbeads were coated with ECs by combining $1x10^4$ microbeads with $4x10^6$ ECs in 5 mL of EGM2 in an upright T-25 tissue culture flask (Corning Inc, Corning, NY). The flask was incubated for 4 hours with periodic agitation every 30 minutes. Afterwards, 5 mL of fresh EGM2 was added, and the 10 mL suspension of freshly coated beads was transferred to a new T-25 and allowed to incubate overnight in the standard tissue culture position. The following day, beads were transferred to a 15 mL conical tube (VWR, Radnor, PA) and allowed to settle by gravity between

two washes with fresh EGM2. Fibrinogen from bovine plasma (Sigma) was dissolved in serum free EGM2 to achieve a final concentration of 2.5 mg/mL clottable fibrinogen upon gelation, and sterile filtered through a 0.22 µm PES membrane filter (Merck Millipore Ltd, Tullagreen, Carrigtwohill, Co. Cork, IRL). For conditions in which the stromal fibroblasts were embedded within the fibrin gel ("embedded") a suspension of DFs was added to the fibrinogen at a final concentration of $2.5x10^4$ cells/mL; for the other conditions, an equal volume of EGM2 was added instead. Microbeads were added to the solution at 50 beads/mL. Heat-inactivated FBS was added to the solution immediately prior to gelation for a final concentration of 5%. Tissue culture dishes were spotted with 40 µL of 100 U/mL thrombin reconstituted in ddH_2O per mL fibrinogen. Dishes were allowed to sit for 5-minutes before being transferred to incubate at 37 °C for another 25 minutes to allow for complete gelation. After gelation, 2 mL of EGM2 per 1 mL of fibrin gel was overlaid for all gels. For conditions in which the stromal fibroblasts were cultured on top of the gel ("overlay"), DFs were introduced in the overlaid EGM2 at a concentration of $2.5x10^4$ cells/mL of fibrin gel to achieve equal DF numbers per gel for both overlay and embedded conditions. For each independent experiment, multiple gels were cast for each time point. Gel constructs (0.5 mL total volume) were fabricated in 24-well tissue culture plates (Corning Inc) for bulk rheology and network quantification assays. For micro-rheology and reflection confocal imaging, gel constructs (1 mL total volume) were fabricated in 35 mm glass bottom dishes (MatTek, Ashland, MA).

For experiments involving Transwell inserts, fibrin based gel constructs (2 mL total volume) were fabricated in the bottom chamber of 6-well Transwell plates (24 mm diameter inserts containing 3.0 µm pores; Corning). DFs were cultured on top of the insert, and DAPI staining was used to confirm these cells did not migrate through the porous insert to the gel surface during the assay. Because the bottom of the insert would rest on the gel if used as provided, sterilized silicon

O-rings (MSC, Melville, NY, part # S70-028) were used to space the insert off the top of the gel. All tissue constructs were cultured for up to two weeks with media exchanged on day 1 and every two days thereafter.

Fluorescent imaging and quantification of capillary morphogenesis: Images were acquired using an Olympus IX81 confocal microscope equipped with a USH-103OL mercury lamp (Olympus America, Center Valley, PA), a Hamamatsu Orca II CCD camera (Hamamatsu Photonics, Hamamatsu City, Japan), and Metamorph Premier software (Molecular Devices, Sunnyvale, CA). For visualization of tubules and cell nuclei, co-cultures were fixed with Z-Fix aqueous buffered zinc formalin fixative (Anatech, Battle Creek, MI) and stained with a rhodamine-conjugated lectin from *Ulex europaeus* (UEA, Vector Laboratories, Burlingame, CA) and 4',6-diamidino-2-phenylindol (DAPI, Sigma-Aldrich). UEA binds glycoproteins and glycolipids specific to endothelial cells. UEA- and DAPI-stained samples were acquired using red (Ex: 562 nm, bandwidth: 40 nm; Em: 641 nm, bandwidth: 75 nm) and blue (Ex: 377 nm, bandwidth: 50 nm; Em: 477 nm, bandwidth: 60 nm) filter sets, respectively. Network length was quantified at days 1, 4, 7, and 14 with all beads imaged at 4x magnification. On day 14, multiple images often had to be stitched together to fit the entire network from a single bead. For unbiased measurements, the microscope was rastered through each gel and all beads were imaged that were far enough away from the edge of plate such that sprouting was unimpinged and did not have overlapping networks with a neighboring bead. This resulted in 8-40 beads per condition for each independent experiment being quantified, with diminishing beads meeting the criteria as time progressed. Three independent experiments (N=3) were conducted for each condition and time point, and the aggregate data from all beads across all 3 independent experiments were presented to illustrate the spread in biological response. Total tube length per bead was quantified using the Angiogenesis

Tube Formation module in Metamorph. The average network length per bead for each condition of each independent experiment was then used for statistical analysis. DF proliferation in overlay conditions was quantified by taking DAPI images of the DFs in a monolayer on top of the gel and manually determining cell density.

Bulk rheology: The bulk mechanical properties of fibrin-based constructs were measured via parallel plate shear rheology using an AR-G2 rheometer (TA Instruments, New Castle, DE) equipped with an 8 mm diameter measurement head and a Peltier stage. Oscillatory shear measurements of 6% strain amplitude and a frequency of 1 rad/sec were performed on days 1, 4, 7, and 14 directly in multi-well tissue culture plates with the rheometer stage maintained at 37 °C. Cell culture media were aspirated before measurements, with a small volume left to ensure the gel remained wet. Rheology of elastic pre-swollen hydrogels typically involves application of a small normal force prior to data acquisition, and/or use of a consistent gap width between the bottom of the sample and the platen. However, fibrin's viscoelasticity precludes use of the former method, while varying degrees of cell-mediated gel compaction over time preclude the latter. Instead, a protocol was developed whereby the top platen was lowered until it made initial contact with the hydrogel, followed by measurements of shear modulus (G') taken at 200 μm intervals while closing the gap between platen and stage. Gels exhibited a plateau in G' as the gap was progressively decreased after making contact with the gel (**Supp. Figure 3.1A/B**). The peak G' measured of 3 gap heights after making contact with the gel was used as our reported value for the given region of interest. One region of interest was interrogated per gel in 24-well plates, and three regions of interest were interrogated per gel in 6-well plates. The measurement head was carefully centered in 24-well plates to avoid edge effects contributing to G' measurements. Comparisons between acellular gels in 24 and 6-well plates over time (2.5 cm^2 and 9.8 cm^2 areas, respectively)

were used to confirm the robustness of the methods across gels of different sizes (**Supp. Figure 3.1C**). Overlay cultures in 6-well plates were also tracked over 14 days to ensure well size did not influence observed stiffening behavior (**Supp. Figure 3.2**). Overlay and embedded conditions with AMR beads included were also tested to ensure bulk G' was unaffected by their inclusion (**Supp. Figure 3.3**). At least 3 measurements were taken per time point per independent experiment. Three independent experiments were conducted (N=3) and for each independent experiment, the gels for all time points were cast from the same stock of reagents.

Laser tweezers-based Active Microrheology: Active microrheology (AMR) was conducted using a dual-laser optical tweezers system, as has been previously described[24] and used in the study of capillary morphogenesis[14]. Briefly, fibrin hydrogels were polymerized as described above within 35 mm glass bottom dishes (MatTek, Ashland, MA) with a dispersion of 2 μm carboxylated silica microbeads (Bangs Laboratories, Fishers, IN) at a concentration of 0.08% (w/v) throughout the hydrogel. During AMR measurements, beads within a volume of approximately 250 x 175 x 30 μm are oscillated at 50 Hz by optical forces induced by a focused 1064 nm laser (trapping beam), at an amplitude of 175 nm. A stationary 785 nm laser (detection beam) was used to detect each probe particle movement in response to the driving force. The oscillation of the input trapping beam and the deflection of the detection beam by the microbead are recorded by a pair of quadrant photodiodes (Newport, Irvine, CA). These measurements allow for calculation of the complex material response α^*. Data here is presented as the real component (G') of the complex shear modulus G^*, computed from α^*, as previously done [25,26]. AMR measurements were performed on days 1, 4, 7, and 14 (N=3, per day, per condition) within a custom-built stage top incubator. The volume measured within each measurement location within cell-free samples was chosen

randomly, while measurements within capillary morphogenesis assays were chosen to be localized around the sprouting endothelial cells or proximal to Cytodex beads on day 1.

Confocal Reflection Microscopy: Reflection confocal stacks were acquired prior to AMR measurement of each sample. Confocal microscopy was conducted using a Fluoview 1200 system (Olympus), integrated into the optical tweezers microscope. Image stacks were imaged using the 488 nm laser line with a depth of approximately 60 μm and step size of 1 μm. For z-projections, stacks were trimmed to remove effect of glass aberration in reflection confocal and in order to keep a consistent number of planes for each z projection. Images were acquired using the same objective as for AMR; 1.45NA 60X TIRF Oil Objective (Olympus).

Statistics: Varying statistical methods were performed depending on the nature of the data analyzed and are indicated as appropriate on the figure captions. For analyzing network length, the average sprout length per bead from 8-40 beads per time point per replicate was considered for statistical analysis in comparing conditions. Linear regression was used for analyzing network length data for embedded and overlay conditions. For analyzing bulk rheology data, the average bulk modulus from 3-6 ROIs per time point per replicate was considered in comparing conditions. Heteroscedastic 2-tail t-tests were used to verify overlay and Transwell conditions had equitable sprouting on any given day, that AMR beads do not influence bulk G' or sprouting, and that culture well size does not influence bulk-G'. One-way ANOVA was used to determine differences in bulk mechanical properties and followed with Tukey HSD post-hoc testing if differences were detected. Mann-Whitney U tests with a Bonferroni correction were performed between pairs of aggregate AMR data.

3.4 RESULTS

3.4.1 DFs stimulate EC neovessel formation when overlaid or embedded in fibrin matrices

ECs cultured on microcarrier beads embedded in fibrin gels of physiological concentration[27] undergo a complex 3D morphogenetic program that results in vessel-like structures radiating from the microcarrier bead when co-cultured with a variety of stromal cells[16,18,28]. Here we demonstrate that normal human dermal fibroblasts (DFs), a clinically relevant and potentially autologous cell source, similarly support angiogenic outgrowth of ECs from microcarrier beads. DFs were either embedded or overlaid on the fibrin matrix to better elucidate the relative contributions of DFs versus EC tubules on the micro- and macro-rheological properties of the gel. Cartoon schematics of these two culture models are shown (**Figure 3.1A**), along with representative images of the typical morphogenetic progression for both culture models (**Figure 3.1B**). (Day 1 images reveal approximately comparable levels of EC confluence on the Cytodex beads achieved via the methods described.) Quantification of these types of images over a 14-day time course reveals an increase in the total length of the vessel-like networks for both conditions, with aggregate data from all beads across each independent experiment shown to illustrate the spread in the observed biological response (**Figure 3.1C**). The average total network lengths for the embedded culture model were consistently higher than the overlay model after day 1, but this increase was not statistically significant. Additionally, inclusion of AMR beads did not affect the rate of network formation (Supp. Figure 3.4). Over the duration of the culture period, the average network length per bead scaled across multiple orders of magnitude with the variance scaling accordingly. Data were log transformed and analyzed with a general linear model. The resulting model is: Log(Network Length) = 3.776*Log(Day). The single regression parameter is highly significant with $p < 0.0001$ and the model has an R^2 value of 0.988, demonstrating that vessel growth was exponential in time.

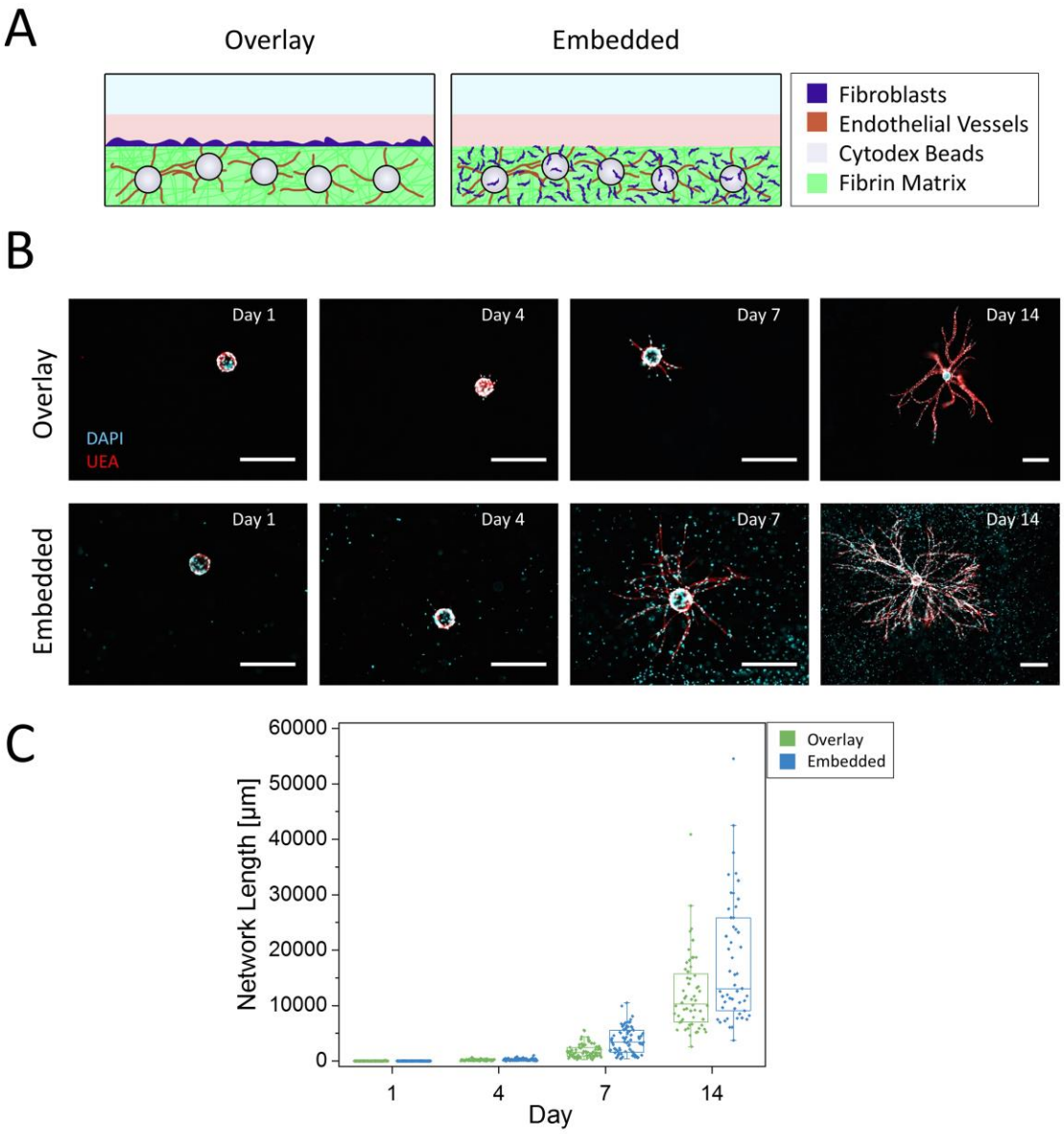

***Figure 3.1**: **DFs induce EC branching morphogenesis when overlaid or embedded within 3D fibrin matrices**. **A)** Schematic representation of the capillary morphogenesis assay. The "Overlay" condition involves culturing DFs on top of the fibrin gel, while the DFs are distributed throughout the fibrin gel in the "Embedded" condition. **B)** Representative images from each condition over a 14 day time course. UEA and DAPI staining indicate ECs and total cell nuclei, respectively. Scale bar = 500 µm. **C)** Quantified network lengths vs. time for both Overlay and Embedded conditions (8-40 beads assessed per replicate, N=3 per condition, per time point). A general linear model resulted in Log(Network Length) = 3.776*Log(Day), $p < 0.0001$, $R^2 = 0.988$. Boxed regions show median and interquartile range (IQR) of aggregate data, whiskers show range within 1.5 IQR.*

3.4.2 Acellular fibrin gels are mechanically stable over 14 days as assessed by macro-rheology and AMR

To characterize the bulk rheological properties of both acellular (pre-swollen) and cell-seeded fibrin constructs, we devised a new method described in the *Supplemental Materials and Methods.* Cartoon schematics illustrating the relative scale of bulk rheology compared to AMR are presented in **Figure 3.2A** to illustrate the large difference in resolution between the two techniques. Bulk rheology showed acellular fibrin gels are mechanically stable, maintaining a nearly constant (time-invariant) G' of 119 ± 19 Pa (mean + st. dev. from all trials and days) over the course of the culture period. Moreover, the inclusion of Cytodex (**Figure 3.2B**) and/or AMR beads (**Supp. Figure 3.5**) did not influence the bulk properties of the gel. Additionally, agreement between G' measurements of gels cast in multiple well sizes illustrates the validity of the method developed, independent of gel size (Error! Reference source not found.). Moving forward, we have used G' (the elastic component of the shear modulus) interchangeably with the more colloquial term "stiffness."

AMR measurements of acellular fibrin gels, both with and without Cytodex beads, exhibited notable stiffness heterogeneity spanning nearly two orders of magnitude (**Figure 3.2C**); min value of 8 Pa, max value of 933 Pa across all conditions and time points shown on the graph). Repeatedly, the mean stiffness of these cell-free systems was slightly higher at Day 1, as compared to Days 4, 7, and 14 ($p<0.05$, for both +/- Cytodex beads). However, comparisons of local G' values across the later time points were not statistically different from one another, illustrating the mechanical stability of these acellular fibrin gels at the microscale consistent with bulk rheology. Furthermore, the presence of the Cytodex beads did not appreciably affect the distribution of local stiffness, as demonstrated by plotting G' values at increasing distance from the Cytodex beads (**Figure 3.2D**). Additionally, confocal reflection images near Cytodex beads were indistinguishable from gels

without cytodex beads, illustrating that Cytodex beads do not disrupt the fibrillar architecture (**Figure 3.2E, F**).

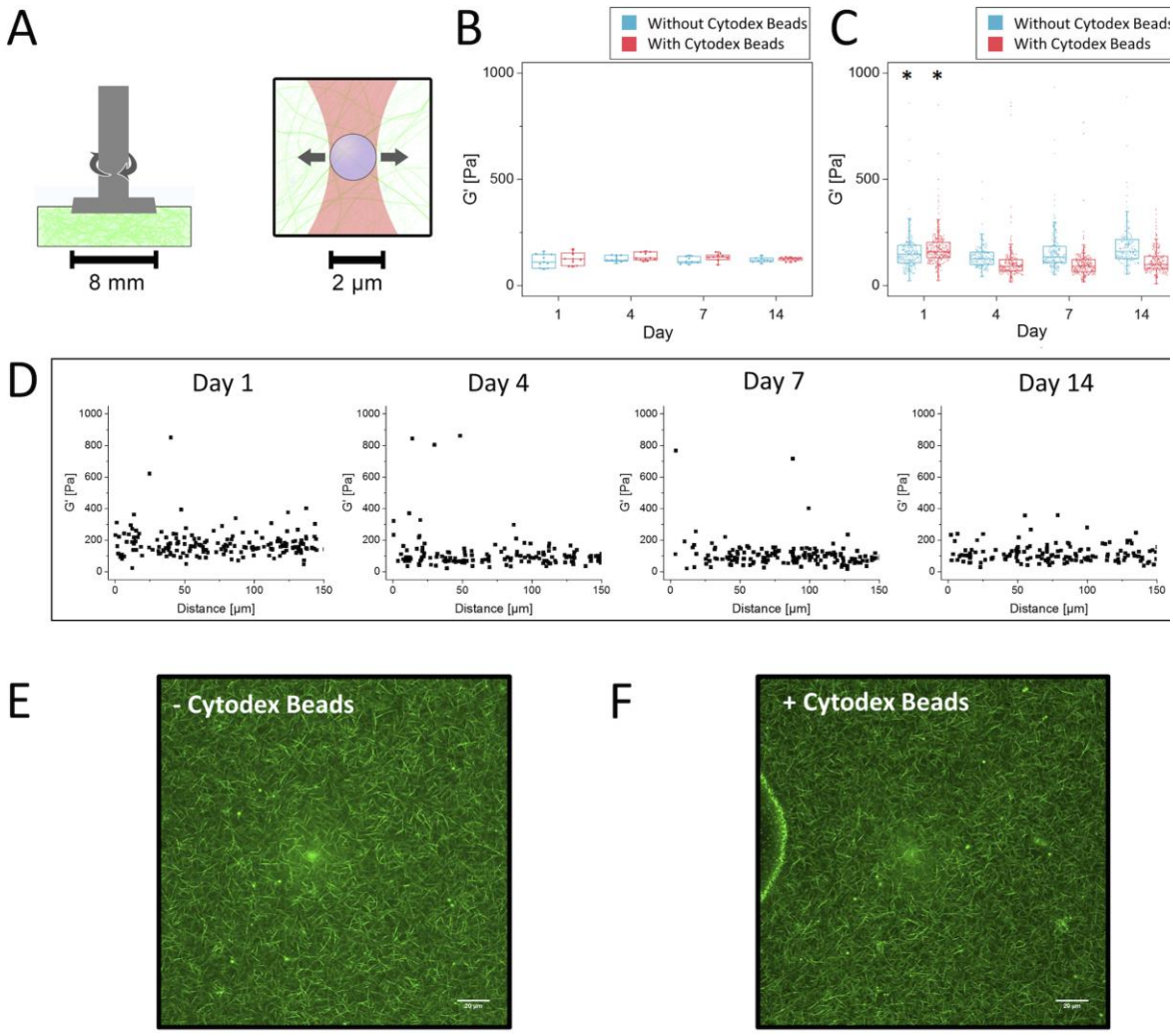

Figure 3.2: Bulk rheology and AMR of acellular fibrin gels reveal the gels are mechanically stable over 2 weeks in culture conditions. ***A)*** *Schematic diagram of methods used to quantify stiffness in bulk using parallel plate rheology (left) and at the microscale using active microrheology (right).* ***B)*** *Bulk rheology over 14 days with (red) and without (blue) Cytodex beads. (N=3, per condition, per timepoint). One-way ANOVA of G' +/- Cytodex beads yielded a P value of 0.93.* ***C)*** *Microrheology over 14 days with and without Cytodex beads (aggregate data, N=3 independent samples, with* $n_{AMRbeads}$*>150 per time point, per condition). Boxed regions in panels B and C show median and interquartile range (IQR) of aggregate data, whiskers show range within 1.5 IQR. The asterisk above Day 1 indicates significant differences (p<0.05) relative to all other time points for both conditions (+/- Cytodex beads).* ***D)*** *Microrheology data from* ***(C)*** *plotted as a function of distance from the edge of the Cytodex bead.* ***E,F)*** *Confocal reflection of the fibrin meshwork without and with Cytodex beads (Scale bar = 20 µm).*

3.4.3 Bulk rheology reveals tissue constructs stiffen over time during morphogenesis

Fibrin gels with DFs either overlaid or embedded demonstrated significant stiffening over time, with overlay conditions stiffening more rapidly than embedded conditions (**Figure 3.3A**). Controls in which DFs were included but Cytodex microcarrier beads were not coated with ECs demonstrate similar bulk stiffening behavior over time (**Figure 3.3B**). Scaffolds with DFs embedded stiffened ~2-fold to a final G' of 253 ± 27 Pa, while scaffolds with DFs overlaid stiffened ~3.3-fold to a final G' of ~394 ± 43 Pa over the course of 2 weeks. Heteroscedastic 2-tail t-tests were used to verify no significant differences occurred between G' measured for any given culture model and day compared to its respective *DF Only* control (**Figure 3.3A, B**). In addition, experiments in which DFs were cultured on Transwell inserts, and then removed for gel rheological measurements, showed that construct mechanical properties did not change significantly over a 14-day time course in the absence of DFs, even when ECs were included in the culture and tubulogenesis occurred (**Figure 3.3C**). Lack of contact of the DFs with the fibrin construct via the Transwell did not adversely affect capillary sprouting, as revealed by the equivalent total network lengths (**Figure 3.3D**). Together, these data demonstrate that DFs dominate the bulk stiffening of the scaffolds, while the ECs undergoing morphogenesis did not significantly affect the bulk mechanical properties of the constructs in this assay.

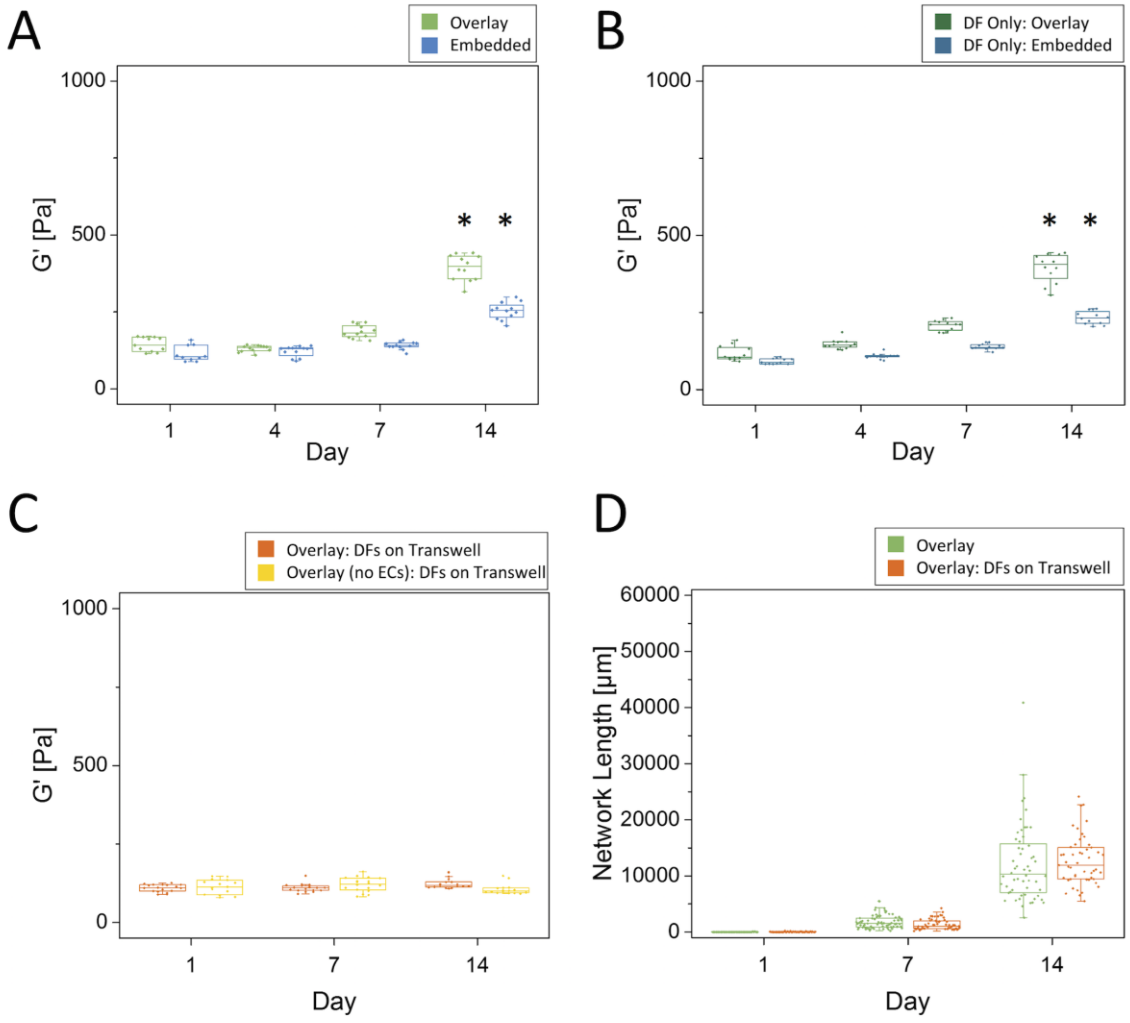

Figure 3.3: Bulk rheology reveals an increase in stiffness with time during morphogenesis. *Parallel plate rheology of* ***(A)*** *bead assay in both the Overlay and Embedded conditions,* ***(B)*** *fibrin constructs with only DFs (no ECs) either overlaid on top of the gel or embedded within, and* ***(C)*** *a bead assay and a fibrin construct with DFs located on a Transwell (N=3 independent experiments for each time point and condition). Asterisks in* ***(A)*** *and* ***(B)*** *indicate statistical differences from all other time points for a given assay type ($p<0.05$).* ***D)*** *Quantified network lengths between the Overlay condition and Overlay with DFs on a Transwell (multiple ROIs assessed per sample, N=3, per condition, per time point). There were no statistical differences between Transwell and Overlay conditions for any given day. Boxed regions show median and interquartile range (IQR) of aggregate data, whiskers show range within 1.5 IQR.*

3.4.4 Capillary morphogenesis is accompanied by dynamic spatiotemporal changes in local ECM stiffness and organization

Results from selected AMR measurements for both overlay and embedded conditions proximal to the endothelial sprouts show that ECM micro-stiffness changed considerably in both space and time during capillary sprouting (**Figure 3.4A**, **B, phase**). In some cases, AMR beads in close proximity reported G' values that differed by as much as 5-10x within only a few microns in the same ECM (**Figure 3.4**, **arrows**). Matched maximum intensity confocal reflection z-projections (**Figure 3.4A, B, confocal reflection**) demonstrated how the ECM was simultaneously remodeled. At early time points (Days 1 and 4), a typical fibrin mesh was detected proximal to the ECs. Stepping through assembled z-stacks revealed a distinct high contrast fibrillar architecture surrounding Cytodex beads on Day 1 for both the overlay (**Supp. Figure 3.6**) and embedded (**Supp. Figure 3.7**) culture models; this architecture is a hallmark signature of fibrin's microstructure. In the embedded model, however, the ECM was already changing spatially around the embedded fibroblasts. By Day 14, this fibrillar meshwork was replaced with a diffuse signal indicative of remodeling by the cells at later time points (Days 7 and 14). The fibrous structure was difficult to resolve near capillaries in the overlay conditions (**Supp. Figure 3.8**), and throughout the dish for embedded cultures (**Supp. Figure 3.9**). Interestingly, changes in pericellular ECM architecture over time did not necessarily correlate with regions of elevated stiffness as measured by AMR in the same locations. This was particularly evident in the Day 7 overlay condition, where punctate stiff areas are found both in and out of the remodeled area, though generally appears elevated near sprouts.

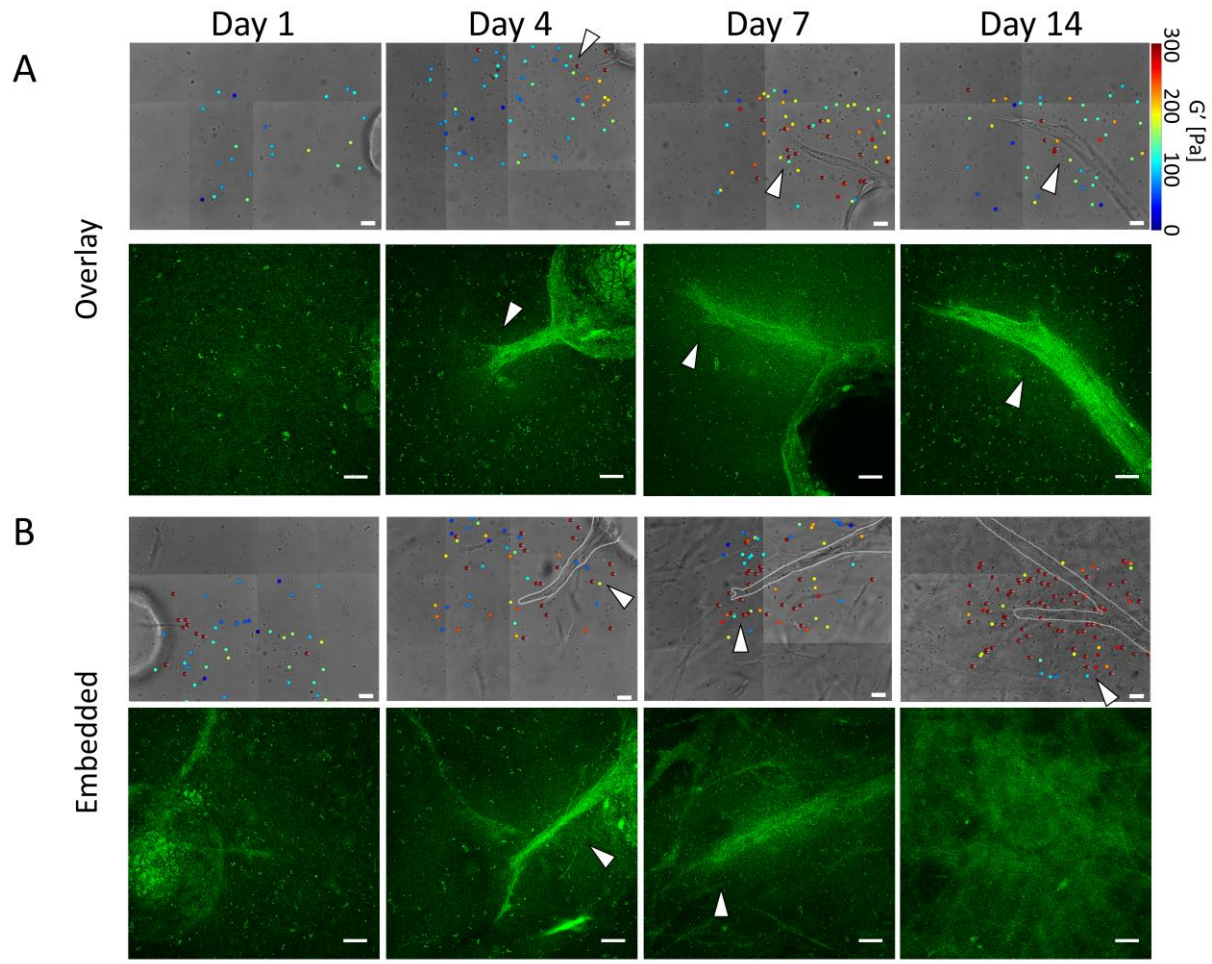

***Figure 3.4**: **Capillary morphogenesis is accompanied by dynamic spatiotemporal changes in local ECM stiffness and organization**. Selected stiffness maps generated using AMR and corresponding confocal reflection maximum intensity z-projections for the **(A)** Overlay and **(B)** Embedded conditions. Z-projections were created from 60 µm z-stacks with a step size of 1 µm, with those planes affected by distortion from the cover glass trimmed out prior to z-projection. Scale bar = 20 µm for brightfield images and 20 µm for reflection confocal z-projections. Arrows added emphasize areas where there is close proximity of stiffness heterogeneity, especially in the context of areas that appear different from the fibrous structure of fibrin. Please note the color map for G' saturates at 300 Pa. Stiffness values for individual beads reporting stiffness above 300 Pa are annotated on the beads.*

3.4.5 AMR quantitatively reveals significant local ECM stiffness heterogeneities during capillary morphogenesis

AMR measurements were conducted for both the overlay and embedded conditions in triplicate, and the results are shown in aggregate (**Figure 3.5A)**. Generally, there was an increase in average micro-stiffness over time. As early as Day 1, the embedded condition showed a broader range of G' values as compared to the overlay condition, with both conditions showing an orders-

of-magnitude distribution. Within the embedded condition, this heterogeneity was observed as early as Day 1. Consistent with acellular gels (**Figure 3.2C**), average local stiffness in the overlay condition decreased slightly between Days 1 and 4 ($p<0.05$), and by Day 14 was similar on average to the embedded condition. To assess the effects of DFs on the peri-endothelial stiffness, AMR was conducted in fibrin gels containing only fibroblasts in both the

overlay and embedded conditions (**Figure 3.5B**). In the embedded case, the effects of fibroblast remodeling were evident (increasing *G'*) by Day 7, whereas in the overlay case, no such effect was observed. In fact, overlay gels softened at Day 14 ($p<0.05$, compared to all other days), an effect not observed with bulk rheology (**Figure 3.3B**).

To further analyze the spatial distribution of stiffness observed in both the overlay and embedded conditions, AMR measurements were classified as either near or far, based on the proximity of each probe particle (<50μm or >50μm, respectively) to the nearest endothelial tubule (**Figure 3.5C**). Within these conditions, *G' near* is significantly greater than *G' far* at all time points, except for Day 1 of the embedded case (Mann-Whitney Test, $p<0.05$). This indicates that the effects of endothelial vessel stiffening of the ECM are concentrated proximal to the vessel, with the effect dissipating with distance. Plots of *G'* as a function of probe bead proximity to the ECs (**Figure 3.5D**) show that in the overlay case stiffening is concentrated in a region approximately within 50 μm of the ECs and increases over time. In contrast, the stiffness topography is more heterogeneous at all time points in the embedded case.

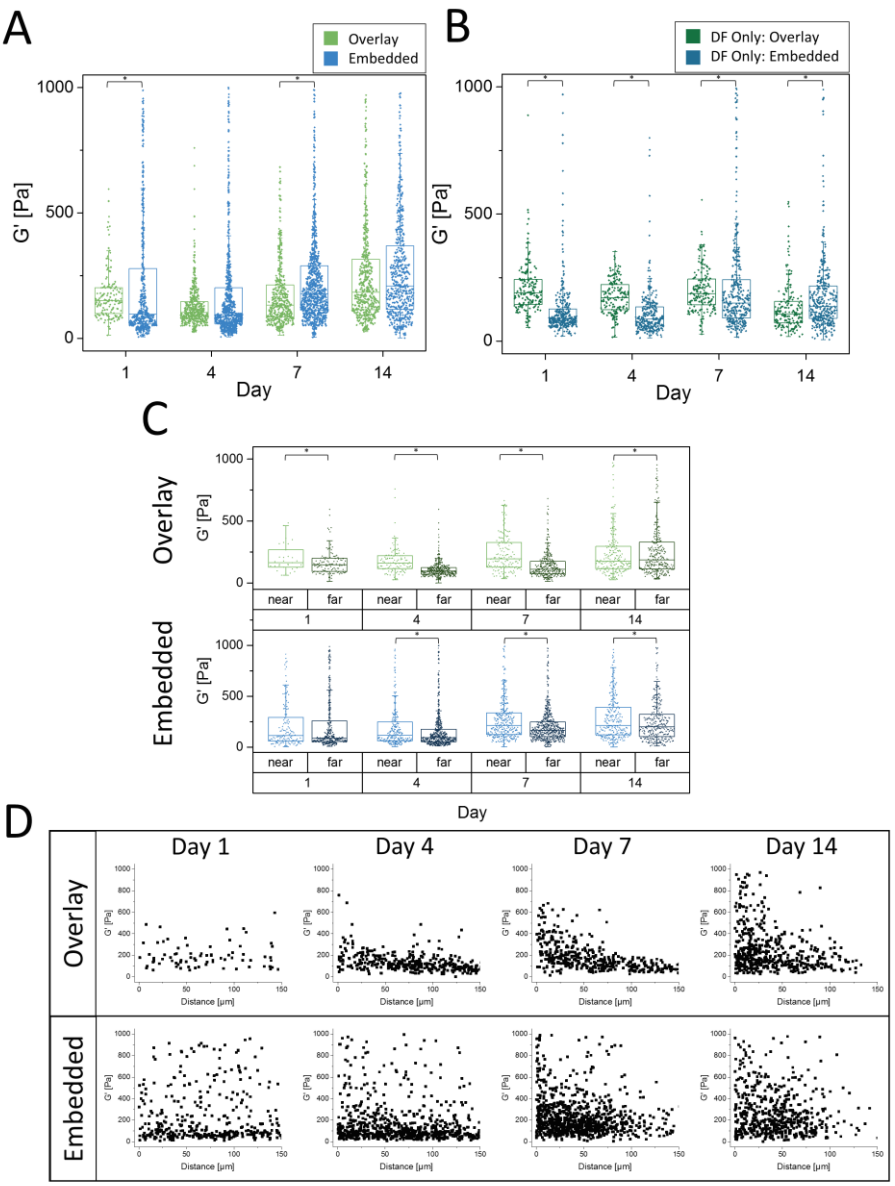

***Figure 3.5**: **AMR quantitatively reveals significant local ECM stiffness heterogeneities during capillary morphogenesis**. **A)** Microrheology proximal to the sprout tips in both the Overlay and Embedded conditions (aggregate data, N=3 per condition, per timepoint). **B)** Microrheology in fibrin constructs only containing DFs (no ECs) either overlaid on top of the gel or embedded within (aggregate data, N=3 independent samples, with $n_{AMRbeads}$>150 per time point, per condition). **C)** Microrheology from (**A**) segregated into two classes, near or far, based on distance from endothelial cells (<50 µm or >50 µm, respectively). For panels A-C, asterisks indicate statistical differences between groups ($p<0.05$) Boxed regions show median and interquartile range (IQR) of aggregate data, whiskers show range within 1.5 IQR. **D)** Microrheology data from (A) plotted as a function of probe bead proximity to the ECs.*

3.5 DISCUSSION

Branching morphogenesis is a complex phenomenon that occurs throughout the life of all metazoan organisms[29], and there is strong evidence that ECM mechanics and cell-generated forces play important roles in shaping the organization (and disorganization) of both normal and diseased tissues[30,31]. Studies using biomimetic materials have shown that matrix stiffness regulates cell fate in 2D[7] and 3D[9]. More recent studies have shown the ECM's mechanical regulation of cell behavior goes well beyond initial bulk material properties (e.g., compressive, tensile, shear moduli), with strong evidence that stress relaxation[32], fibrillar architectures[33], mechanical patterns/gradients[34,35], and dynamic changes in mechanical properties[36–38] all play significant roles. To better understand the mechanical influence of a natural ECM on a complex morphogenetic process in 3D, we applied a laser tweezers-based active microrheology method and traditional parallel plate shear macrorheology to a well-established and biologically relevant 3D fibrin-based co-culture model of capillary morphogenesis, and tracked the spatiotemporal evolution of the micro- and macro-scale shear elastic modulus during the formation of an extensive microvascular network.

AMR revealed mechanical micro-heterogeneities within acellular fibrin-based matrices, with G' values spanning an order of magnitude within each gel. This microscale heterogeneity increased in the presence of cells and with time in culture, coincident with an overall increase in the bulk G' values of the tissue constructs. Experiments to dissect the cellular origins of this increased stiffness revealed that the supportive DFs largely accounted for the observed increases in the bulk mechanical properties of the ECM, as DF monocultures lacking ECs also increased their bulk mechanical properties with time in culture. Additional experiments in which DFs were cultured on a Transwell insert placed on top of the gel revealed that the bulk mechanical properties of gels not in physical contact with DFs did not increase. Equivalent EC sprouting occurred when DFs

were in direct contact with the gel or on a Transwell. Because we have previously shown that sprouting is deficient in the presence of fibroblast-conditioned media[13], these experiments show that reciprocal cross-talk between ECs and DFs necessary for morphogenesis still occurs when the latter are cultured on Transwells.

While the bulk mechanical property changes were largely attributable to the DFs, AMR revealed that ECs undergoing sprouting angiogenesis also progressively stiffened the ECM as they invaded. Significant increases in the micro-stiffness of the ECM occurred within 50 μm ("near") of the sprouting vessel-like structures, regardless of whether DFs were overlaid or embedded in the matrix. The AMR experiments in the overlay conditions were particularly indicative of the EC-induced local stiffening because the DFs were located on top of the gel a fixed distance away from the z-plane (> 500 μm) in which the EC-coated beads tend to settle and in which our AMR measurements were taken. The increased heterogeneity of G' values with time in the "near" region proximal to the vessel-like structures in the overlay conditions was also likely due to ECs. ECs apply traction forces[12,14] and deposit new matrix[39] during capillary morphogenesis, both of which would be expected to locally stiffen the ECM.

In addition to our AMR measurements, we observed changes in ECM architecture during morphogenesis via confocal reflection microscopy. Previous studies have shown that EC tubules invading a fibrous collagen ECM deposit new collagen matrix (appearing specular as opposed to fibrillar) proximal to the lumen as EC tubules grow[39]. The ECM's appearance proximal to vessels in our culture models (Error! Reference source not found.**,**Error! Reference source not found.**)** was consistent with these previous findings. What has not been clear is how such changes affect local stiffness over time. Our AMR results show that local stiffness heterogeneity increased over time in culture, an effect localized to EC tubules in the overlay culture, but ubiquitous in the embedded

cultures that contain an increasing population of DFs. In some cases, stiffness distal to EC tubules and located in fibrous ECM increased to values similar to those found proximal to EC tubules in specular ECM. Furthermore, this distal effect was limited in extent for the overlay conditions; beyond ~50 μm from the tubule surface, stiffness values were similar to those measured by bulk rheology and AMR of acellular gels. Therefore, areas of obvious matrix remodeling did not necessarily coincide with regions of elevated stiffness or even the greatest stiffness heterogeneities. This observation casts important limitations on methods that correlate mechanical properties with fiber architecture[40] or rely on quantification of fiber deformations[41].

In the context of vascular morphogenesis, inconsistencies regarding the roles of ECM mechanics remain in the literature. Early evidence demonstrated that mechanical cues directly impact tubulogenesis, with softer gels better able to support capillary morphogenesis in 2D[42,43]. In 3D cultures, angiogenic process extension was attenuated in fibrin gels whose mechanical properties were manipulated by adding exogenous factor XIII to form additional cross-links[44]. We previously demonstrated that increasing fibrin's bulk mechanical properties by increasing fibrinogen concentration beyond the physiologic provisional clot concentration used here (~2.5 mg/mL)[27] results in significant reductions in angiogenic sprouting not only *in vitro*[15] but also *in vivo*[45]; however, sub-physiologic concentrations yield overly soft gels that slowed angiogenic invasion due to reduced resistance to cell-generated traction forces[14]. Efforts to decouple ECM stiffness from other cues using glycated collagen matrices have demonstrated that stiffer ECM promotes increased angiogenic outgrowth, invasion, and branching, independent of changes in matrix density[46,47]. Similarly, angiogenic invasion of ECs was increased in collagen gels cross-linked with transglutaminase to increase the stiffness without affecting the concentration[48].

However, other studies have reported that increased stiffness induced by collagen glycation attenuates vessel morphogenesis[49,50].

Because of the limitations of natural ECMs and the inconsistencies in the literature, we (and many others) have turned to synthetic material platforms in an effort to decouple the mechanical and chemical effects of the ECM and thereby differentiate the contributions of mechanical cues in isolation. In such systems, softer, less cross-linked gels susceptible to cell-secreted proteases were better able to support the formation of vessel-like networks *in vitro*[51,52]; the identity of the degradable peptides was a bigger influence than the starting mechanical properties of the gels on the formation of functional microvasculature *in vivo*[52]. However, engineered hydrogels lack key features of native ECM, which is typically fibrillar, macroporous, heterogeneous, mechanically anisotropic, and is actively remodeled by the cells that reside within it. The amorphous nature and mechanical homogeneity of synthetic gels are essential for their utility in 3D traction force microscopy[53], but questions remain regarding their physiological relevance for addressing mechanistic questions.

Our findings underscore the importance of characterizing across length scales when deciphering the roles of ECM mechanics on morphogenesis in 3D. Bulk rheology was useful for establishing ensemble averaged mechanical properties and quantifying the large degrees of stromal cell-mediated matrix remodeling with a relatively accessible technique. Understanding bulk properties is important for handling of tissue constructs and regenerative medicine applications. By contrast, AMR was useful for the precise spatiotemporal quantification of ECM mechanics on subcellular length scales during 3D capillary morphogenesis in soft fibrin matrices. Similar AMR measurements have also revealed enormous heterogeneity in the micromechanical properties of type-I collagen gels[54]. Interestingly, in these collagen gels, local cell-mediated stiffening requires

both myosin-mediated traction forces[54] and active proteolysis via MMPs[55][55]. Future work will address if the wide spatiotemporal variations in ECM stiffness observed during capillary growth and invasion in soft fibrin gels translate to other natural materials (of different concentrations), and if they directly influence phenotypic bifurcations (i.e., cell fate decisions), including the induction of vessel branching or the guidance of vascular invasion.

3.6 ACKNOWLEDGMENTS

Research reported in this publication was supported by the National Heart, Lung, and Blood Institute of the National Institutes of Health under Award Number R01-HL085339. The content is solely the responsibility of the authors and does not necessarily represent the official views of the National Institutes of Health. BAJ was partially supported by the Tissue Engineering and Regeneration Training Program at the University of Michigan (T32-DE007057).

3.7 SUPPLEMENTAL MATERIAL

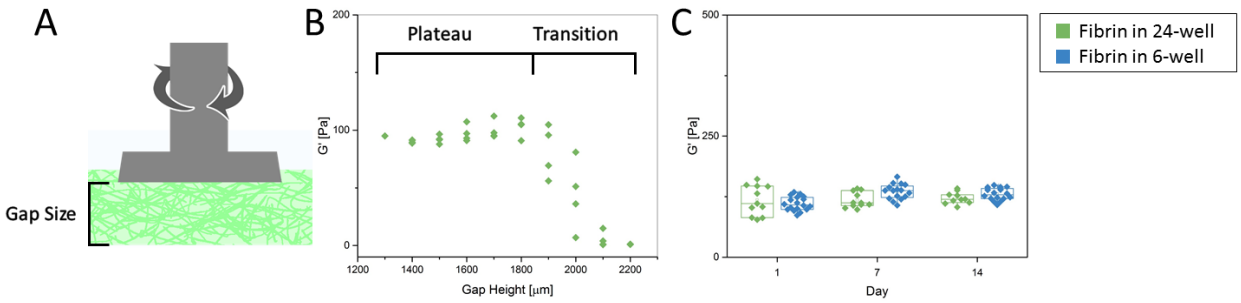

***Supp. Figure 3.1**: **Acellular fibrin gels in culture plates reach consistent plateau value for G' and are consistent across well sizes. A)** Schematic illustrating gap height from bottom of sample to measurement head. **B)** Shear modulus as a function of gap height is shown as the rheometer measurement head was progressively lowered onto acellular fibrin gels cast in 24-well plates. A plateau value of ~110 Pa was quickly reached after the measurement head made contact with the gels and was consistent over hundreds of microns before gradually decreasing. (Aggregate data shown, N=4) **C)** Shear modulus is consistent between 24-well (2.5 cm^2) and 6-well (9.8 cm^2) plates across time. One-way ANOVA resulted in p = 0.60 between all conditions and time points. (Aggregate data shown, N=3, per condition, per time point)*

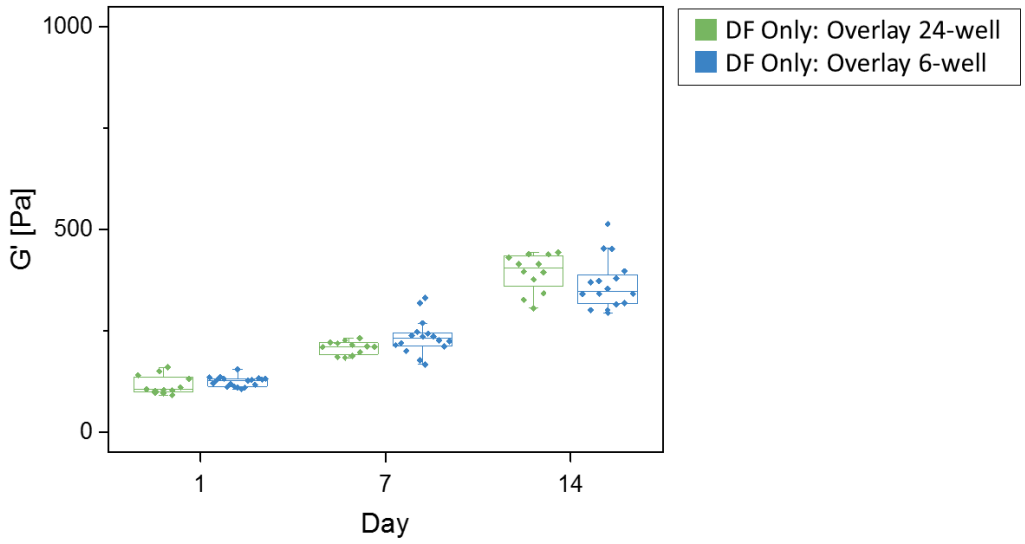

Supp. Figure 3.2: ***Culture well size does not influence stiffening behavior of overlay conditions.*** *Bulk G' on days 1, 7, and 14 was unaffected by the size of well in which cells were cultured, as assessed with t-tests between matching conditions. (Aggregate data shown, N=3 for all conditions)*

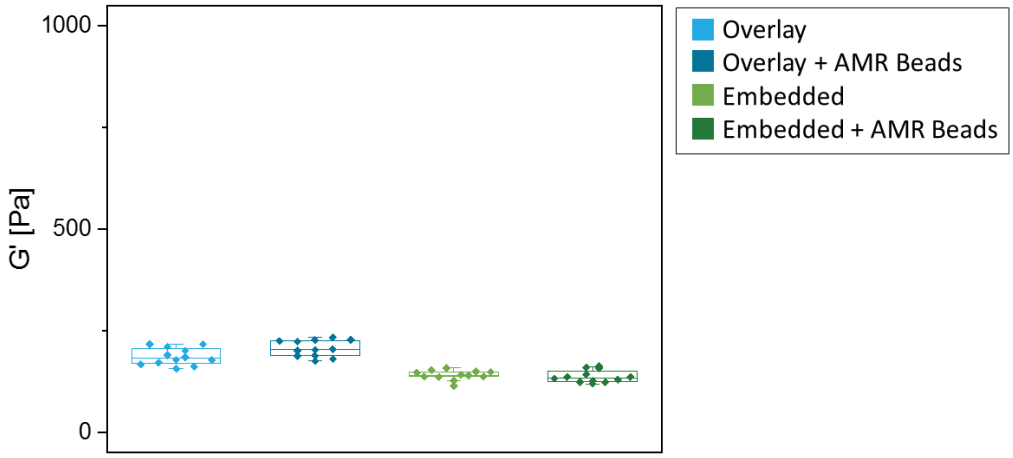

Supp. Figure 3.3: ***Inclusion of AMR beads does not influence bulk G' of cell cultures on Day 7.*** *Bulk G' was unaffected by the inclusion of AMR beads for either co-culture model, as assessed with t-tests between matching conditions. (Aggregate data shown, N=3 for all conditions)*

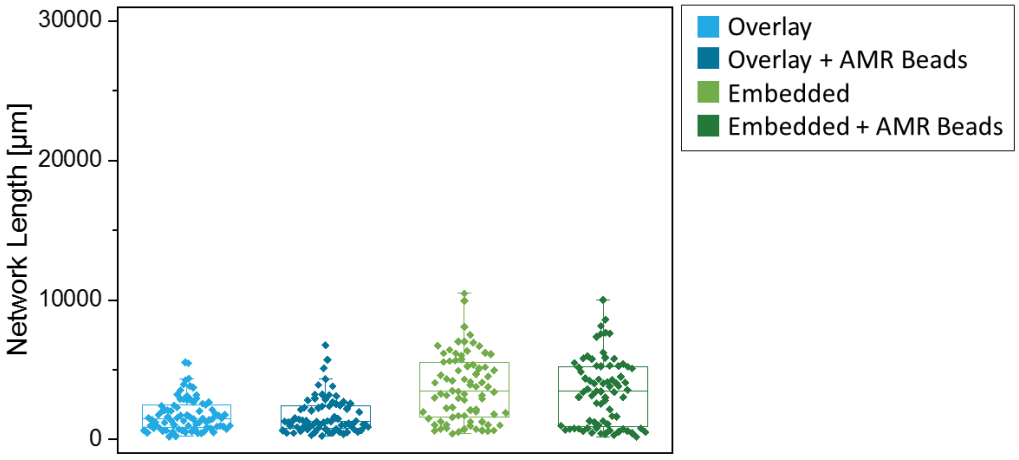

Supp. Figure 3.4: ***Inclusion of AMR beads does not influence capillary network formation at Day 7.*** *Average network lengths were unaffected by the inclusion of AMR beads for either co-culture model, as assessed with t-tests between matching conditions. (Aggregate data shown, N=3 for all conditions)*

:

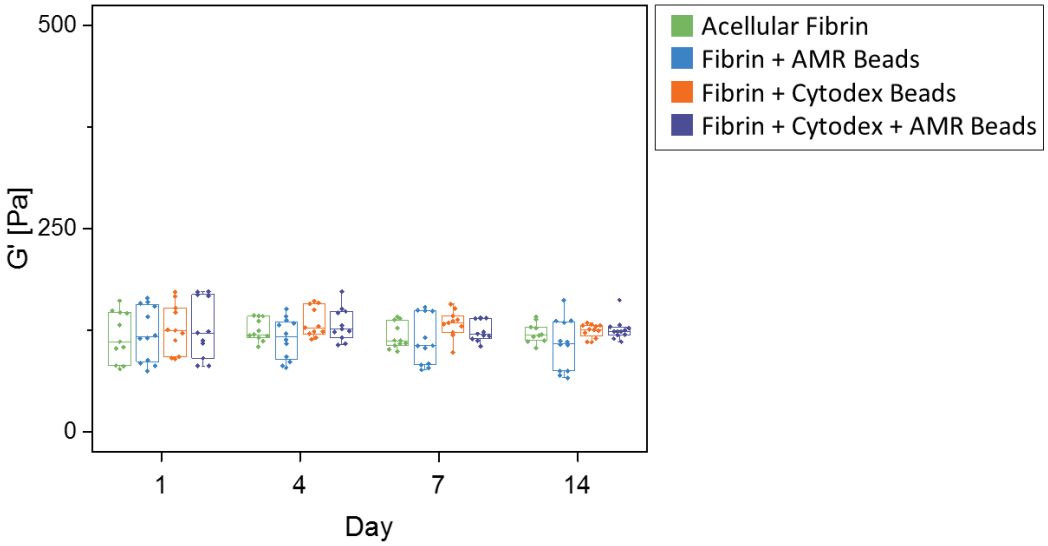

Supp. Figure 3.5: ***Inclusion of Cytodex and/or AMR beads does not influence the bulk properties of acellular gels over time.*** *No significant differences in bulk G' were observed between any condition across all time points. One-way ANOVA resulted in p = 0.91 between all conditions and time points. (Aggregate data shown, N=3, per condition, per time point)*

Supplemental Video Still Images and Captions

Note: Full videos available on the publishers website.

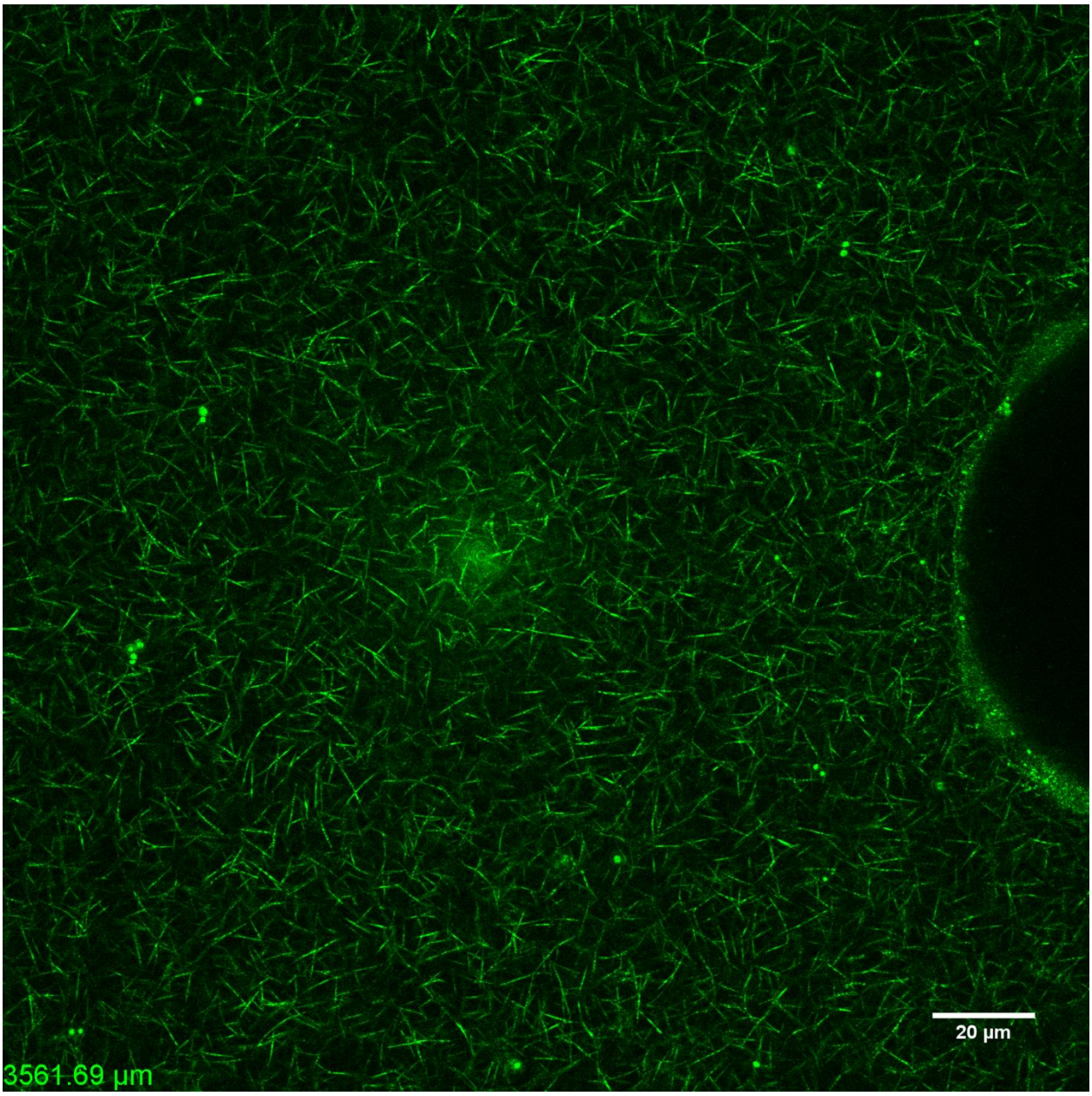

*Supp. Figure 3.6: Video**, Day 1 Overlay Condition - Reflection confocal z-stack***

EC-coated cytodex bead within fibrin matrix highlighting the structure of the fibrin matrix prior to sprouting when DFs are in the overlay configuration.

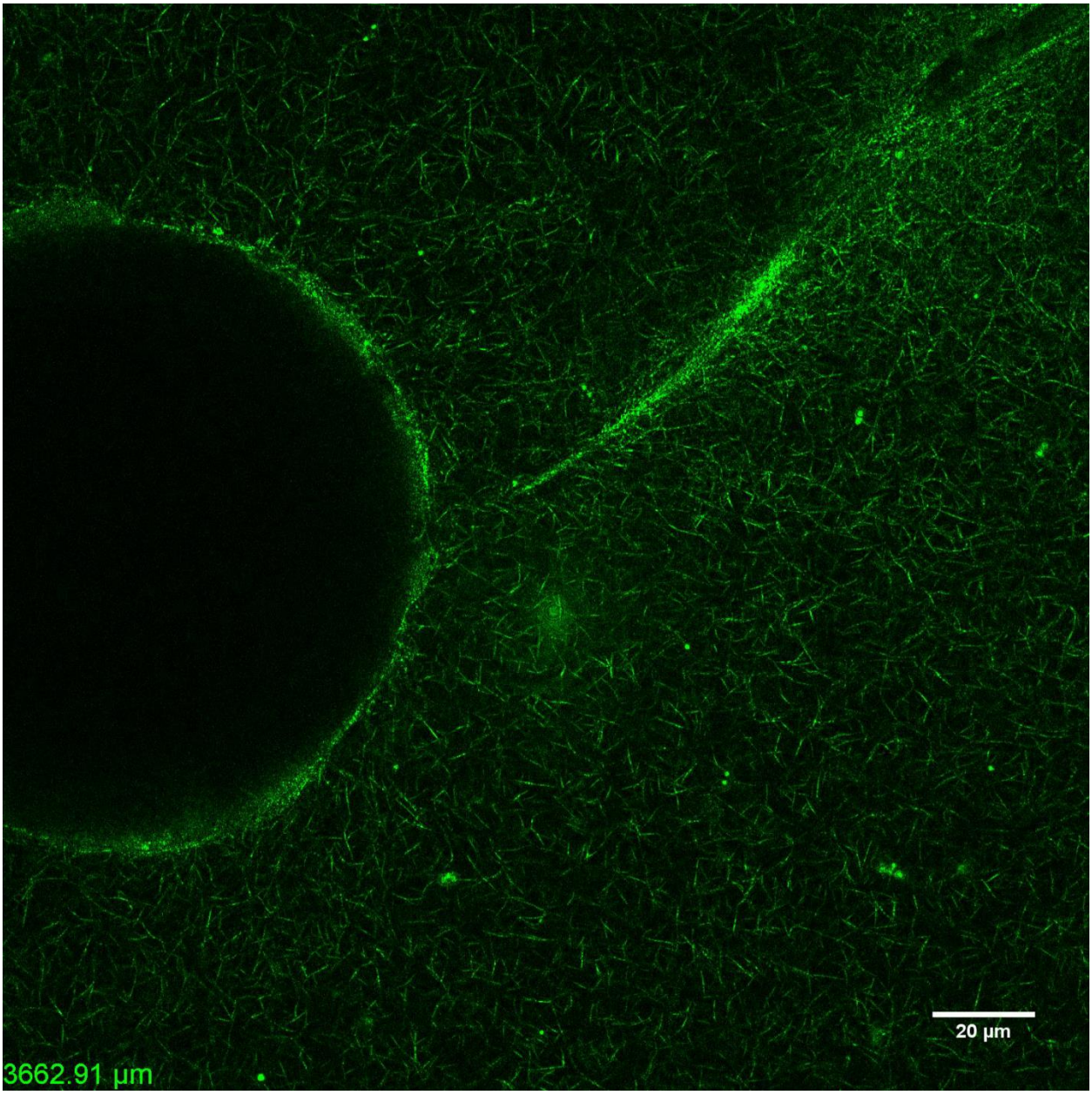

Supp. Figure 3.7: Video, ***Day 1 Embedded Condition - Reflection confocal z-stack***

EC-coated cytodex bead within fibrin matrix highlighting the structure of the fibrin matrix prior to sprouting when DFs are in the embedded configuration.

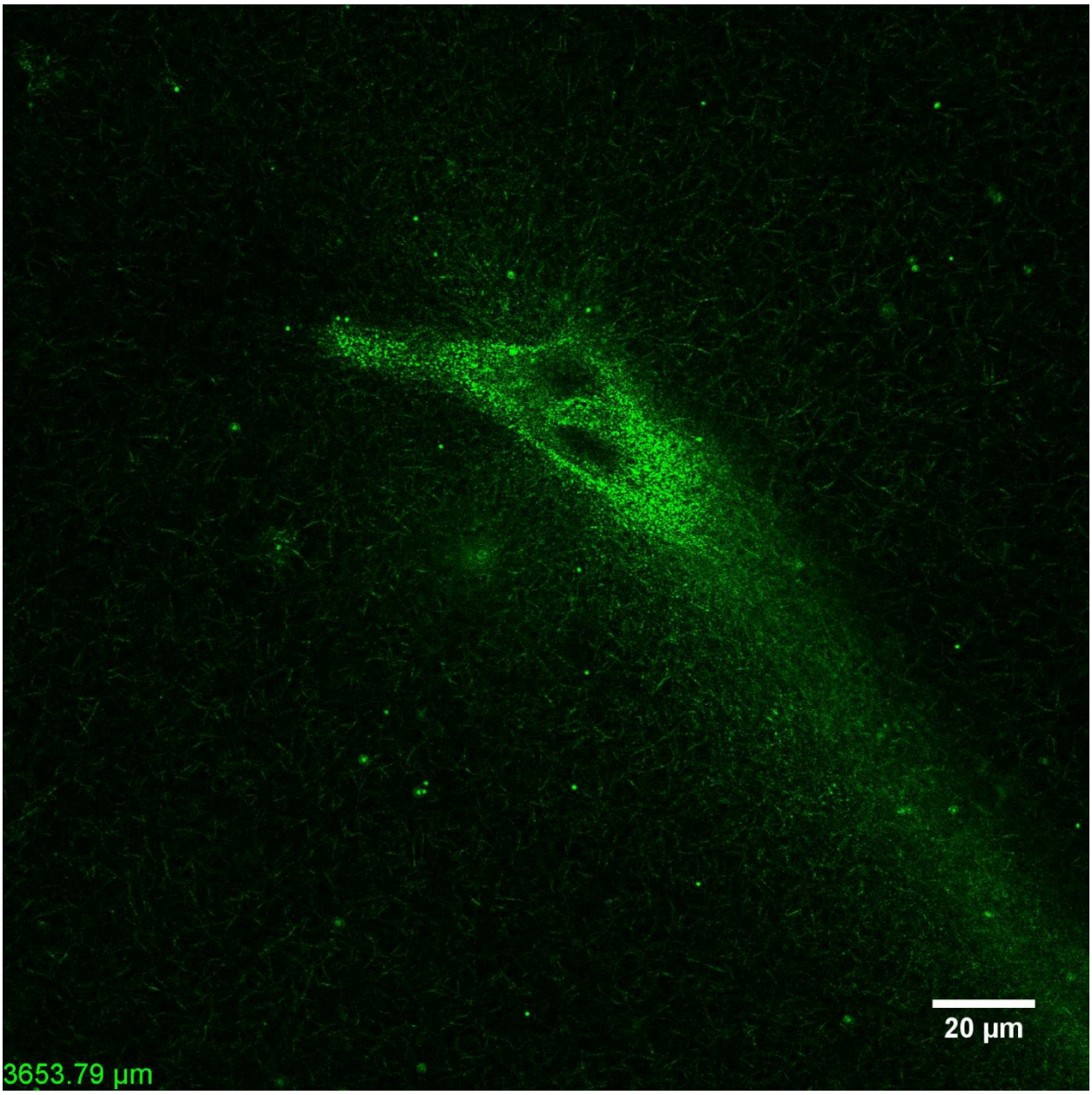

Supp. Figure 3.8: Video, ***Day 14 Overlay Condition - Reflection confocal z-stack***

EC sprout within fibrin matrix highlighting the structure of the fibrin matrix following 14 days of growth with DFS in the overlay configuration.

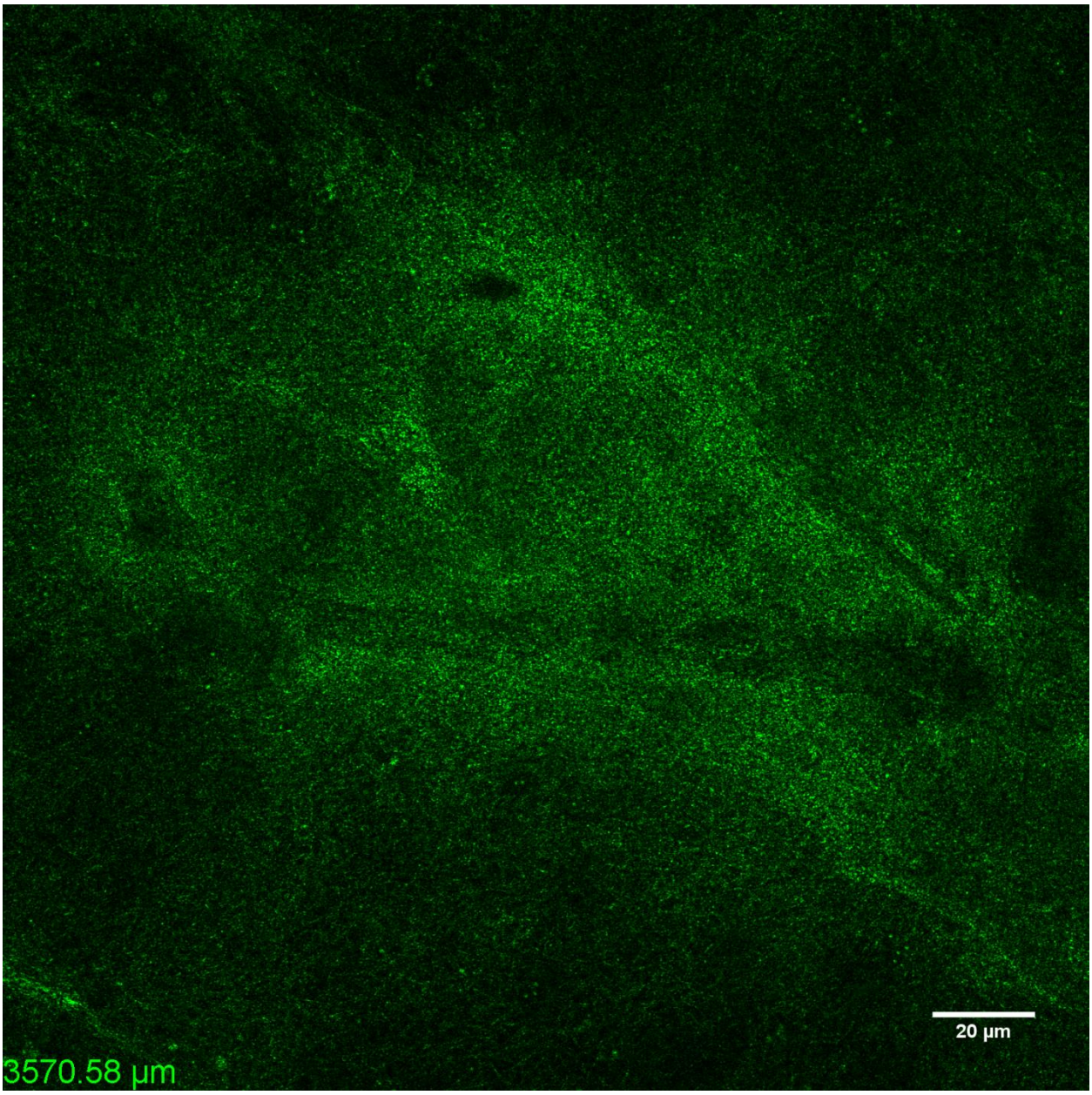

Supp. Figure 3.9: Video, ***Day 14 Embedded Condition - Reflection confocal z-stack***

EC sprout within fibrin matrix highlighting the structure of the fibrin matrix following 14 days of growth with DFS in the embedded configuration.

3.8 REFERENCES

1. Discher, D. E., Janmey, P. & Wang, Y.-L. Tissue cells feel and respond to the stiffness of their substrate. *Science* **310,** 1139–43 (2005).
2. Engler, A. *et al.* Substrate Compliance versus Ligand Density in Cell on Gel Responses. *Biophys. J.* **86,** 617–628 (2004).
3. Peyton, S. R. & Putnam, A. J. Extracellular matrix rigidity governs smooth muscle cell motility in a biphasic fashion. *J. Cell. Physiol.* **204,** 198–209 (2005).
4. Beamish, J. A., Chen, E. & Putnam, A. J. Engineered extracellular matrices with controlled mechanics modulate renal proximal tubular cell epithelialization. *PLoS One* **12,** 1–24 (2017).
5. Khatiwala, C. B., Peyton, S. R. & Putnam, A. J. Intrinsic mechanical properties of the extracellular matrix affect the behavior of pre-osteoblastic MC3T3-E1 cells. *Cell Physiol. - Am. J. Physiol.* **290,** C1640–C1650 (2006).
6. Lo, C. M., Wang, H. B., Dembo, M. & Wang, Y. L. Cell movement is guided by the rigidity of the substrate. *Biophys. J.* **79,** 144–152 (2000).
7. Engler, A. J., Sen, S., Sweeney, H. L. & Discher, D. E. Matrix Elasticity Directs Stem Cell Lineage Specification. *Cell* **126,** 677–689 (2006).
8. Khatiwala, C. B., Kim, P. D., Peyton, S. R. & Putnam, A. J. ECM compliance regulates osteogenesis by influencing MAPK signaling downstream of RhoA and ROCK. *J. Bone Miner. Res.* **24,** 886–898 (2009).
9. Huebsch, N. *et al.* Harnessing traction-mediated manipulation of the cell/matrix interface to control stem-cell fate. *Nat. Mater.* **9,** 518–26 (2010).
10. Peyton, S. R., Kim, P. D., Ghajar, C. M., Seliktar, D. & Putnam, A. J. The effects of matrix stiffness and RhoA on the phenotypic plasticity of smooth muscle cells in a 3-D biosynthetic hydrogel system. *Biomaterials* **29,** 2597–2607 (2008).
11. Ingber, D. E. Mechanical signaling and the cellular response to extracellular matrix in angiogenesis and cardiovascular physiology. *Circ. Res.* **91,** 877–887 (2002).
12. Korff, T. & Augustin, H. G. Tensional forces in fibrillar extracellular matrices control directional capillary sprouting. *J. Cell Sci.* **112 (Pt 1,** 3249–3258 (1999).
13. Kniazeva, E. & Putnam, A. J. Endothelial cell traction and ECM density influence both capillary morphogenesis and maintenance in 3-D. *Am. J. Physiol. Physiol.* **297,** C179–C187 (2009).
14. Kniazeva, E. *et al.* Quantification of local matrix deformations and mechanical properties during capillary morphogenesis in 3D. *Integr. Biol. (Camb).* **4,** 431–9 (2012).
15. Ghajar, C. M., Blevins, K. S., Hughes, C. C. W., George, S. C. & Putnam, A. J. Mesenchymal stem cells enhance angiogenesis in mechanically viable prevascularized tissues via early matrix metalloproteinase upregulation. *Tissue Eng.* **12,** 2875–2888 (2006).
16. Nehls, V. & Drenckhahn, D. A Novel, Microcarrier-Bead in Vitro Assay for Rapid and Reliable Quantification of Three-Dimensional Cell Migration and Angiogenesis. *Microvascular Research* **50,** 311–322 (1995).
17. Tonnesen, M. G., Feng, X. & Clark, R. A. F. Angiogenesis in wound healing. *J. Investig. Dermatology Symp. Proc.* **5,** 40–46 (2000).
18. Ghajar, C. M. *et al.* Mesenchymal cells stimulate capillary morphogenesis via distinct proteolytic mechanisms. *Exp. Cell Res.* **316,** 813–825 (2010).

19. Nakatsu, M. N. *et al.* Angiogenic sprouting and capillary lumen formation modeled by human umbilical vein endothelial cells (HUVEC) in fibrin gels: The role of fibroblasts and Angiopoietin-1. *Microvasc. Res.* **66,** 102–112 (2003).
20. Newman, A. C., Nakatsu, M. N., Chou, W., Gershon, P. D. & Hughes, C. C. W. The requirement for fibroblasts in angiogenesis: fibroblast-derived matrix proteins are essential for endothelial cell lumen formation. *Mol. Biol. Cell* **22,** 3791–3800 (2011).
21. Tomasek, J. J., Gabbiani, G., Hinz, B., Chaponnier, C. & Brown, R. a. Myofibroblasts and mechano-regulation of connective tissue remodelling. *Nat. Rev. Mol. Cell Biol.* **3,** 349–63 (2002).
22. Jansen, K. A., Bacabac, R. G., Piechocka, I. K. & Koenderink, G. H. Cells actively stiffen fibrin networks by generating contractile stress. *Biophys. J.* **105,** 2240–2251 (2013).
23. Ghajar, C. M. *et al.* The effect of matrix density on the regulation of 3-D capillary morphogenesis. *Biophys. J.* **94,** 1930–41 (2008).
24. Kotlarchyk, M. A. *et al.* Concentration independent modulation of local micromechanics in a fibrin gel. *PLoS One* **6,** (2011).
25. Brau, R. R. *et al.* Passive and active microrheology with optical tweezers. *J. Opt. A Pure Appl. Opt.* **9,** S103–S112 (2007).
26. Mizuno, D., Head, D. a., MacKintosh, F. C. & Schmidt, C. F. Active and Passive Microrheology in Equilibrium and Nonequilibrium Systems. *Macromolecules* **41,** 7194–7202 (2008).
27. Weisel, J. W. Enigmas of blood clot elasticity. *Science (80-.).* **320,** 456–457 (2008).
28. Kachgal, S. & Putnam, A. J. Mesenchymal stem cells from adipose and bone marrow promote angiogenesis via distinct cytokine and protease expression mechanisms. *Angiogenesis* **14,** 47–59 (2011).
29. Lu, P. & Werb, Z. Patterning mechanisms of branched organs. *Science (80-.).* **322,** 1506–1509 (2008).
30. Bellas, E. & Chen, C. S. Forms, forces, and stem cell fate. *Curr. Opin. Cell Biol.* **31,** 92–97 (2014).
31. Mammoto, T., Mammoto, A. & Ingber, D. E. Mechanobiology and Developmental Control. *Annu. Rev. Cell Dev. Biol.* **29,** 27–61 (2013).
32. Chaudhuri, O. *et al.* Hydrogels with tunable stress relaxation regulate stem cell fate and activity. *Nat. Mater.* **15,** 326–333 (2015).
33. Baker, B. M. *et al.* Cell-mediated fibre recruitment drives extracellular matrix mechanosensing in engineered fibrillar microenvironments. *Nat. Mater.* **14,** 1262–1268 (2015).
34. Tse, J. R. & Engler, A. J. Stiffness gradients mimicking in vivo tissue variation regulate mesenchymal stem cell fate. *PLoS One* **6,** (2011).
35. Yang, C. *et al.* Spatially patterned matrix elasticity directs stem cell fate. *Proc. Natl. Acad. Sci.* **113,** E4439–E4445 (2016).
36. Khetan, S. *et al.* Degradation-mediated cellular traction directs stem cell fate in covalently crosslinked three-dimensional hydrogels. *Nat. Mater.* **12,** 458–65 (2013).
37. Yang, C., Tibbitt, M. W., Basta, L. & Anseth, K. S. Mechanical memory and dosing influence stem cell fate. *Nat. Mater.* **13,** 645–652 (2014).
38. Lee, J., Abdeen, A. A. & Kilian, K. A. Rewiring mesenchymal stem cell lineage specification by switching the biophysical microenvironment. *Sci. Rep.* **4,** 5188 (2014).

39. Lee, P.-F., Yeh, A. T. & Bayless, K. J. Nonlinear optical microscopy reveals invading endothelial cells anisotropically alter three-dimensional collagen matrices. *Exp. Cell Res.* **315,** 396–410 (2009).
40. Raub, C. B. *et al.* Noninvasive assessment of collagen gel microstructure and mechanics using multiphoton microscopy. *Biophys. J.* **92,** 2212–2222 (2007).
41. Steinwachs, J. *et al.* Three-dimensional force microscopy of cells in biopolymer networks. *Nat. Methods* **advance on,** 171–176 (2016).
42. Vailhé, B., Lecomte, M., Wiernsperger, N. & Tranqui, L. The formation of tubular structures by endothelial cells is under the control of fibrinolysis and mechanical factors. *Angiogenesis* **2,** 331–344 (1998).
43. Deroanne, C. F., Lapiere, C. M. & Nusgens, B. V. In vitro tubulogenesis of endothelial cells by relaxation of the coupling extracellular matrix-cytoskeleton. **49,** 647–658 (2001).
44. Urech, L., Bittermann, A. G., Hubbell, J. A. & Hall, H. Mechanical properties, proteolytic degradability and biological modifications affect angiogenic process extension into native and modified fibrin matrices in vitro. *Biomaterials* **26,** 1369–1379 (2005).
45. Kniazeva, E., Kachgal, S. & Putnam, A. J. Effects of extracellular matrix density and mesenchymal stem cells on neovascularization in vivo. *Tissue Eng. Part A* **17,** 905–914 (2011).
46. Mason, B. N., Starchenko, A., Williams, R. M., Bonassar, L. J. & Reinhart-King, C. A. Tuning three-dimensional collagen matrix stiffness independently of collagen concentration modulates endothelial cell behavior. *Acta Biomater.* **9,** 4635–4644 (2013).
47. Bordeleau, F. *et al.* Matrix stiffening promotes a tumor vasculature phenotype. *Proc. Natl. Acad. Sci.* **114,** 492–497 (2017).
48. Lee, P. F., Bai, Y., Smith, R. L., Bayless, K. J. & Yeh, A. T. Angiogenic responses are enhanced in mechanically and microscopically characterized, microbial transglutaminase crosslinked collagen matrices with increased stiffness. *Acta Biomater.* **9,** 7178–7190 (2013).
49. Francis-Sedlak, M. E. *et al.* Collagen glycation alters neovascularization in vitro and in vivo. *Microvasc. Res.* **80,** 3–9 (2010).
50. Kuzuya, M. *et al.* Inhibition of angiogenesis on glycated collagen lattices. *Diabetologia* **41,** 491–499 (1998).
51. Singh, R. K., Seliktar, D. & Putnam, A. J. Capillary morphogenesis in PEG-collagen hydrogels. *Biomaterials* **34,** 9331–9340 (2013).
52. Vigen, M., Ceccarelli, J. & Putnam, A. J. Protease-sensitive PEG hydrogels regulate vascularization in vitro and in vivo. *Macromol. Biosci.* **14,** 1368–1379 (2014).
53. Legant, W. R. *et al.* Measurement of mechanical tractions exerted by cells in three-dimensional matrices. *Nat. Methods* **7,** 969–971 (2010).
54. Keating, M., Kurup, A., Alvarez-Elizondo, M., Levine, A. J. & Botvinick, E. Spatial distributions of pericellular stiffness in natural extracellular matrices are dependent on cell-mediated proteolysis and contractility. *Acta Biomater.* (2017). doi:10.1016/j.actbio.2017.05.008
55. Tang, Y. *et al.* MT1-MMP-Dependent Control of Skeletal Stem Cell Commitment via a β1-Integrin/YAP/TAZ Signaling Axis. *Dev. Cell* **25,** 402–416 (2013).

CHAPTER 4: SELECTIVE STIFFENING OF FIBRIN CONSTRUCTS WITH MICRON RESOLUTION VIA PHOTO-CROSSLINKING

Mark Keating[1], Micah Lim[1], Qingda Hu[1,2], Elliot Botvinick[1,2,3,*]

[1] Department of Biomedical Engineering, University of California, Irvine CA 92697-2730
[2] Center for Complex Biological Systems, University of California, Irvine, CA 92697-2280
[3] Department of Surgery, University of California, Irvine, CA 92697-2730
[*] To whom correspondence may addressed. Email: elliot.botvinick@uci.edu

Keywords: Microrheology; Stiffness; Tissue Mechanics; Extracellular Matrix; Hydrogel; Fibrin

4.1 ABSTRACT

Fibrin hydrogels are used as a model system for studying cell-ECM interactions. Stiffness of the fibrin ECM surrounding cells is an important input of this interaction. Stiffness values at the length scale of microns vary by as much as a few orders of magnitude in the presence of contractile cells. Exogenous patterning of matrix stiffness at this spatial scale thus could be useful in studying such interactions. We present and evaluate a technique to selectively stiffen defined regions within a fibrin hydrogel. This is accomplished via laser scanning illumination stimulating ruthenium-catalyzed crosslinking of fibrin tyrosine residuals. This results in tunable stiffness changes spanning distances as small as a few microns and a localized compaction of the material. As probed by active microrheology, stiffness changes can be as large as 25X before versus after crosslinking. Overall, this method allows for selective modification of fibrin stiffness at the micro scale with the potential to create more complex patterns, which could be valuable for the investigation of mechanotransduction in a 3D context.

4.2 INTRODUCTION

Many cell types sense and respond to the stiffness of their surrounding extracellular matrix (ECM). In 2D, this has been well demonstrated with initial substrate stiffness affecting critical cellular processes ranging from migration[1] to differentiation[2]. Interactions between cells and their surrounding ECM can be studied using 3D hydrogels as a model system for the ECM. While these hydrogel systems are far removed from native systems, they can be tuned and functionalized in ways appropriate for testing specific hypotheses. Hydrogels can be composed of natural, synthetic, or composite materials and have various properties that influence these interactions, including material stiffness[3], porosity[4], density[5], susceptibility to enzymes[6], and adhesion ligand concentrations[7]. For the case of naturally derived ECMs, it may be challenging, if not impossible, to independently modulate subsets of these features. Our group has previously demonstrated concentration independent modulation of fibrin stiffness and establishment of stiffness gradients using strain fields instead of chemical modifications[8]. We have also used optical tweezers active microrheology (AMR) to map these stiffness gradients in both cell free and cell-containing systems. In the case of cells, we have shown pericellular stiffness distributions are dependent on cell mediated matrix remodeling and strain hardening[9]. Here, we describe a new method for modulating stiffness in fibrin gels using established photochemistries and a laser scanning confocal microscope, where stiffness changes are confirmed via AMR.

Complex synthetic systems allow for control over matrix stiffness with minimal influence on other ECM properties[10,11], but are typically nonfibrous and thus missing a fundamental property of biological tissues. They tend to have mesh sizes orders of magnitude smaller than natural tissues and essentially present themselves as a continuous barrier with respect to cell confinement and biotransport. Hydrogel systems have been developed with the ability to be stiffened via light-

mediated crosslinking acting on sites incorporated into the gel at arbitrary time points after initial polymerization[12–14]. These gels have been shown to be stiffened in bulk as well as in patterned regions. Patterned stiffening has been deployed in the study of endothelial cells[15] and stem cells[16,17], both showing that cells respond differently to local stiffness found with spatially patterned constructs .

In this paper we present a technique for extending these methods into a naturally derived fibrous matrix: fibrin. Fibrin is a naturally occurring fibrous protein that is an essential component of blood clots, making up a significant portion of the provisional ECM during wound healing[18]. *In vitro* fibrin hydrogels have been used as a model of studying angiogenesis[19], stem cells[20,21], macrophages[22,23], and cancer cell lines[24]. As a hydrogel, fibrin forms a fibrous, viscoelastic, randomly interconnected matrix with pores on the length scale of one micron. At the millimeter scale fibrin's bulk material properties have been shown to be consistent from sample to sample; however, as we have shown, there is significant heterogeneity in stiffness at the subcellular spatial scale[8]. Characterizing stiffness can be further complicated by the fact that fibrin is permissive to cell mediated remodeling via enzymatic breakdown, deposition of new matrix, or other modes of ECM modification[25]. Stiffness heterogeneity increases with cell activity, or, as shown in the case of sprouting angiogenesis, bulk rheology is blinded to local stiffness changes of an order of magnitude or more[26].

One potential way to modify the stiffness of a naturally derived matrix such as fibrin is chemical crosslinking. Methods for achieving this include using cytotoxic chemicals such as glutaraldehyde[27] or harsh exposure to UV[28]. A less cytotoxic approach was demonstrated by Bjork et. al. wherein crosslinking fibrin via ruthenium-catalyzed photo-crosslinking (RCP) was shown to preserve cell viability[29]. In this method, a light activated ruthenium compound (Ru) oxidizes

tyrosine residues in the fibrin forming tyrosine radicals, which can react with other tyrosine residues to form dityrosine in the presence of persulfate[30].

Here we present and evaluate a modification to this technique, where we selectively pattern crosslinking within the volume of 3D fibrin hydrogels using a laser scanning confocal microscope and then measure induced stiffness changes via AMR. With our method, we have achieved selective stiffening within the construct at scales as small as a few microns, which may be beneficial to future studies on cell-ECM interactions within this context.

4.3 MATERIALS AND METHODS

4.3.1 HYDROGEL PREPARATION

Fibrin gels were prepared with 2.0 μm microbeads dispersed within the gels prior to gelation. Fibrinogen stock (Sigma) was dissolved in PBS and sterile filtered (0.22 μm) before use. Gelation was conducted by mixing fibrinogen/microbead/PBS solution with thrombin, to achieve a 1 mL gel with final concentrations of 2.5 mg/mL fibrin, 0.8% microbeads, and 4 U/mL thrombin. Gels were cast into 35 mm glass bottom dishes (MatTek) and kept in an incubator (37° C, 5% CO_2) for 25 minutes after which they were hydrated with 2 mL of DMEM + 10% FBS + 1% Penicillin-Streptomycin. Fibrin gels were stored in the incubator until used 24 hours after being prepared.

4.3.2 SELECTIVE AND FULL CONSTRUCT PHOTO-CROSSLINKING

Photo-crosslinking was done using a final solution containing 0.30 mg/mL tris(2,2′-bipyridyl) dichlororuthenium (II) hexahydrate (Sigma) and 0.48 mg/mL sodium persulfate (Sigma). For selective-crosslinking, a Fluoview 1200 (Olympus) system was used. With the built-in functionality of the FV system, the user can draw arbitrary ROIs to expose specific regions to controlled amounts of laser scanning. In all cases presented here, the 488 nm laser line was used

at 5% power, amounting to 1.5 mW total power. Scans were conducted at 2 µs/pixel, at 1600 px by 1600 px with no zoom applied, using a 60X 1.45NA Objective (Olympus). For full construct crosslinking, dishes were held 1 cm above an array of 4 blue LEDs (460 nm, SparkFun). LEDs run at an operating current of 20 mA per LED. Following crosslinking in both methods, gels were washed 3 times with DMEM to prevent any further activation of the crosslinker.

4.3.3 MICROSTRUCTURAL ASSESSMENT: CRM AND AMR

Confocal reflection microscopy (CRM) was performed to assess structural differences within the fibrin mesh. Imaging was done using the FV1200, using the 559 nm light which did not noticeably activate the crosslinker at the concentration used. An optical flow algorithm based on the Farneback method[31] was utilized to analyze successive frames of these images and capture deformation dynamics across the entire crosslinking process by summing deformations throughout the time series. Summed optical flow results were down sampled via bilinear interpolation by a factor of 80, resulting in nodes being spaced 10.6 microns apart.

AMR was conducted within the volume of the fibrin gels. Probed beads were located approximately 35 µm from the bottom cover glass and measurements for each sample were conducted at 50 Hz. The system used for AMR has been described in detail previously[8,9]. Briefly, probe beads within the hydrogel are oscillated via a 1064 nm laser steered by a pair of galvanometer mirrors. The movement of the bead, in response to this driving force, lenses a second, stationary laser beam (785 nm) which is then focused onto a quadrant photodiode. The complex material response (α^*) can then be calculated from the phase amplitude modulations between the steered trap and the response of the probe bead[32,33]. We present these results as $1/\alpha'$, the inverse of the real component of the complex material response (α^*). which can be thought of as a metric of stiffness.

4.3.4 STATISTICAL ANALYSIS

Statistical analysis was conducted in Origin Pro. Each set of samples was tested for normality (Shapiro-Wilk test, $p < 0.05$). Failing this, samples were tested using non-parametric statistical methods. Mann-Whitney U-tests ($\alpha=0.05$) with a Bonferroni correction was conducted for all statistical comparisons presented in this paper. Data in the manuscript is presented as mean ± standard deviation.

4.4 RESULTS

4.4.1 Selective Crosslinking Results in Structural Changes to Fibrin Mesh

A simplified schematic of RCP is shown in **Figure 4.1A**, along with a cartoon schematic of two crosslinking modalities used in this paper, either selective via a focused laser (**Figure 4.1B**) or entire fibrin gel via an LED array (**Figure 4.1C**).

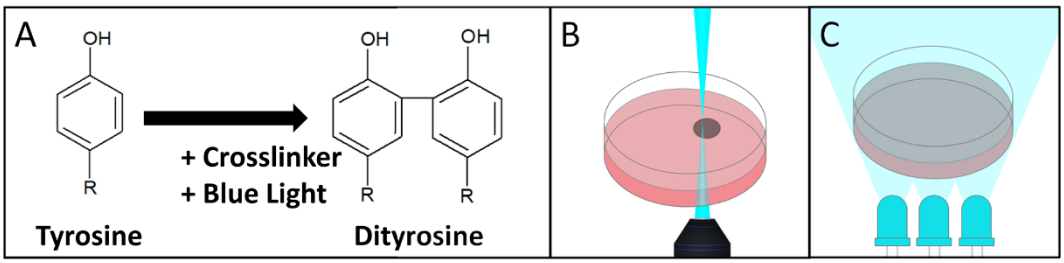

Figure 4.1*: Simplified diagram of photo-crosslinking and cartoon schematic of the two crosslinking modalities: laser scanning confocal or LED initiated. (**A**) The two active components of the crosslinking solution are the ruthenium compound (Ru) and a persulfate ion. Ru is activated by blue light and oxidizes tyrosine residues already present within fibrin into tyrosyl radicals. These radicals can react with other tyrosine residues to form dityrosine, in the presence of persulfate, which acts as an electron acceptor[30]. (**B**) In selective photo-crosslinking, the 488 nm laser line of a confocal microscope is repeatedly scanned across a region of interest. The extent of crosslinking can be controlled by laser intensity or number of sequential scans. (**C**) With LED initiated photo-crosslinking, the entire fibrin construct is illuminated using an array of 460 nm LEDs. Crosslinking extent can be controlled by intensity of the LEDs or amount of time illuminated.*

To demonstrate the selectivity of this crosslinking approach, fibrin constructs were imaged before and after treatment with a 488 nm laser, which is absorbed by Ru to initiate the crosslinking reaction. Two circular regions with diameters 10 µm and 100 µm were treated. These treatments

will be referred to as T10 and T100, respectively. Following treatment with 488 nm light to crosslink, the full field of view was imaged with a 559 nm laser, which at these crosslinker concentrations does not notably initiate the crosslinking reaction and thus is appropriate for reflection confocal microscopy. The effects of crosslinking on the fibrin matrix are shown on representative fields of view in **Figure 4.2A and B**, respectively, in both transmitted light (**i, ii, iii**) and reflection confocal modalities (**iv, v, vi**).

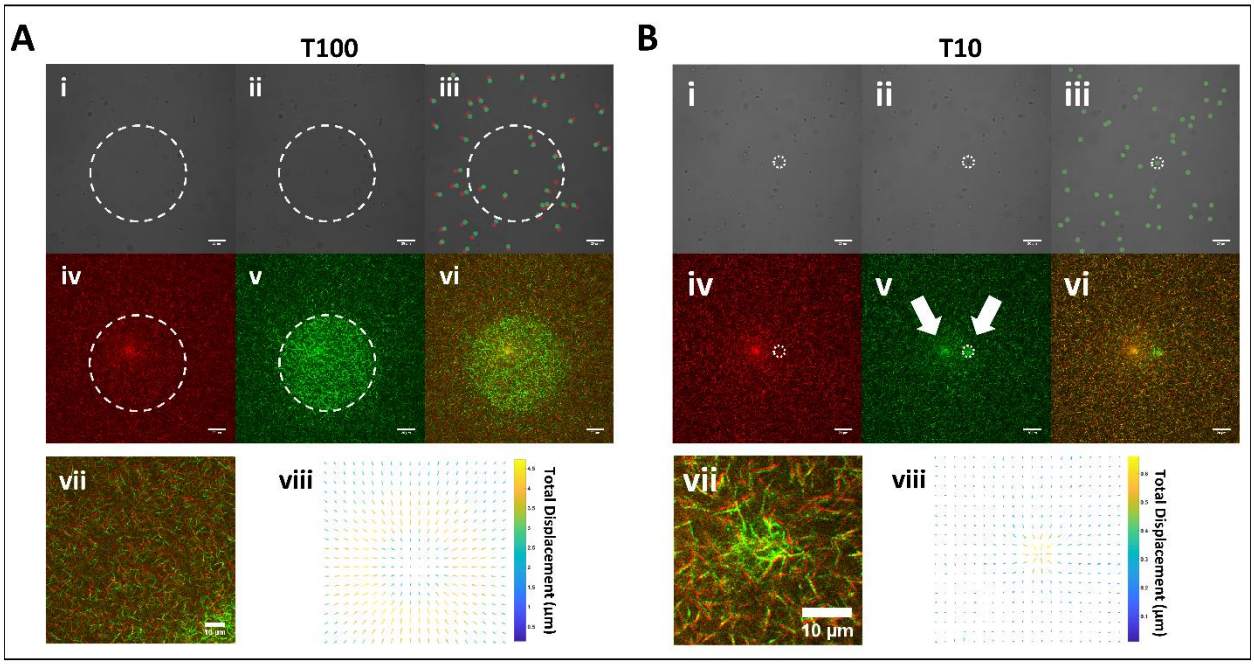

Figure 4.4: Transmitted light and reflection confocal imagery of 100 and 10 µm, (referred to as T100 and T10, respectively), diameter treatment spot sizes within fibrin gels before and after photoactivation by confocal illumination. (**A**) Transmitted light images of T100 treatment spot (**i**) before, (**ii**) after, and (**iii**) composite. Probe bead locations in the composite are marked red and green for before and after, respectively. CRM images (**iv**) before, (**v**) after, and (**vi**) composite. (**vii**) Zoomed inset of the composite image suggests contraction toward treated area, confirmed by (**viii**) optical flow analysis. (**B**) Corresponding images for T10 treatments. Note that the leftmost arrow in (v) points to an imaging artifact common to reflection confocal imaging while the rightmost points to the treated spot. Boundaries of treatment spots are marked with white dashed line. Note: Arrow length was increased for visualization, but color maps to displacement magnitude. Scale bars = 20 µm.

With T100 treatment, embedded microbeads within and beyond the region of treatment were displaced in the transverse plane by several microns (**Figure 4.2A, i-iii**). Reflection confocal imaging allows direct visualization of the fibrin mesh. Images show elevated pixel intensities in the treated region as compared to nontreated (**Figure 4.2A, iv, v**). Pseudo-colored composite

images of the mesh before and following treatment show that fibers were displaced, notably outside of the treated region (**Figure 4.2A, vi, vii**). To capture full frame videos of mesh dynamics during the crosslinking process, we implemented a confocal imaging strategy during which full field-of-view imaging at 559 nm (negligible crosslinking) was recorded in between every 100 sequential frames at 488 nm (for active crosslinking). Videos show a symmetric contraction of the mesh toward the treated area (**Supplementary Videos 1 and 2**). These were analyzed by an optical flow algorithm. Displacements were predominantly directed radially toward the center of the treated area in T100 treated samples (**Figure 4.2A, viii**). Peak displacement was located at the treatment boundary and displacement decreased radially in the positive and negative direction.

We next investigated such displacements for a T10 treated region (10-micron diameter treatment). As compared to T100 treatment, microbeads within and beyond the treatment region were displaced by no more than five hundred nanometers in the transverse plane (**Figure 4.2B i, ii, iii**). Reflection confocal imagery confirms the effect on the matrix is highly localized to the region of treatment (**Figure 4.2B iv, v, vi, vii**). Optical flow analysis shows that displacement was

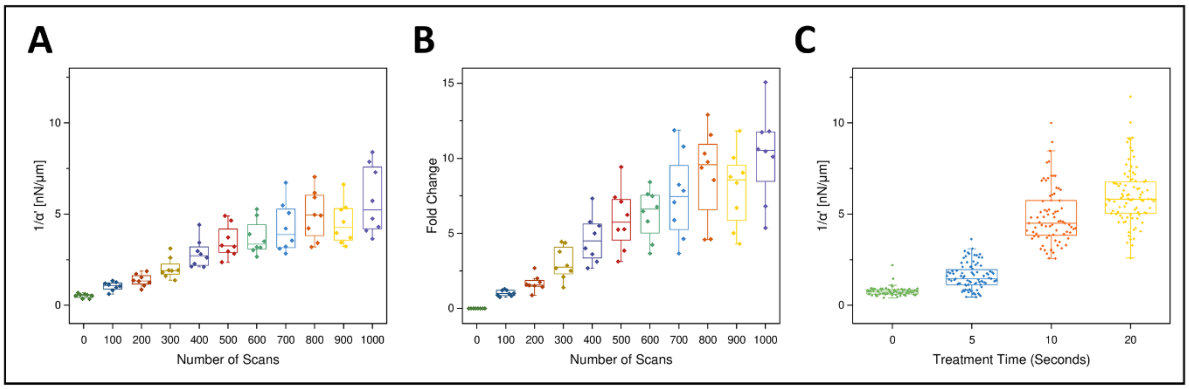

more confined, occurring only immediately proximal to the treated area with a much lower

Figure 4.7: Stiffness increases with treatment time within a fibrin gel in both selective and full construct crosslinking. (**A**) Stiffness (1/ α', nN/um) probed by AMR using the same probe particles (n_{beads}=8) after successive laser scans of a T100 treatment. Probe particles are all located within the T100 treatment region. (**B**) Data from (A) represented as fold change over the baseline (0 scans). (**C**) Change in construct stiffness after increasing LED exposure ($n_{samples}$=2, per treatment time).

displacement magnitude compared to T100 (**Figure 4.2B viii**). Outside of a few microns from the treatment area, the matrix appeared unaffected.

4.4.2 Local Stiffness Increases in Treated Area

Next, we quantified the increase in stiffness within the treated area. Embedded microbeads were probed by AMR to report local stiffness. To assess the dependence of stiffening on light exposure, AMR was conducted on 8 beads across sequential crosslinking treatments (**Figure 4.3A and B**), (100 scans with 488 nm, see Methods). The stiffness distribution after 1000 scans (**Figure 4.3A**) was comparable to that observed when the full construct crosslinked by LED illumination for 20 seconds (**Figure 4.3C,** p=0.54, Mann-Whitney Test, note the disparity between sample sizes). Also, similar to selectively crosslinked regions, LED crosslinked samples showed a denser

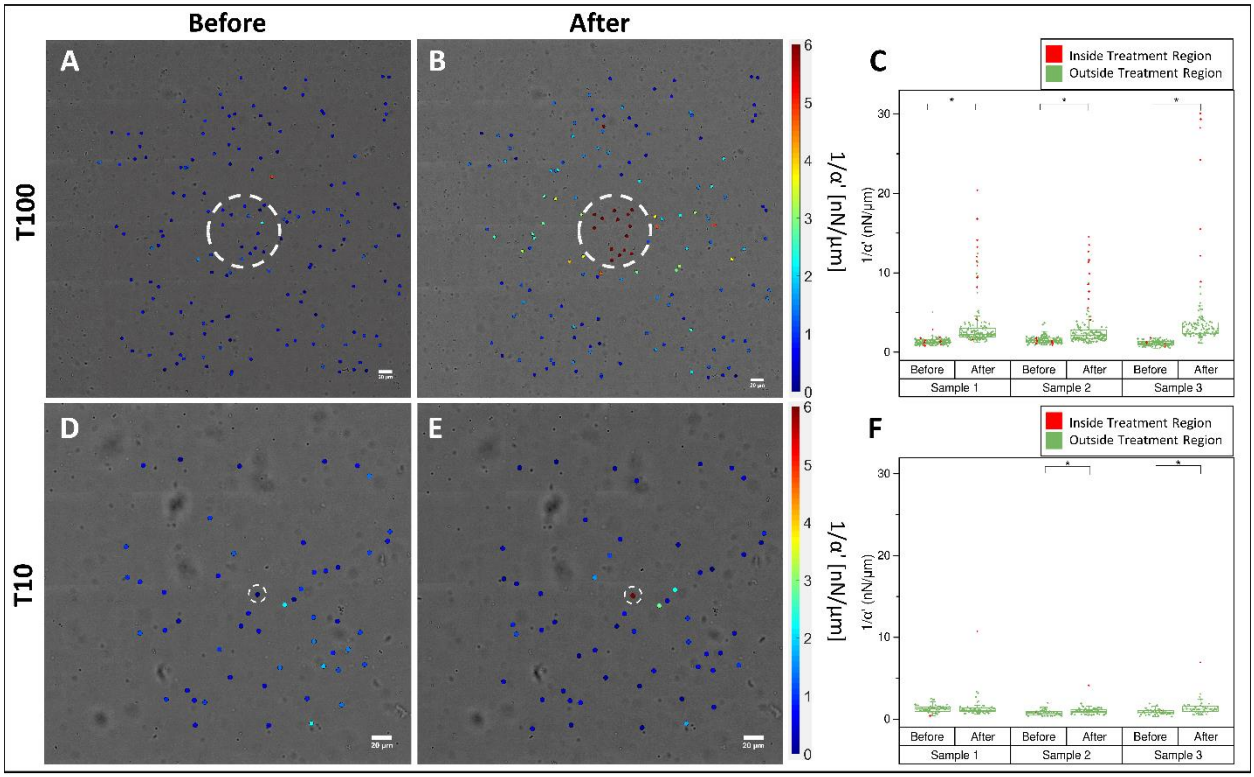

Figure 4.10: Distribution of stiffness within a fibrin gel probed by AMR before and after T100 and T10 treatments. Stiffness map (**A**) before and (**B**) after T100 treatment. (**C**) Scatter plot of all T100 treatment samples before and after treatment. Stiffness maps (**D**) before and (**E**) after T10 treatment. (**F**) Scatter plot of all T10 treatment samples before and after treatment. (*) denotes significance at 0.05 level via a Mann-Whitney Test. Note that color maps saturate at 6 nN/µm. Scale bars = 20 µm.

mesh (**Supp. Figure 4.2**). To assess if the crosslinker had any effect on gels sans illumination, we conducted a set of sham crosslinking experiments, which appeared to show minimal change to stiffness across the samples measured (**Supp. Figure 4.2**).

Beyond the treated area, we see significant stiffening for T100 treatment, but not T10 treatment (**Figure 4.4**), a result consistent with the displacement fields (**Figure 4.2A**). Representative stiffness maps are shown in **Figure 4.4.** Prior to crosslinking, stiffness is low and heterogeneous throughout the field of view (**Figure 4.4A** & **D).** Following treatment, stiffness is notably increased within the treated areas and, for the case of T100, outside the treatment area as well (**Figure 4.4B** & **E**). By contrast, stiffness changes are predominantly confined to the treatment areas in T10 treated samples. The complete set of measurements is shown in **Figure 4.4C** and **F**. On average, increases in stiffness within the treated region were 11.6 ± 7.0 nN/μm and 6.5 ± 3.6 for T100 and T10, respectively. Outside of the treated regions, stiffness changes were substantially lower: 1.3 ± 1.3 nN/μm and 0.2 ± 0.4 nN/μm, for T100 and T10, respectively. For all treatments, stiffness increases were statistically significant ($p<0.05$, Mann-Whitney test, with Bonferroni Correction), except for T10 Sample 1, which was not significant at the 0.05 level.

Changes in stiffness as a function of radial distance to the center of the treated region are plotted in **Figure 4.5**. Within both T100 and T10 treatments, stiffness change was most prominent within the boundaries of the treated region (**Figure 4.5A and B**), with fold changes as high as 25x (**Figure 4.5C and D**). In T100 treatments, stiffness change appears to extend beyond the treated region, decreasing with distance from the boundary for approximately 50 microns. For T10 treatments, stiffness change is isolated to the treated region.

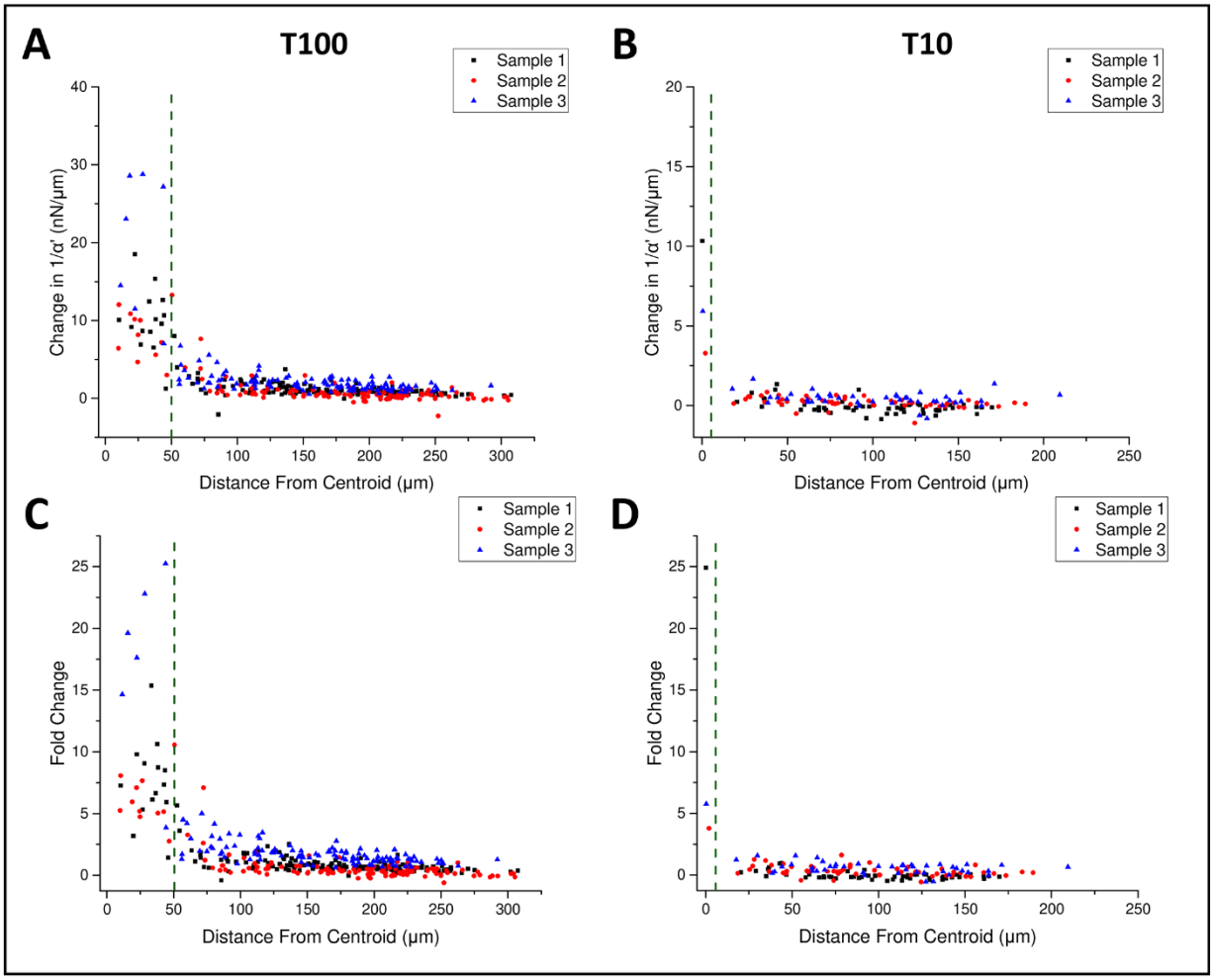

Figure 4.13: Change in stiffness as a function of distance from the center of the treatment area. Change in stiffness before versus after for (**A**) T100 and (**B**) T10 samples as a function of distance from the treatment area center. Fold change presented in (**C**) and (**D**), respectively. Dotted lines mark the outer radius of the treatment area. ($n_{samples}$=3, per treatment type).

4.5 Discussion and Conclusion

In this study we use a photo-crosslinking method coupled with a laser scanning confocal microscope to generate patterns of crosslinked areas within a fibrin hydrogel (**Supp. Figure 4.3**). Crosslinking was indicated by increased pixel brightness and any effects on stiffening were investigated via AMR. Degree of stiffening in the treated region was observed to be as much as 25-fold, which is significant in the context of published interactions between cells and their ECM. In many of these studies, the initial stiffness of an ECM has been linked to phenotypical changes such as stem cell fate in both 2D[2] and 3D[34] models. However, within a permissive environment

(such as fibrin), stiffness, architecture, and composition can be modified by cells over time[35–37]. This holds true for synthetic hydrogels, engineered to be degradable or otherwise, which are also subject to deposition of new matrix by cells[38,39]. An important consequence of cell-mediated remodeling is that measured initial stiffness of a hydrogel is insufficient to describe the mechanical environment around cells over time. In fact, we have observed that local mechanical properties both surrounding single cells and multicell angiogenic sprouts were dynamic and highly heterogeneous[9,40]. With these studies, we observed cells stiffen their pericellular matrix by as much as 35-fold versus cell-free, from an average of 0.8 ± 0.5 nN/µm initially to as high as 16.9 ± 8.0 nN/µm, with gradients as steep as 3.5 nN/um^2. Our method can induce the same range of stiffness and stiffness gradients at the sub-cellular spatial scale, allowing for exogenous control of local stiffness in a biologically meaningful way.

We also examined the effects of stiffening 'bleed through', or the extent to which ECM stiffening is observed outside of the treated region. No such bleed through was observed surrounding small T10 treated areas (**Figure 4.5B**), however, it was observed outside of T100 treated areas, particularly in the annular region between r to 2r, where r is the radius of the treated area (**Figure 4.5A**). During the crosslinking process, we noted an apparent contraction of the treated area and suspected this contraction may displace the surrounding matrix as well. This displacement could stiffen the surrounding material through strain hardening, an important characteristic of fibrin and other natural ECMs[41]. Both cell-mediated and exogenous strain have been shown to stiffen these matrices as measured by ourselves[8,9] and others[42,43]. This encouraged us to image the crosslinking process in fine steps and implement an optical flow algorithm to quantify the displacement of the matrix. While T10 treatment showed minimal displacement (**Figure 4.2B, viii**), T100 presented peak displacement within the r to 2r annulus (**Figure 4.2A,**

viii), where stiffening occurs. Taken together, these results imply that crosslinking a large area can induce strain hardening in region not affected by the photo crosslinking chemistry, a phenomenon that may be useful in the study of cellular mechanobiology.

In summary, we report a method to selectively stiffen fibrin matrices at small spatial scales. Presently, we are working on extending these results to other natural matrices such as collagen and beginning to analyze cellular response to changes in their local pericellular stiffness by our method. Lastly, we invite readers to contact the corresponding author for any additional details in implementing our method.

4.6 DISCLOSURES

The authors declare no competing financial interests

4.7 ACKNOWLEDGMENTS

We thank Linda McCarthy for her assistance in cell culture. We thank the funding sources that made this research possible National Institute of Health (NIH) T32 pre-doctoral Training Grant HL116270, and the Laser Microbeam and Medical Program, a National Biomedical Technology Resource (NIH P41-EB015890). The content is solely the responsibility of the authors and does not necessarily represent the official views of the NIH.

4.8 SUPPLEMENTARY FIGURES

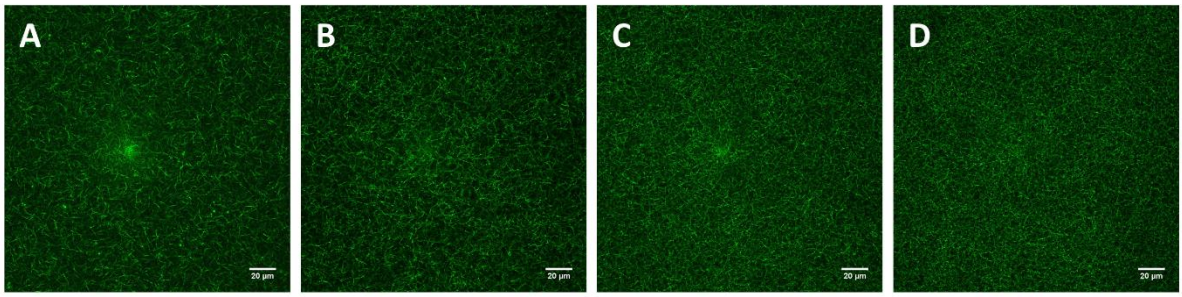

Supp. Figure 4.1*: Reflection confocal of fibrin hydrogel after treatment with LED for (**A**) 0 seconds, (**B**) 5 seconds, (**C**) 10 seconds, (**D**) 20 seconds.*

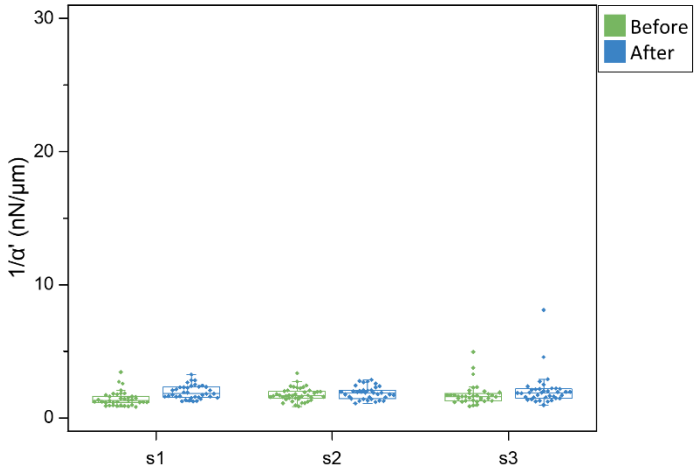

Supp. Figure 4.2*: AMR before and after sham crosslinker treatment (no light).*

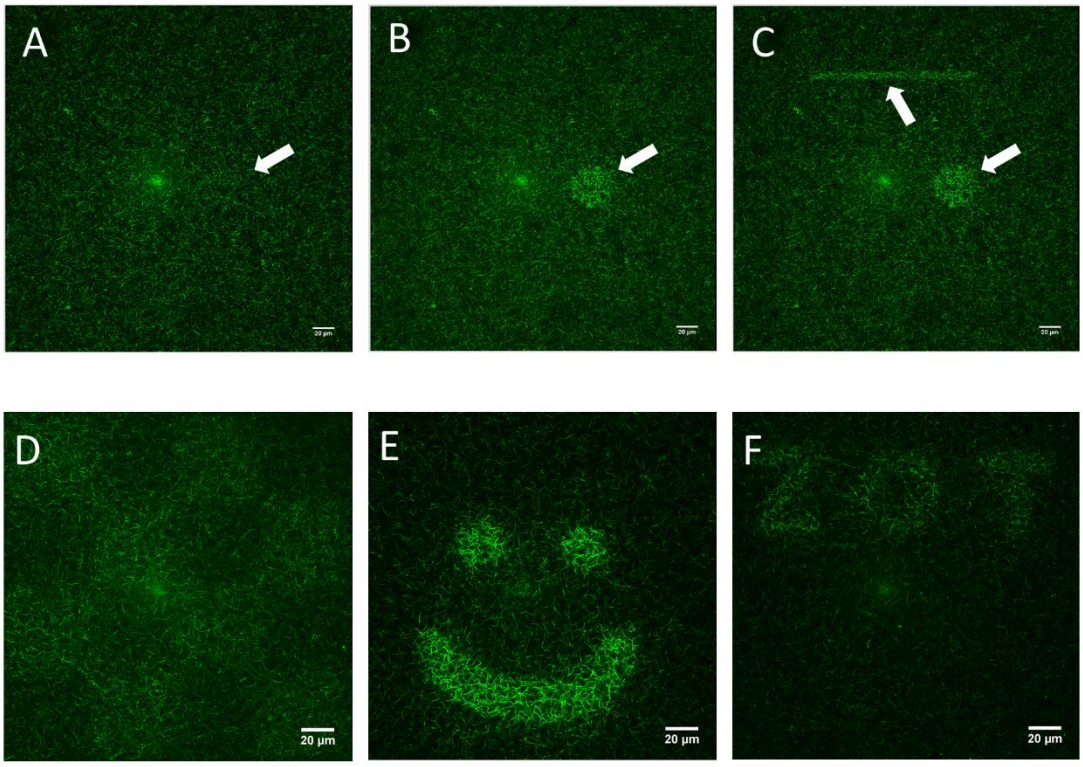

Supp. Figure 4.3*: (**A-C**) Patterning within fibrin gel using 40X (0.6 NA) air objective. Arrows denote treated spots. Spatial patterning: (**D**) checkerboard, (**E**) smiley face, (**F**) "ZOT."*

4.9 REFERENCES

1. Isenberg, B. C., DiMilla, P. A., Walker, M., Kim, S. & Wong, J. Y. Vascular smooth muscle cell durotaxis depends on substrate stiffness gradient strength. *Biophys. J.* **97,** 1313–1322 (2009).
2. Engler, A. J., Sen, S., Sweeney, H. L. & Discher, D. E. Matrix Elasticity Directs Stem Cell Lineage Specification. *Cell* **126,** 677–689 (2006).
3. Wells, R. G. The role of matrix stiffness in regulating cell behavior. *Hepatology* **47,** 1394–1400 (2008).
4. Lien, S. M., Ko, L. Y. & Huang, T. J. Effect of pore size on ECM secretion and cell growth in gelatin scaffold for articular cartilage tissue engineering. *Acta Biomater.* **5,** 670–679 (2009).
5. Kniazeva, E. & Putnam, A. J. Endothelial cell traction and ECM density influence both capillary morphogenesis and maintenance in 3-D. *AJP Cell Physiol.* **297,** C179–C187 (2009).
6. Trappmann, B. *et al.* Matrix degradability controls multicellularity of 3D cell migration. *Nat. Commun.* **8,** 1–8 (2017).
7. GOBIN, A. S. & WEST, J. L. Cell migration through defined, synthetic ECM analogs. *FASEB J.* **16,** 751–753 (2002).
8. Kotlarchyk, M. A. *et al.* Concentration independent modulation of local micromechanics in a fibrin gel. *PLoS One* **6,** (2011).
9. Keating, M., Kurup, A., Alvarez-Elizondo, M., Levine, A. J. & Botvinick, E. Spatial distributions of pericellular stiffness in natural extracellular matrices are dependent on cell-mediated proteolysis and contractility. *Acta Biomater.* **57,** 304–312 (2017).
10. Jonker, A. M., Bode, S. A., Kusters, A. H., Van Hest, J. C. M. & Löwik, D. W. P. M. Soft PEG-Hydrogels with Independently Tunable Stiffness and RGDS-Content for Cell Adhesion Studies. *Macromol. Biosci.* **15,** 1338–1347 (2015).
11. Rape, A. D., Zibinsky, M., Murthy, N. & Kumar, S. A synthetic hydrogel for the high-throughput study of cell-ECM interactions. *Nat. Commun.* **6,** 1–9 (2015).
12. Nemir, S., Hayenga, H. N. & West, J. L. PEGDA hydrogels with patterned elasticity: Novel tools for the study of cell response to substrate rigidity. *Biotechnol. Bioeng.* **105,** 636–644 (2010).
13. Kloxin, A. M., Tibbitt, M. W. & Anseth, K. S. Synthesis of photodegradable hydrogels as dynamically tunable cell culture platforms. *Nat. Protoc.* **5,** (2010).
14. Yeh, Y.-C. *et al.* Mechanically dynamic PDMS substrates to investigate changing cell environments. *Biomaterials* **145,** 23–32 (2017).
15. Lampi, M. C., Guvendiren, M., Burdick, J. A. & Reinhart-King, C. A. Photopatterned Hydrogels to Investigate the Endothelial Cell Response to Matrix Stiffness Heterogeneity. *ACS Biomater. Sci. Eng.* **3,** 3007–3016 (2017).
16. Marklein, R. A. & Burdick, J. A. Spatially controlled hydrogel mechanics to modulate stem cell interactions. *Soft Matter* **6,** 136–143 (2009).
17. Yang, C. *et al.* Spatially patterned matrix elasticity directs stem cell fate. *Proc. Natl. Acad. Sci.* **113,** E4439–E4445 (2016).
18. Clark, R. A. F. Fibrin and wound healing. *Ann. N. Y. Acad. Sci.* **936,** 355–367 (2001).
19. Nakatsu, M. N., Davis, J. & Hughes, C. C. W. Optimized fibrin gel bead assay for the study of angiogenesis. *J. Vis. Exp.* 186 (2007). doi:10.3791/186
20. Kolehmainen, K. & Willerth, S. M. Preparation of 3D fibrin scaffolds for stem cell culture applications. *J. Vis. Exp.* e3641 (2012). doi:10.3791/3641
21. Arulmoli, J. *et al.* Static stretch affects neural stem cell differentiation in an extracellular matrix-dependent manner. *Sci. Rep.* **5,** 8499 (2015).
22. Colvin, R. B. & Dvorak, H. F. Fibrinogen/fibrin on the surface of macrophages: detection, distribution, binding requirements, and possible role in macrophage adherence phenomena. *J. Exp. Med.* **142,** 1377–1390 (1975).
23. Hsieh, J. Y. *et al.* Differential regulation of macrophage inflammatory activation by fibrin and fibrinogen. *Acta Biomater.* **47,** 14–24 (2017).
24. Liu, J. *et al.* Soft fibrin gels promote selection and growth of tumorigenic cells. *Nat. Mater.* **11,** 734–41 (2012).
25. Paszek, M. J. *et al.* Tensional homeostasis and the malignant phenotype. *Cancer Cell* **8,** 241–254 (2005).
26. Juliar, B. A., Keating, M. T., Kong, Y. P., Botvinick, E. L. & Putnam, A. J. Sprouting angiogenesis induces significant mechanical heterogeneities and ECM stiffening across length scales in fibrin hydrogels.

Biomaterials **162,** 99–108 (2018).
27. Charulatha, V. & Rajaram, A. Influence of different crosslinking treatments on the physical properties of collagen membranes. *Biomaterials* **24,** 759–67 (2003).
28. Cornwell, K. G. & Pins, G. D. Discrete crosslinked fibrin microthread scaffolds for tissue regeneration. *J. Biomed. Mater. Res. Part A* **82A,** 104–112 (2007).
29. Bjork, J. W., Johnson, S. L. & Tranquillo, R. T. Ruthenium-catalyzed photo cross-linking of fibrin-based engineered tissue. *Biomaterials* **32,** 2479–2488 (2011).
30. Fancy, D. A. & Kodadek, T. Chemistry for the analysis of protein–protein interactions: Rapid and efficient cross-linking triggered by long wavelength light. *Chem. Biochem.* **96,** 6020–6024 (1999).
31. Farnebäck, G. Two-frame motion estimation based on polynomial expansion. *Image Anal.* **2003,** 363–370 (2003).
32. Brau, R. R. *et al.* Passive and active microrheology with optical tweezers. *J. Opt. A Pure Appl. Opt.* **9,** S103–S112 (2007).
33. Mizuno, D., Tardin, C., Schmidt, C. F. & Mackintosh, F. C. Nonequilibrium mechanics of active cytoskeletal networks. *Science* **315,** 370–3 (2007).
34. Huebsch, N. *et al.* Harnessing traction-mediated manipulation of the cell/matrix interface to control stem-cell fate. *Nat. Mater.* **9,** 518–26 (2010).
35. Birkedal-Hansen, H. Proteolytic remodeling of extracellular matrix. *Curr. Opin. Cell Biol.* **7,** 728–735 (1995).
36. Matrisian, L. M. Metalloproteinases and their inhibitors in matrix remodeling. *Trends Genet.* **6,** 121–125 (1990).
37. Larsen, M., Artym, V. V., Green, J. A. & Yamada, K. M. The matrix reorganized: extracellular matrix remodeling and integrin signaling. *Curr. Opin. Cell Biol.* **18,** 463–471 (2006).
38. Caliari, S. R., Vega, S. L., Kwon, M., Soulas, E. M. & Burdick, J. A. Dimensionality and spreading influence MSC YAP/TAZ signaling in hydrogel environments. *Biomaterials* **103,** 314–323 (2016).
39. Nicodemus, G. D., Skaalure, S. C. & Bryant, S. J. Gel structure has an impact on pericellular and extracellular matrix deposition, which subsequently alters metabolic activities in chondrocyte-laden PEG hydrogels. *Acta Biomater.* **7,** 492–504 (2011).
40. Juliar, B. A., Keating, M. T., Kong, Y. P., Botvinick, E. L. & Putnam, A. J. Sprouting angiogenesis induces significant mechanical heterogeneities and ECM stiffening across length scales in fibrin hydrogels. *Biomaterials* **162,** (2018).
41. Shah, J. V. & Janmey, P. A. Strain hardening of fibrin gels and plasma clots. *Rheol. Acta* **36,** 262–268 (1997).
42. Jansen, K. A., Bacabac, R. G., Piechocka, I. K. & Koenderink, G. H. Cells actively stiffen fibrin networks by generating contractile stress. *Biophys. J.* **105,** 2240–2251 (2013).
43. Winer, J. P., Oake, S. & Janmey, P. A. Non-linear elasticity of extracellular matrices enables contractile cells to communicate local position and orientation. *PLoS One* **4,** (2009).

CHAPTER 5: CONCLUSIONS

5.1 SUMMARY AND IMPLICATIONS

It is understood that interactions between cells and the extracellular matrix (ECM) are reciprocal and governed by both outside-in and inside-out processes. Several notable experiments show that an increase in bulk ECM stiffness correlates with mammary epithelial cell invasion into the ECM[1], differentiation of mesenchymal stem cells down specific lineages[2,3], and maturation of cardiomyocytes[4]. Cells are also known to actively alter their ECM through context-dependent degradation, remodeling, and deposition of new molecules[5]. These changes, in turn, can affect neighboring cells. Tissue homeostasis, morphogenesis and pathology are all dependent, to varying degrees, on such mechanical interactions.

In conclusion, my thesis presents insight into cell-ECM mechanical interactions by probing measuring the mechanical topography of two *in vitro* systems and introduces a method that will aid in the study of these interactions via selective crosslinking. With this work, I have continued our lab's work to explore distributions of stiffness within the pericellular space and have now introduced an appropriate tool to modify it. In **Chapter 2**, I demonstrated our ability to probe the pericellular space, uncovering a dependence of the normal pericellular mechanical topography on proteolysis and contractility. This work underscores an important question in the realm of mechanobiology – specifically, which stiffness are cells responding to? Much of cell-ECM interaction has been studied using bulk stiffness values, however we have found similar stiffness ranging orders of magnitude around a single cell. With **Chapter 3**, I extended the techniques from Chapter 2 to probe around multi-cellular angiogenic sprouts and compare those results directly to those seen with bulk rheological methods. This built upon the previous

findings, showing that during a large morphogenic process, bulk rheological measurements were blinded to the mechanics involved. Lastly, with **Chapter 4**, I presented and evaluated a method to modify the stiffness of fibrin matrices at spatial scales relevant to the pericellular stiffness distributions we have been observing. I am hopeful that this provides a tool for future studies of stiffness distributions on cell behavior, as now we should be able to modify and create similar stiffness distributions.

5.2 REFERENCES

1. Paszek, M. J. *et al.* Tensional homeostasis and the malignant phenotype. *Cancer Cell* **8,** 241–254 (2005).
2. Park, J. S. *et al.* The effect of matrix stiffness on the differentiation of mesenchymal stem cells in response to TGF-β. *Biomaterials* **32,** 3921–3930 (2011).
3. Chaudhuri, O. & Mooney, D. J. Stem-cell differentiation: Anchoring cell-fate cues. *Nat. Mater.* **11,** 568–569 (2012).
4. Young, J. L., Kretchmer, K., Ondeck, M. G., Zambon, A. C. & Engler, A. J. Mechanosensitive kinases regulate stiffness-induced cardiomyocyte maturation. *Sci. Rep.* **4,** 6425 (2014).
5. Kumar, S. & Weaver, V. M. Mechanics, malignancy, and metastasis: The force journey of a tumor cell. *Cancer Metastasis Rev.* **28,** 113–127 (2009).